Cerebral Cortex, June 2020;30: 3483–3517

doi: 10.1093/cercor/bhz322
Advance Access Publication Date: 2 January 2020
Feature Article

FEATURE ARTICLE

Anatomy and Physiology of Macaque Visual Cortical Areas V1, V2, and V5/MT: Bases for Biologically Realistic Models

Simo Vanni[1,2], Henri Hokkanen[1,2], Francesca Werner[1,2,3], and Alessandra Angelucci[4]

[1]HUS Neurocenter, Department of Neurology, Helsinki University Hospital, 00290 Helsinki, Finland, [2]Department of Neurosciences, University of Helsinki, 00100 Helsinki, Finland, [3]Department of Biomedical and Neuromotor Sciences, University of Bologna, 40126 Bologna, Italy, and [4]Department of Ophthalmology and Visual Sciences, Moran Eye Institute, University of Utah, Salt Lake City, UT 84132, USA

Address correspondence to Simo Vanni, Biomedicum Helsinki, Neurology Research Unit, P.O. Box 700, 00290 Helsinki, Finland. Email: simo.vanni@helsinki.fi.

Abstract

The cerebral cortex of primates encompasses multiple anatomically and physiologically distinct areas processing visual information. Areas V1, V2, and V5/MT are conserved across mammals and are central for visual behavior. To facilitate the generation of biologically accurate computational models of primate early visual processing, here we provide an overview of over 350 published studies of these three areas in the genus *Macaca*, whose visual system provides the closest model for human vision. The literature reports 14 anatomical connection types from the lateral geniculate nucleus of the thalamus to V1 having distinct layers of origin or termination, and 194 connection types between V1, V2, and V5, forming multiple parallel and interacting visual processing streams. Moreover, within V1, there are reports of 286 and 120 types of intrinsic excitatory and inhibitory connections, respectively. Physiologically, tuning of neuronal responses to 11 types of visual stimulus parameters has been consistently reported. Overall, the optimal spatial frequency (SF) of constituent neurons decreases with cortical hierarchy. Moreover, V5 neurons are distinct from neurons in other areas for their higher direction selectivity, higher contrast sensitivity, higher temporal frequency tuning, and wider SF bandwidth. We also discuss currently unavailable data that could be useful for biologically accurate models.

Key words: biomimetic, computational neuroscience, microcircuit, neural network, neuroinformatics

Introduction

One of the fundamental aims of visual neuroscience is to understand the computational principles underlying biological vision. How do the biophysics of single neurons and network interactions generate neuronal receptive fields (RFs), process sensory inputs, and cause visual behavior? Decades of studies have provided a wealth of data and multiple descriptive and quantitative models of vision. Nevertheless, we still lack the ability to construct accurate computational models that can reproduce a biologically meaningful visual system. Such models and related computer simulations could help bridge the gap between the physiological responses of single neurons and existing abstract models of vision as well as provide a better understanding of cortical processing.

The continuous increase of computational power has recently enabled the first comprehensive microcircuit simulations of the rat somatosensory cortex (Markram et al. 2015).

Recent simulations of macaque monkey visual cortex have explored large-scale interactions between visual cortical areas (Mejias et al. 2016), replicated natural firing rate statistics in a laminar network model of the primary visual cortex (V1; Rasch et al. 2011), or described the generation of orientation tuning and the dynamics of V1 sublayer 4C alpha (Chariker et al. 2016). However, we are still far from being able to replicate the multiplicity of cortical functions, let alone visual behavior, with biologically realistic model simulations.

Accurate numerical model simulations require quantitative data on the anatomy and physiology of the system, as well as on the structure and biophysical parameters of distinct cell types. With unavoidable gaps in available data, unknown parameters need to be explored against known neural RF properties and eventually compared with visual behavior.

To facilitate the generation of realistic computational models of visual cortex, here we have collated data from more than 350 publications on connectivity, physiological RF properties, and single neuron biophysical properties in three visual cortical areas (V1, V2, and V5 or middle temporal [MT]) of the macaque monkey, one of the best studied animal genus in vision research and the available animal model closest to humans (Kaas 1992; Preuss 2004).

In macaques, visual information drives a network of about 30 interconnected cortical areas organized into a hierarchical network according to laminar connectivity patterns (Maunsell and Van Essen 1983b; Ungerleider and Desimone 1986b; Zeki and Shipp 1988; Felleman and Van Essen 1991; Merigan and Maunsell 1993; Barone et al. 2000; Van Essen 2003; Shipp 2007; Kravitz et al. 2011, 2013; Markov et al. 2014b). V1, at the bottom of this hierarchy, sends prominent connections to areas V2, V3, V4, V5/MT, and V6; in turn these V1-recipient cortical areas are interconnected with each other.

Here we focus on areas V1, V2, and V5/MT, as there is general agreement on the location and macroscopic boundaries of these areas in primates and humans, and their anatomy and electrophysiological properties have been extensively characterized. In contrast, there is ongoing debate regarding the exact parcellation and function of the areas that occupy the cortical territory between V2 and V5 (Kaas 1992, 2003; Van Essen 2003; Wandell et al. 2007; Angelucci and Rosa 2015; Angelucci et al. 2015; Zhu and Vanduffel 2019). V1, V2, and V5 participate in early visual processing and are mutually connected. These areas represent multiple low- and middle-tier visual stimulus features at various scales, necessary for visually guided behavior (Hegdé and Van Essen 2003; Born and Bradley 2005; Sincich and Horton 2005; Vidyasagar and Eysel 2015; Zeki 2015). Phylogenetically, V1 and V2 are conserved in mammals, and V5 is found in all primate species studied (Kaas 1995, 2003; Large et al. 2016) suggesting that these three areas play a fundamental role in cortical processing of visual signals.

Despite challenges, such as the occurrence of multidimensional RFs, the complexity of the cortical microcircuit, different definitions of the various parameters in different studies, and missing data, this review attempts to report the available data in a consistent way. We also attempt to provide a balanced overview of controversial issues and to emphasize quantitative data. The latter are reported as numerical quantities, or best estimates of proportions or relative strengths, when these are available in the literature. When quantitative data are not available, we cover qualitatively topics, which we consider important for building computational models.

Anatomical and Physiological Database and Conventions

All data reported here are limited to the Old World monkey genus Macaca, including mainly the species *M. fascicularis*, *M. nemestrina*, *M. mulatta*, and *M. fuscata*. In addition, we report data from functional anatomy studies performed in *M. arctoides*, *M. assamensis*, *M. irus*, or *M. radiata*. When different developmental stages were compared in a study, we extracted only data from young adult individuals.

For consistency and brevity, we have excluded data from New World monkeys, which are phylogenetically more distant from humans than macaques [for phylogenetic comparison of primate visual cortices, see (Kaas 2003, 2005; Rosa and Tweedale 2005)]. However, for some experimental questions and methodological approaches, the New World primates are better suited animal models. For example, the smooth cortical structure of the marmoset cortex allows easier and simultaneous access to multiple visual cortical areas.

We have combined data from several species of the genus *Macaca*. Brain volume across the included species varies by a factor of about 1.7 (Marino 1998), which may introduce variability in quantifications between different datasets. Given the similar pattern of V1 layers across primate species (Balaram and Kaas 2014), we expect little structural variation across macaque subspecies. Saleem et al. (2007) studied the anatomical differences of medial temporal lobe areas between *M. fuscata*, *M. fascicularis*, and *M. mulatta*. They found a similar anatomical organization of cortical layers, but one of the four areas studied showed a shift in areal boundary across subspecies. Similarly, the primary auditory cortex and its surrounding fields are smaller in *M. fascicularis* than in *M. fuscata*, whereas the laminar distributions of various histochemical stains were similar (Jones et al. 1995). These studies suggest that subtle differences in the macroscopic anatomy of visual cortical areas are likely to exist among macaque subspecies, but the general functional architecture is likely conserved.

Moreover, animal gender can introduce additional variability, as for example, in *M. mulatta*, the volume of the male brain is on average 1.26 times larger than that of the female (Franklin et al. 2000). However, the primary driver of variability is likely the body weight, as this is closely correlated with brain weight (Jerison 1955), therefore requiring knowledge of the body weight of the individual animals, more than their species or gender, in order to calibrate the data; unfortunately, we lacked this information and therefore our reports are not corrected for any of these factors.

Tuning properties of neuronal responses to 11 visual stimulus parameters were reported consistently across the literature and are summarized in the figures. For other parameter values in the text and tables, we report the mean and range of the mean values reported across studies (but no range if there was only one study). For a model system, this can serve as the range of possible mean parameter values. The distribution of values behind the means was inconsistently reported across studies, and, of course, it was impossible for us to control for outliers. These original distributions are omitted in this review, unless descriptive statistics, such as standard deviation, were available for the whole data in the original studies. The supplementary material comprises both anatomical and physiological data in machine-readable csv format.

Anatomical Conventions

There are two different nomenclatures for V1 layers in the literature. We follow the more widely used Brodmann's nomenclature, according to which layer (L) 4 has four subdivisions (4A, 4B, 4Cα, 4Cβ; Brodmann 1909, translated by Garey (Brodmann and Garey 2006)). Hassler's nomenclature is based on the same histological subdivisions, but layers 4A and 4B of Brodmann are considered part of L3 (Hassler 1966).

Area V5 is also known as MT, for middle temporal, following its original naming in the New World monkeys. In V1, we group L2 with L3A, as typical in many interlaminar connectivity studies.

Here connection strength is defined mainly as the number of labeled neurons in retrograde tracer studies or density of axonal projections of singly labeled neurons. Such anatomical definition of strength does not obviously reflect the actual physiological strength of a connection, which depends on several other factors such as neuron identity, and the number, strength, and locations of presynaptic boutons on the postsynaptic neuron. Note, also, that connection strength can only be compared within single tracer injections, because the number of labeled cells varies across injections of different size. When quantitative data were unavailable, connection strength was estimated from figures or from the text and reported in Figure 2 and Supplementary Table 1 as sparse, medium, or dominant connection strength to indicate the approximate number of presynaptic somata or axonal terminations. For interareal connections, the term "dominant" indicates the combined dominant origin and termination of a given connection. In the absence of any description of connection strength in the original publications, we set the strength to medium. For contradicting results in different studies, we gave more weight to the data that were more rigorously quantified. When quantitative data were available, sparse, medium, and dominant connections (in Fig. 2 and Supplementary Table 1) indicate $<10\%$, 10–50%, and $>50\%$, respectively, of cells (for a given tracer injection) or of synapses/boutons/axonal length (for intracellular microinjections).

When axons of traced neurons were reported to terminate at a border between two cortical layers, the connection was marked as terminating in both layers. We included studies using glutamate uncaging (Sawatari and Callaway 2000; Briggs and Callaway 2001, 2005; Yabuta et al. 2001). This method reveals connections to neurons with somata and dendrites located within the postsynaptic layer, as well as to neurons with somata residing in other layers but with dendrites extending into the postsynaptic layer. Connectivity studies based on degeneration were not included.

For interareal connectivity studies, single tracer injections are typically not confined to a layer, and therefore the layers of origin and termination within the injection site could not be identified. Therefore, in Supplementary Table 1, we report separately the literature references for the connections' origin and termination; moreover, for each laminar origin and termination, the same reference is repeated for each laminar termination and origin, respectively. These data are visualized in Figure 2 reporting the existence and density of interareal connections between different layers of the connected areas. For example, Lund et al. (1981), following retrograde tracer injections across all V2 layers, found labeled cells in V1 L2/3A, 4A, and 4B, while following anterograde tracer injections into all V1 layers, they found labeled terminations in V2 L4 and L3B with sparser spread into L3A and at the L5 and 6 border. For the retrograde tracer injection of this study, in Supplementary Table 1 and Figure 2, we report three types of connections from V1 to V2, one arising from V1 L2/3A, the second from V1 L4A, and the third from V1 L4B, each terminating in V2 L3A, 3B, 4, 5B, and 6, and cite this study five times for each of the three V1 layers of origin.

Description of Physiological Parameters

Physiological RF data were reported as the total number or percent of cells in a given area as a function of a given RF parameter. This allowed us to combine different datasets if the reported values were comparable. To this goal, we extracted and digitized data from the figures in the original publications and reported in our figures the proportion of cells across studies as a function of a given physiological parameter value. Because we are not analyzing the original raw data, but summary histograms, the descriptive statistics we report here inevitably include some inaccuracies, for example, errors in the centering of the bins on the x-axis of the original data, residual rotation, and calibration and digitization errors. As a quality control, we visualized all data reporting figures, calibration and digitized points, and then redigitized all data exceeding 10% mismatch between the total number of cells reported in the original study and that reported in our data.

Different studies used different metrics for data analysis. We included only data from one of these metrics or data that could be converted into a standard metrics using a simple transformation. For example, different datasets report either circular variance (CV) or orientation selectivity index (OSI $= 1-$CV), as measures of orientation selectivity. In this case, we converted OSIs to CV.

Anatomy

Anatomical data show significant individual variability, and many studies are based on only few monkeys. Thus, some of the mean values reported below may not reflect real population means.

Recently, mouse neocortical cells have been classified into 133 transcriptomic clusters based on single-cell RNA sequencing. These clusters included 61 GABAergic, 56 glutamatergic, and 16 nonneuronal types (Tasic et al. 2018). However, the number of such clusters depends on the cut point of the clustering method. Based on axonal projection patterns mainly in rodents, cortical excitatory cells have been classified into three major groups, intratelencephalic (projection to cortex and striatum), pyramidal tract (projections mainly to the brainstem, spinal cord, and midbrain), and corticothalamic (projections mainly to the ipsilateral thalamus), with ongoing subgrouping efforts based on morphology, gene expression, and physiology (reviewed in Shepherd 2013; Harris and Shepherd 2015). Following existing literature on the neuroanatomy of macaque visual cortex, largely from the 1980s until the last decade (Gilbert 1983; Nieuwenhuys 1994; Douglas and Martin 2004), below we divide excitatory cells into two major morphological groups, spiny stellate and pyramidal cells (PCs). Further subgrouping PC is challenging, due to the wide diversity of PC dendritic and axonal morphologies, which could result in an intricate classification according to soma position, branching patterns, or axonal targets (examples in Larkman 1991; Markram et al. 2015); moreover, such a subgrouping across layers has not been systematically applied to

macaque visual cortex. The pyramidal and spiny stellate cells receive excitatory input predominantly onto their spines and inhibitory input onto their somas, dendritic shafts, and axon initial segments.

Likewise, a general system for GABAergic interneuron classification is missing [for reviews, cf., (Markram et al. 2004; Ascoli et al. 2008; DeFelipe et al. 2013)]. Cells immunoreactive for the calcium-binding proteins calbindin, calretinin, and parvalbumin are distributed nonuniformly across laminae in macaque V1 and V2 (DeFelipe et al. 1999), but these markers are not uniquely mapped to morphological cell types (Ascoli et al. 2008; Markram et al. 2015). In rodent cortex, interneurons have been classified into three major types based on expression of parvalbumin, somatostatin, and $5HT_{3A}$-receptor, each type having a different embryonal origin (Lee et al. 2010; Rudy et al. 2011). However, a similar classification has not been systematically applied to macaque visual cortex.

Gamma-aminobutyric acid (GABA)-releasing inhibitory interneurons can be further classified based on the morphological, physiological, or molecular phenotype (Ascoli et al. 2008; DeFelipe et al. 2013). At least eight morphological subtypes exist (Jones 1993; DeFelipe et al. 2013), with the double bouquet cell following a unique developmental path in primates (reviewed in DeFelipe 2011; Betizeau et al. 2013). In the 1980s and 1990s, Jennifer Lund and colleagues published a series of Golgi staining studies describing the various morphological inhibitory cell types in macaque V1 and their distinct laminar distributions of dendritic and axonal projections (Lund 1987; Lund et al. 1988; Lund and Yoshioka 1991; Lund and Wu 1997). These studies, however, did not quantify these cells' morphological features. Recently introduced automatic classifier methods might help generating a more unified classification of cell type morphologies (DeFelipe et al. 2013), but presently there exist no quantitative analyses of inhibitory cells in distinct areas and layers of macaque visual cortex.

Area Size and Cell Numbers, Types, and Locations

Lateral Geniculate Nucleus

In each lateral geniculate nucleus (LGN) of *M. mulatta*, the two magnocellular (Magno) layers, one for each eye, comprise on average 148×10^3 neurons (range across monkeys $91–235 \times 10^3$), and the four parvocellular (Parvo) layers, two for each eye, 1270×10^3 neurons (range $900–1700 \times 10^3$, Ahmad and Spear 1993). Earlier estimates of Magno and Parvo LGN cell numbers, including data from undefined macaque species, give values between the ranges above (le Gros Clark 1941; Connolly and Van Essen 1984; reviewed in Peters et al. 1994). Of the numbers above, 35% of cells in the Magno layers and 25% of cells in the Parvo layers are immunoreactive for the inhibitory neurotransmitter GABA, therefore are local inhibitory interneurons, the remaining being thalamocortical projection neurons (Montero and Zempel 1986).

A neurochemically distinct population of koniocellular (Konio) cells was recognized later (Hendry and Yoshioka 1994). It occupies primarily the spaces between and below the Magno and Parvo layers in LGN, forming six distinct layers, termed the intercalated or K layers (reviewed in Hendry and Reid 2000; Casagrande et al. 2007). These layers comprise about 100×10^3 projection neurons and apparently no inhibitory interneurons. In addition, small neurons with the chemical signature of K cells are also scattered within the M and P layers and form bridges between the K layers (Hendry and Yoshioka 1994).

Table 1 Cortical surface areas (mm^2) from anatomical studies

	V1	V2	V5
Mean	1181 (797–1343)	944 (730–1012)	50 (33–73)
Min	690	660	24
Max	1817	1412	99
N	58	17	37
Refs	1–5,9	1,3,8–9	2,6–7,9

N = total number of hemispheres. The mean values across studies were weighted by the N hemispheres in each study. Parenthesis encloses the range across the means of individual studies. Min and max values indicate the lowest and highest values in individual monkeys across all studies. References: 1, Gattass et al. (1981); 2, Van Essen et al. (1981); 3, Van Essen et al. (1986); 4, Van Essen et al. (2002); 5, O'Kusky and Colonnier (1982a); 6, Ungerleider and Desimone (1986a); 7, Maunsell and Van Essen (1987); 8, Olavarria and Van Essen (1997); and 9, Sincich et al. (2003).

V1, V2, and V5: Area Size

The sizes and neuron numbers of cortical areas vary across individual monkeys, being related to body weight, which has an allometric relation to cortical surface (Maunsell and Van Essen 1987; Hofman 1989).

In the adult macaque monkey, the whole cortical surface of one hemisphere may comprise up to 130–140 functionally distinct areas (Van Essen et al. 2012) and covers, on average, an area of 10 430 mm^2 ($N = 10$ hemispheres from 3 *M. mulatta* and 7 *M. fascicularis*, range across monkeys 8286–14 113 mm^2; Sincich et al. 2003). V1 represents about 13% and V2 about 10% of this total area. Table 1 reports the surface areas for V1, V2, and V5. The corresponding surface area ratios between these three areas are 1:0.80:0.042, respectively.

V1: Neuron Numbers and Types

PC bodies occur in all V1 layers, except 4C and 1 (Lund 1973). Moreover, the apical dendrites of PCs residing in L5 and L6 have few spines in L4C. Spiny stellate cells occur in all V1 L4 subdivisions, and in L4C they constitute 85–95% of all neurons (Mates and Lund 1983; Fitzpatrick et al. 1987). Moreover, Briggs et al. (2016) have recently reported some spiny stellate cells in V1 L6A. Inhibitory stellate cells occur in all V1 layers.

Figure 1 depicts the modular organization of V1, which includes the ocular dominance columns (ODCs) and cytochrome oxidase (CO) blobs, as well as the six layers of V1. Monocular RFs predominate in L4C, and the blob structure is most evident in L3. Above and below these layers, RFs are biased to represent the same ODC, blob/interblob compartment, and other RF properties such as preference for the orientation of edges, usually referred to as columnar organization.

Table 2 reports the total number of neurons and the relative number of inhibitory neurons in each layer of area V1. The total number of neurons in one hemisphere of adult macaque V1 ($N = 2$ *M. fascicularis* and 4 *M. mulatta*) is 161×10^6 (standard deviation [SD] = 18), and the total number of synapses is 381×10^9 (SD = 53). In this dataset, V1 covers on average 841 mm^2 (SD = 88) surface area ($N = 7$ hemispheres; O'Kusky and Colonnier 1982b). A recent study based on rigorous stereological methods estimated V1 neuron numbers more than double the original estimates (Table 2; Giannaris and Rosene 2012).

In V1, 19% (range 18.5–19.6%) of neurons are GABA immunoreactive, while in extrastriate cortex surrounding V1, including area V2, the proportion of inhibitory neurons is 25% (range 24.2–25.3%, $N = 5$ hemispheres, Hendry et al. 1987). No apparent

Table 2 Total number of neurons, synapses/neuron, and the proportion of inhibitory interneurons in each cortical layer of area V1

Layer	N neurons × 10^6	Synapses/neuron × 10^3	% inhibitory	N neurons × 10^6
1	0.47	61.8	84	Supragr. 215
2	44*	2.6*	20	
3			20	
4A	17	1.6	22	Granular 121
4B	17	2.7	19	
4Cα	14	1.9	16**	
4Cβ	24	1.4		
5	20	1.7	20	Infragr. 80
6	24	2.1	15	
Total	161	2.3		416
Refs	1	1	2–4	5

*Layers 2 and 3 together; **Layers 4Cα and 4Cβ together. References: 1, O'Kusky and Colonnier (1982b); 2, Fitzpatrick et al. (1987); 3, Hendry et al. (1987); 4, Beaulieu et al. (1992); and 5, Giannaris and Rosene (2012).

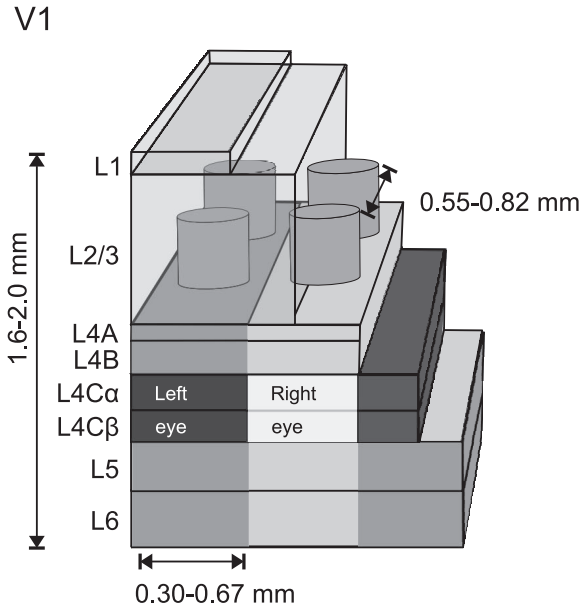

Figure 1. Schematics of CO and ocular dominance modules in V1. The cylinders in L3 depict CO blobs and the lighter and darker columnar gray bands the ODCs, most emphasized in L4C (Hubel and Wiesel 1968). References for cortical thickness (range of means; Chow et al. 1950; Lund 1973; O'Kusky and Colonnier 1982b); layer thickness is drawn approximately to scale (Lund 1973); reported distance between CO blobs is the range across monkeys (Horton 1984; Landisman and Ts'o 2002); reported width of ODC is the range across monkeys (LeVay et al. 1975; Horton and Hocking 1996).

difference in the density of GABAergic cells exists between the CO blobs and interblobs of V1 (Beaulieu et al. 1992).

In primate evolution, L4 of area V1 has become specialized into three sublayers (reviewed in Casagrande and Kaas 1994), and correspondingly the number of neurons in V1 per unit surface area doubled compared with other cortical areas (Hendry et al. 1987). In addition, of all cortical areas, the density of neurons per unit volume is highest in V1. The mean density of neurons across all layers in V1 is $230 \times 10^3/mm^3$ (range 190–$280 \times 10^3/mm^3$; average of three *M. fascicularis* monkeys) and drops in V2 to $130 \times 10^3/mm^3$ (range 110–$140 \times 10^3/mm^3$; average of two *M. fascicularis*, and one *M. mulatta*, Kelly and Hawken 2017). The neuronal densities per unit mass show similar trends, being highest in V1 (130–177×10^6/g) and somewhat lower in V2 (89–114×10^6/g) and V5 (85×10^6/g; *M. mulatta*, Collins 2011).

Layer 4A has a unique honeycomb-like appearance consisting of parvocellular geniculate afferent axons, local groups of pyramidal neurons in cone-like arrangement (30–80 µm wide, mean 60 µm), separated by neuropil, and vertical apical dendritic clusters (1270 clusters/mm^2) arising from L5 PCs (Peters and Sethares 1991a, 1991b).

V2: Neuron Numbers and Types

Only sparse quantitative data exist for V2. Rockland (1997) estimated that beneath $1mm^2$ area of V2 lay about 92 600 neurons (of which 31 200 in L3, 37 200 in L4, 10 600 in L6). In contrast to V1, there are no spiny stellate neurons in V2 L4 or elsewhere in cortex, and infragranular PCs in V2 have spines in L4, which further emphasizes the functional uniqueness of V1 among visual areas (Lund et al. 1981). In L4 of V2, over 90% of cells are pyramidal, with short apical dendrites rising up to L3.

Data on neuron numbers and types for the individual layers of area V5 have not been reported.

Layer-specific quantifications of distinct neuron types would be of paramount importance for modeling.

Connections Between Subcortical Nuclei and V1, V2, and V5

Geniculocortical and Corticogeniculate Connections

Three main pathways, Magno- Parvo- and Koniocellular streams convey visual signals from the retina through the LGN to V1 (Figs 2 and 3 [top], Supplementary Table 1A). These pathways are functionally distinct and computationally assumed to convey independent dimensions of visual information from the retina to the visual cortex (Derrington et al. 1984; Gegenfurtner 2003; Lennie and Movshon 2005). The Magno layers of the LGN, whose cells mediate achromatic vision, have high temporal but low spatial frequency (SF) tuning, and respond nonlinearly to changes in luminance and contrast, send denser projections to V1 L4Cα and sparser and fine axon collaterals to the lower part of L6. The Parvo layers, whose cells mediate red–green contrast, have high spatial but low temporal frequency (TF) tuning, and respond linearly to dynamic stimuli and contrast changes, send their most dominant projection to L4Cβ and sparser projections from a separate population of cells to layers 4A and the upper

part of L6 (Figs 2 and 3 [top]; Hubel and Wiesel 1972; Hendrickson et al. 1978; Blasdel and Lund 1983). In L4C, the thalamic afferents form arborizations covering one monocular column, with a complementary pattern of projection representing the other eye. The width of this periodic arborization shows individual variability from 0.5 to 1.2 mm (Hubel and Wiesel 1972).

Data on single thalamocortical axon arborization patterns are very sparse. An individual Magno axon terminating in L4Cα may divide into two or perhaps more arbors. These arbors form a cluster, each covering 0.3–0.4 mm^2 surface area. Each cluster contains 6490 synapses (mean from Blasdel and Lund 1983 and Freund et al. 1989; both studies reported data from one filled axon).

The corresponding coverage for the Parvo pathway axon terminal in L4Cβ is much smaller, 0.067 mm^2 (Blasdel and Lund 1983). Freund et al. (1989) filled two Parvo axons and counted on average 3154 synapses/axon cluster. A single Parvo axon in L4A formed a single terminal field with a honeycomb-like pattern, including 764 boutons covering 0.058 mm^2 surface area (Blasdel and Lund 1983). Assuming an average of 2.2 synapses/bouton [mean of Parvo synapses per bouton, from (Freund et al. 1989)], this would result in 1681 synapses/axon cluster.

The Konio stream of the macaque LGN, a fraction of which mediates blue–yellow contrast, is organized in six cellular layers (K1–K6), located between and below the four Parvo and two Magno layers (Figs 2 and 3 [top];(Casagrande et al. 2007). Layers K1–K2 project mainly to V1 L1 (47% of K1–K2 projecting boutons) and the upper part of L3 (38% of boutons; named 3A in Casagrande et al. 2007), with minor projections to L2 (3%) and the lower part of L3 (12%); each axon has on average 134 boutons (range 55–255, $N = 9$ axons). Cells in the LGN layers K3–K6 project mainly to the lower part of V1 L3 (93% of boutons; named 3Bα in Casagrande et al. 2007), targeting mainly the CO-rich blobs (Hendry and Yoshioka 1994; Casagrande et al. 2007), with minor projections to L1 (2%), upper L3 (3%), and L4A (2%); each axon has on average 217 boutons (range 90–430, $N = 9$ axons). The number of thalamocortical synapses per bouton in the Konio stream is unknown.

A subset of L6 neurons in V1 projects back to LGN (Wiser and Callaway 1996; Briggs et al. 2016) in a stream-specific manner (Lund et al. 1975), that is, separate cells in L6A and 6B project to the Parvo and Magno layers, respectively, each with functional properties resembling their LGN targets (Briggs and Usrey 2009). In addition to V1, also some V2 L6 neurons project back to LGN (Briggs et al. 2016). Because the target layers in LGN are unknown for these V2 projections, these connections are omitted in Figure 2 and Supplementary Table 1A.

The LGN also projects directly to V2 (Bullier and Kennedy 1983; Markov et al. 2011), and about 1% of, or 8000, LGN neurons project directly to V5 (Sincich et al. 2004). Interestingly, these geniculate connections to V2 and to V5 both originate primarily from the intercalated Konio layers (Bullier and Kennedy 1983; Sincich et al. 2004), which represent the phylogenetically older blue–yellow color system (Carlos and Silveira 2003). Unfortunately, we do not know the target layers in V2 and V5 for this LGN projection, and thus we have omitted these connections from Figure 2 and Supplementary Table 1A.

Other Subcortical Afferents to V1, V2, and V5

Of all subcortical inputs to V1, one of the largest arises from the claustrum (0.3% of all retrogradely labeled neurons after injections in V1), whereas for LGN inputs, this fraction does not exceed 0.2% (Markov et al. 2011). V1 receives also afferents from the pulvinar (to layers 1 and 2, Lund et al. 1981) and the amygdala (Markov et al. 2011). The largest fraction of subcortical projecting neurons to V2 arises from both inferior and lateral pulvinar (Benevento and Rezak 1976; Trojanowski and Jacobson 1976) [0.3% (Markov et al. 2011), terminating primarily in L3B (Lund et al. 1981)], and from the claustrum (0.5%; Markov et al. 2011). In addition, V1 and V2 receive sparse projections from thalamic intralaminar nuclei and the nucleus basalis of Meynert (Kennedy and Bullier 1985). Area V5 also receives projections from the pulvinar (Adams et al. 2000) and claustrum (Gattass et al. 2014). Unlike the very localized inputs from LGN and pulvinar, inputs from the claustrum and thalamic intralaminar nuclei show much larger spread (Perkel et al. 1986).

Interareal Connections

Overview of Corticocortical Connections

Interareal connections between V1, V2, and V5 have been reviewed previously (Zeki and Shipp 1988; Felleman and Van Essen 1991; Merigan and Maunsell 1993; Gattass et al. 2005; Sincich and Horton 2005; Angelucci and Bressloff 2006; Nassi and Callaway 2009). Later, quantitative studies have provided significant new information on the relative connection strengths between cortical areas (Markov et al. 2011; Markov et al. 2014a), and online databases have also enabled targeted searches of existing literature (Kötter 2004; Bakker et al. 2012). In addition to visual inputs, V1 and V2 receive feedback (FB) from auditory and parietal cortices suggesting that multimodal signals are available to all visual areas, not just to association areas positioned at higher levels of the anatomical hierarchy (Falchier et al. 2002; Rockland and Ojima 2003).

The macaque cortex consists of a moderately dense network of functional areas, where one estimate suggests that 66% of possible direct connections between two areas exist, with the number of projecting neurons between any two areas spanning a scale of 10^5 (Markov et al. 2014a). With the caution that these numbers are based mainly on one species, *M. fascicularis*, and thus cannot be applied to other macaque species, these data suggest that the number of projecting neurons $p(d)$ follows an exponential cortical distance rule (Markov et al. 2013):

$$p(d) = ce^{-\lambda d}; \text{SD of } p(d) = \sqrt{\mu + \frac{\mu^2}{\theta}},$$

where c is a scaling constant, λ is the spatial decay constant, and d is distance across white matter. Markov et al. (2013) reported $\lambda = 0.19$ mm^{-1} for macaques, interpreting it to reflect the cost of wiring. Variability of λ between monkeys was not reported, but individual injections show SD, which follows the mean, fitting best to negative binomial model with dispersion parameter $\theta = 7.6$ (Markov et al. 2011).

Between areas, the fraction of supragranular presynaptic projection neurons is correlated with hierarchical distance from the target area, so that in lower order areas, supragranular projection neurons predominate, whereas in higher order areas, projection neurons lay primarily in infragranular layers (Barone et al. 2000; Markov et al. 2013).

A large fraction of V1 excitatory cells sends their axons into the white matter. In a study based on nine monkeys (*Macaca radiata*; (Callaway and Wiser 1996), white matter-projecting axons were found for 50% (3/6 cells) of excitatory cells in layers 2/3A, 60% (3/5 cells) in L3B, 83% (5/6 cells) in L4B, and 19% in L5 (3/16

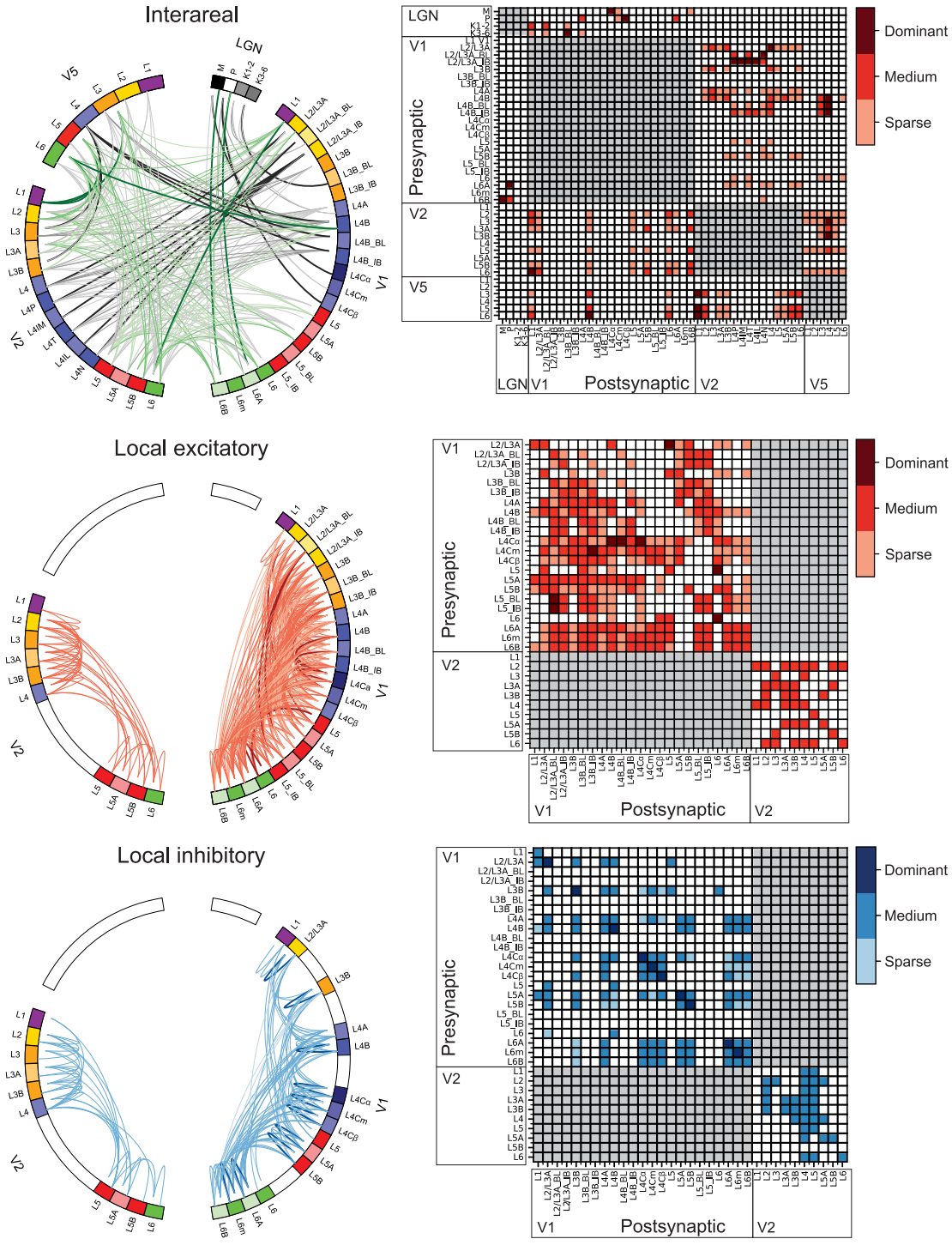

Figure 2. Connections between LGN, V1, V2, and V5 and within V1 and V2. For references, see Supplementary Table 1D. Top, middle, and bottom rows indicate interareal, intra-areal excitatory, and intra-areal inhibitory connections, respectively. LEFT COLUMN: Connectograms (Krzywinski et al. 2009) showing connections between distinct layers. Each colored segment in the circular perimeter indicates a cortical layer, sublayer, or CO compartment. Line width and color intensity indicate the robustness of the connection. Unknown strengths are marked as medium; for V2 interlaminar connections (middle and bottom connectograms), the paucity and qualitative character of the available studies did not allow us to estimate connection strength. The origin (soma) of a projection neuron is marked as a line slightly displaced from the outer edge of the circle, while its termination (axon terminals) is marked as a line reaching the outer edge of the circle. "Top left": Interareal connections and connections between LGN and areas V1, V2, and V5. Black lines indicate FF connections and green lines FB connections. V2 L4P = L4 pale stripe (no distinction between lateral/medial stripes), L4IM = L4 interstripe (or pale stripe) medial, L4T = L4 thick stripe, L4IL = L4 interstripe (or pale) lateral, L4N = L4 thin stripe. All interareal connections are excitatory. "Middle left": Local excitatory connections. "Bottom left": Local inhibitory connections; none of the studies reviewed here identified the CO compartments. RIGHT COLUMN: Matrix of the connections. No connection (white squares) indicates that the connection either does not exist or was not studied. Red squares indicate excitatory connections and blue squares inhibitory connections. Color intensity indicates the strength of the connection.

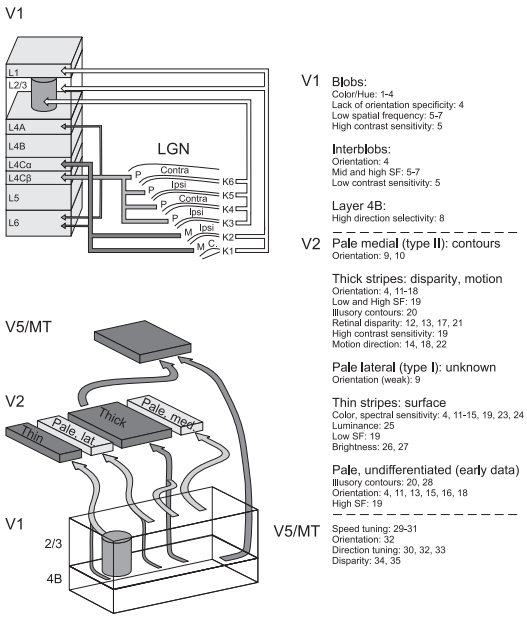

Figure 3. FF pathways and specialization of functional compartments in LGN, V1, V2, and V5. TOP: Main LGN to V1 pathways (Hendrickson et al. 1978; Blasdel and Lund 1983; Kaplan 2003; Casagrande et al. 2007). Arrow thickness indicates the relative contribution of Parvo and Magno geniculocortical afferents to the different V1 layers. BOTTOM: Main FF pathways between V1, V2, and V5 (Sincich and Horton 2002; Sincich et al. 2007, 2010; Federer et al. 2013). In both top and bottom schematics, additional sparse connections were omitted for clarity. The CO compartments of V1 and V2 contain multiple functional feature maps, and their constituent neurons show specific RF tuning properties, as indicated on the right. Numbers refer to the following references: 1, Tootell et al. (1988a); 2, Landisman and Ts'o (2002); 3, Xiao et al. (2007); 4, Lu and Roe (2008); 5, Edwards et al. (1995); 6, Silverman et al. (1989); 7, Tootell et al. (1988a); 8, Gur and Snodderly (2007); 9, Felleman et al. (2015); 10, Shipp and Zeki (2002a); 11, Shipp and Zeki (2002b); 12, DeYoe and Van Essen (1985); 13, Roe and Ts'o (1995); 14, Munk et al. (1995); 15, Gegenfurtner et al. (1996); 16, Vanduffel et al. (2002); 17, Ts'O et al. (2001); 18, Levitt et al. (1994a); 19, Tootell and Hamilton (1989); 20, Peterhans and von der Heydt (1993); 21, Chen et al. (2008); 22, Lu et al. (2010); 23, Tootell et al. (2004); 24, Xiao et al. (2003); 25, Wang et al. (2007); 26, Lu and Roe (2007); 27, Roe et al. (2005); 28, Heider et al. (2000); 29, Lagae et al. (1993); 30, Maunsell and Van Essen (1983c); 31, Perrone and Thiele (2001); 32, Albright (1984); 33, Dubner and Zeki (1971); 34, Maunsell and Van Essen (1983a); and 35, DeAngelis and Newsome (1999).

cells). In L6, 28% of cells (16/56 cells; 8 monkeys; *M. radiata*) projected to white matter (Wiser and Callaway 1996). Many projection neurons have also extensive intra and interlaminar local collaterals in V1 (Lund and Boothe 1975; Callaway and Wiser 1996; Yarch et al. 2017).

Markov et al. (2014a) have provided important quantitative data on corticocortical connections (Table 3). They injected retrograde tracers in multiple areas, including V1, V2, and V5, counted the number of cells projecting to these areas, and calculated each area's relative input from different areas. V1 receives about three fourths of its interareal input from V2, and vice versa V2 receives three fourths of its input from V1, representing the densest mutual connectivity in the macaque brain. Rockland (1997) estimated that under each mm^2 of cortex, 14 600 V1 neurons send feedforward (FF) projections to V2 (range 8800–21 600), whereas 11 300 (range 8000–12 800) V2 neurons send FB projections to V1. Moreover, 41–68% of V2 L6 neurons provide FB connections to V1 (Rockland 1994).

Given this robust mutual connectivity between V1 and V2, it is interesting that these two areas exert rather different impacts

Table 3 Relative strength of mutual connections between V1, V2, and V5

V1 to V2		V2 to V1	
Mean	76.4%	Mean	73.2%
Std	2.7%	Std	3.5%
Min	73.3%	Min	68.3%
Max	78.3%	Max	76.6%
V1 to V5		V5 to V1	
Mean	1.9%	Mean	5.9%
		Std	1.1%
		Min	5.2%
		Max	7.8%
V2 to V5		V5 to V2	
Mean	11.9%	Mean	3.6%
		Std	0.6%
		Min	3.0%
		Max	4.1%

Numbers indicate the percent of total presynaptic neurons, labeled in the source area after a retrograde tracer injection in the target area (e.g., after a tracer injection in V2, 76.4 ± 2.7% of all labeled presynaptic cells reside in V1); (Markov et al. 2014a). Data from http://core-nets.org/index.php?action=download. Data are from adult monkeys; five hemispheres were injected in V1 (four monkeys, all females), three in V2 (two monkeys, all males), and one in V5 (female).

on each other's neuronal responses; whereas inactivating V1 silences V2 (reviewed in Bullier et al. 1994), inactivating V2 has much subtler effects on V1 responses (Hupé et al. 1998, 2001; Nassi et al. 2013; Nurminen et al. 2018) indicating that the anatomical strength of a connection does not dictate its physiological strength. Other factors, such as the strength of synaptic connections and their location on the postsynaptic cell, are likely important determinants of physiological strength of a connection.

The proportion of afferent connections to V5 arising from V1 and V2, as well as the FB connections from V5 to V1 and V2, are clearly sparser, but still significant (Table 3).

Many studies suggest that connections between V1 and V2, V2 and V5, and V1 and V5 are retinotopically organized in such a way that neighboring patches of cortex represent neighboring regions in the visual field (Ungerleider and Mishkin 1979; Weller and Kaas 1983; Ungerleider and Desimone 1986b; Shipp et al. 1989). However, the cell populations projecting from V1 to V2 and V5 are largely distinct (Sincich and Horton 2003; Nassi and Callaway 2007).

Figure 2 (top), Figure 3 (bottom), and Supplementary Table 1A summarize the interareal connectivity between V1, V2, and V5. CO staining in V2 reveals a periodic stripe pattern consisting of dark thick and thin stripes with interleaving pale stripes (Fig. 3 [bottom]). A robust connection from V1 to V2 arises from L2/3A interblobs, followed by the projection from L2/3A blobs. A second robust, but generally sparser (except for the projection to thick CO stripes), pathway arises from L4B interblob and blob columns, and sparse inputs arise from layers 3B, 4A, 5B, and 6A. In V2, the majority of V1 afferents terminate in L4 of the different CO stripes (thick, thin, and pale), with minor terminations in layers 3A, 3B, 5A, 5B, and 6. The FB projections from V2 to V1 arise predominantly from L6, followed by layers 2–3A, with minor efferent connections from layers 3B and 5B. Earlier studies, using less sensitive anterograde tracers or bidirectional tracers, suggested that V2 FB projections terminate predominantly in L1 of V1, with only minor projections or collaterals to other layers (2/3 and 5) (Rockland and Pandya 1979; Lund et al. 1981; Rockland and Virga 1989; Rockland 1994; Gattas

et al. 1997). Recent studies, using more sensitive and exclusively anterograde viral vectors of fluorescent proteins, however, have shown strong V2 FB projections not only to L1 but also to L5B and 6B of V1, with sparser terminations in layers 2/3, 4B, 5A, and 6A (Ta'afua et al. 2018). This arrangement suggests that the layer-wise connectivity between V1 and V2 is largely reciprocal, that is, the same V1 layers sending FF projections to V2 receive direct FB connections from V2. Such symmetry suggests the existence of FF–FB loops, for fast modulation of incoming V1 FF signals by V2 FB connections. However, the lack of FB connections arising from L4, the dominant FB arising from L6, and the dominant FB terminations in L1 are exception to an exact FF–FB reciprocity, showing anatomical asymmetry. How this asymmetry affects the cells' integrative function is unclear. Connections to dendrites distant from the soma, such as the FB to L1, may contact the apical dendrites of PCs with somata in deeper layers. However, studies in rodents and modeling work have shown that the postsynaptic signals relayed at these distal sites are attenuated (Rall 1962; Williams and Stuart 2002), and their effect may depend on coincident inputs onto the proximal dendrite (Larkum et al. 2004; Larkum 2013). These dendritic intracellular interactions may affect the layer-specific timing of visual responses carried by FF, horizontal, and FB connections (Self et al. 2013; Bijanzadeh et al. 2018).

FF connections from V1 to V5 arise from layers 4B (both blobs and interblobs) and 6 and target primarily L4 and less so L3 of V5. Similar to V2-to-V1 FB, FB connections from V5 originate predominantly in L6, with smaller contributions from layers 5 and 3, while L4 sends no FB to V1. FB projections from V5 to V1 terminate predominantly in layers 4B and 6 (Maunsell and Van Essen 1983b; Ungerleider and Desimone 1986b; Shipp et al. 1989), that is, the source layers of the V1-to-V5 FF projection. Only in the peripheral visual field (>10° eccentricity) does V5 FB target also V1 L1 (Ungerleider and Desimone 1986b; Shipp et al. 1989). FF connections from V2 to V5 arise predominantly from L3B but also from layers 2, 3A, and 5, with a minor contribution from L6. These connections terminate mainly in L4 of V5 with some spread into the neighboring layers 3 and 5. FB from V5 to V2 arises from V5 layers 3, 5, and 6 and terminates predominantly in V2 layers 1 and 6 but also 2, 3A, and 5B, with minor terminations also in layers 3B and 5A. In contrast to V2, where the supragranular origin of FB connections is mainly from L2–3A, the supragranular FB from V5 seems to originate only from L3; while Rockland and Pandaya (1979) reported it to originate in L3A, Weller and Kaas (1983) did not specify from which subdivision of L3 V5 FB originates.

Characteristics of Connections Between V1 and V2

The major target layer of V1-to-V2 projections is L4, where axon terminals form 0.2- to 0.5-mm-wide clusters; 1–3 clusters are arranged in 0.2- (single cluster) to 1.2-mm-long (multiple clusters) and 0.3-mm-wide terminal fields (Rockland and Virga 1990; Anderson and Martin 2009). Sparse axonal terminations also occur contiguously in layers 3 and 5 (Rockland and Pandya 1979). In V2, the most frequent targets of V1 FF projections are the dendritic spines of excitatory neurons, with sparse terminations onto shafts, the latter mainly (about 60%) onto inhibitory neurons (Anderson and Martin 2009). Of the spines receiving V1 FF projections, only 19% receive a second inhibitory synapse in addition to excitatory synapses.

As mentioned above, macaque V2 has four CO stripe compartments (thick, thin, and 2 pale stripes), each with unique afferent and efferent connectivity (Fig. 2 [top], Fig. 3 [bottom], Supplementary Table 1A). Retrograde tracer injections confined to distinct V2 stripes result in spatially segregated clusters of labeled somata in V1, which align preferentially with distinct V1 CO compartments (blobs or interblobs), suggesting parallel FF pathways from V1 to V2 (Livingstone and Hubel 1984a, 1988a; Sincich and Horton 2002; Federer et al. 2013). Livingstone and Hubel (1984b, 1988a) first proposed a tripartite model of V1-to-V2 projections. This model was later modified by Sincich and Horton (2002) and, subsequently, Federer et al. (2013) as illustrated in Figure 3 (bottom). According to this model, thin stripes receive projections from CO blobs and thick and pale stripes from interblobs. V1 projections to all stripes arise predominantly from L2–3 with sparse projections from layers 4A and 5–6; projections from L4B are densest to thick stripes, moderate to thin stripes, and one set of pale stripes (type I, also termed pale-lateral as they are located laterally to thick stripes) and absent to the second set of pale stripes (type II, also termed pale-medial). Importantly, this segregation is not strict, as all stripe types receive sparser projections from both blobs and interblobs.

After paired injections of different retrograde tracers into thick and pale stripes, 16% of all V1 labeled neurons were double labeled in the interblobs (Sincich and Horton 2002); even smaller percentages of double-labeled neurons were found after paired retrograde tracer injections into thin and pale stripes (Sincich and Horton 2002) or pale-lateral and pale-medial stripes (1–3% of all labeled neurons, Federer et al. 2013), demonstrating that different stripe types receive inputs predominantly from different V1 cells, but at least some common inputs from the same cells, and that the segregation of inputs is more marked for thin versus thick/pale stripes compared with thick versus pale or pale-lateral versus pale-medial stripes.

Using intra-V2 injections of a glycoprotein-deleted rabies virus carrying the gene for green fluorescent protein (GFP), Nassi and Callaway (2007) found that on average 17% of V1 L4B neurons projecting to V2 had spiny stellate morphology and 83% ($N = 2$ hemispheres, 82% and 85%, respectively) had pyramidal morphology. By confining injections of the same virus to thick or thin stripes, Yarch et al. (2019) reported that on average > 60% of L4B inputs to thick stripes and about 40% to thin stripes arises from stellate cells and the rest from pyramids. The difference between the results of Nassi and Callaway (2007) and those of Yarch et al. (2019) suggests that most V1 L4B stellate cells that project to V2 target the thick stripes and that pale stripes receive dominant or exclusive V1 L4B inputs from PCs. Alternatively, viral injections in the two studies may have been confined to different subcompartments or layers within the stripes, or the virus differentially infected different populations of L4B cells in the two studies. Yarch et al. (2019) additionally fully reconstructed the intra-V1 axon arbors of single L4B neurons projecting to thick stripes; using unbiased cluster analysis of these neurons' intra-V1 laminar axon projection patterns, they identified at least two (possibly three) major classes within this L4B subpopulation. Most reconstructed neurons (65%, 15/23 neurons) belonged to Class 1, sending narrowly focused axonal projections to L2/3 and laterally extending projections to layers 4B and 5. Class 2 cells (26%), instead, sent collaterals mainly to L5 and the rare Class 3 cells (9%) predominantly to L6. The somata of all these cell classes lay preferentially outside CO blobs, and their axon projections in all layers also avoided CO blobs, indicating that the intra-V1 connections of L4B neurons projecting to thick stripes preserve segregation between blobs and interblobs.

Rockland and Virga (1989) reported that V2 to V1 FB axons form terminal clusters in V1 with extents of 4.0×10^6 μm^3 (range 0.2×10^6–15.4×10^6), primarily in L1, with sparser terminations in layers 2 and 5. Most single FB axons travel 0.75–2 mm in L1, sending clusters at 350–650 μm intervals (Rockland 1994). In L5, however, the terminals travel < 0.75 mm. The density of boutons varies from 3 to 15 boutons/100 μm of axon.

Using more sensitive viral vectors of GFP (AAV9) confined to distinct V2 stripes, Angelucci and colleagues (Federer et al. 2015; Ta'afua et al. 2018) have recently reported dominant V2 FB projections to V1 layers 1, 2A, 5B, and 6B and sparser projections to 2B, 3, 5A, and 6A, from all stripe types. Sparse, but significant, projections to L4B were observed after thick and pale-lateral stripe injections but were virtually absent after thin stripe injections. Moreover, V2 FB projections mimicked the parallel organization of the reciprocal FF V1-to-V2 pathways: in all V1 layers of termination, thin stripes projected predominantly to blobs and pale and thick stripes to interblobs.

Characteristics of V5 Afferent Pathways

The most direct LGN Magno inputs reach V5 trisynaptically via V1 layers 4Cα and 4B. In contrast, most Parvo input travels a longer route, via V2, to reach V5 (cf., Nassi and Callaway 2006, Figure 3). More specifically, the pyramidal neurons in V1 L4B receive Magno and Parvo inputs from both layers 4Cα (via direct 4Cα-to-4B projections) and 4Cβ (via 4Cβ-to-3 projections contacting the apical dendrites of L4B pyramids in L3), whereas the 4B spiny stellate neurons receive only Magno input from L4Cα (Yabuta et al. 2001). L4B spiny stellates then carry Magno data directly to V5 (Nassi and Callaway 2007). After injections of retrograde tracers into V5, Nassi and Callaway (2007) found that on average 76% ($N = 3$ hemispheres, range 67–93%) of the labeled cells in V1 L4B had spiny stellate morphology and only 24% had pyramidal morphology. This contrasted with the much larger fraction of pyramids (~80%) projecting to V2. Moreover, the V5-projecting V1 L4B neurons were larger in size compared with the V2-projecting ones, and the V5-projecting PCs were more likely to reside under CO blobs and have longer dendritic trees extending more often up to L1. Other studies found that L4B cells projecting to V5 are equally located under blobs and interblobs (Shipp et al. 1989; Sincich and Horton 2003) and that V1 projections to V5 arise predominantly from L4B (97.8% of V1 inputs) and sparsely from L6 projection (2.2%; Nhan and Callaway 2012).

Individual axons from V1 terminate into 1.0- to 1.8-mm-wide patchy fields in L3, L4, and L6 of area V5 (Rockland 1989; Anderson et al. 1998). Each axonal branch forms up to four terminal arbors up to 250 μm in diameter in the L4 and L3 and up to 50–100 μm in L6 (Rockland 1989). The axons form excitatory synapses with dendritic spines (54%; with the largest synapses, mean area 0.127 μm^2, SEM 0.011), shafts (33%; 0.071 μm^2, SEM 0.07), and somata (13%; 0.031 μm^2, SEM 0.008). All connections to the soma and 26% of those on shafts were found to be on inhibitory postsynaptic cells, the remainder (78% of all connections) being on excitatory cells (Anderson et al. 1998). These authors estimated that of the $5–10 \times 10^3$ synapses present on single V5 neurons, only few hundreds are made by V1 afferents, which is analogous to LGN to V1 projections where a small number of synapses have a disproportionally strong impact on the target neurons.

Similar to V1 projections, V2 afferent axons to V5 form terminal patches in L3–4, each patch being up to 200–250 μm in width, with an interpatch distance of up to 600 μm (Rockland 1995). Moreover, as in V1, most V2 afferent synapses land onto spines (67% in L4, 82% in L2/3), and only 4–6% of synapses onto L4 neurons are made by V2 afferent axons (Anderson and Martin 2002). In contrast to V1 projections, some V2 axon arbors extend from L4 upward into L1; moreover, V2 afferent axons are thinner than V1 afferents (diameter of about 3.0 μm in V1 vs. 1.0 μm in V2) and send no collaterals to L6 (Rockland 1995; Anderson and Martin 2002).

Divergence and Convergence in FF and FB Connections

Some of the earliest anatomical studies of interareal connections reported that the tangential extents of the FF and FB connectional fields were asymmetric (reviewed in Zeki and Shipp 1988). The forward connections converged to a local region in higher order areas, and it was hypothesized that they represent the anatomical substrate for the increasing RF size of neurons along the cortical hierarchy. In contrast, the backward projecting system was typically more divergent, thus possibly serving widespread modulation of low-order areas.

Angelucci et al. 2002b tested the hypothesis that widespread FB connections from extrastriate cortical areas provide an anatomical substrate for contextual modulation of V1 neuron responses arising from outside the neurons' classical RF (also termed the RF surround). By combining tracer injections with electrophysiological recordings at the injection site and in the cortical region of expected tracer transport, these authors were able to compare the spatial extent of extrastriate FB connections to V1 with the spatial extent of V1 neurons' classical and extraclassical RFs. Anterograde tracer injections confined to the V2 upper layers produced a pattern of labeled patchy FB terminations in V1 upper layers. Injections including also the deep V2 layers additionally produced less patchy and more extensive terminal FB label in layers 5/6. The diameter of the V2 FB axon terminal field in V1 was 6.8 ± 0.4 mm (mean ± SEM, range 6.4–7.6 mm), while FB terminations from V5 extended over 13.4 ± 0.5 mm (range 12.9–13.9) mm in V1. These authors also made injections of retrograde tracers into V1 and measured the extent of the retrogradely labeled fields of neurons in V2 and V5 sending convergent FB projections to the injected V1 region. When converted to visuotopic coordinates, on average, the V2 and V5 L5/6 FB neurons labeled by small injections of retrograde tracers in V1 encompassed a visual field region of 3.8 ± 0.6 degrees and 26.6 ± 3.0 degrees, respectively, in diameter. In contrast, the field of long-range intra-V1 horizontal connections converging to the same V1 injection sited was only 2.9 ± 0.4 degrees in diameter. Expressed in units of V1 classical RF size, the visuotopic extents of V2 FB fields correspond to 4.0 ± 0.4 times (range 2.7–5.3; for FB from V2 L2/3) and 4.6 ± 0.2 times (4.0–5.1; for FB from V2 L5/6) the size of the classical RF of V1 neurons. FB from V5 L2/3 and 5/6, instead, extends 15.0 and 25.0 ± 4.0 (21–29) times, respectively, the V1 neurons' classical RF size. Importantly, the FB fields to V1 are much larger than the extent of visual field encompassed by the intra-V1 long-range horizontal connections, which, instead, encompass 2.7 (L2/3) to 3.7 (L4B) times the classical RF size of V1 cells. In conclusion, horizontal connections can mediate contextual integration of visual signals from just outside the V1 neurons' RF (the "near surround"), while FB connections provide V1 cells with a much larger area for integrating visual signals arising from the most distant regions of the RF surround (the "far surround").

Intra-areal Connections

Local cortical connectivity is complex. For example, a recently implemented model of the microcircuit of rat somatosensory cortex comprises almost 2000 connection types between 55 morphological cell types (Markram et al. 2015). For modeling purposes, the complex connectivity needs to be simplified to basic principles, including distance distributions, major local interlaminar pathways, and main connection motifs for excitatory and inhibitory neurons. This information is only partially available for macaque cortex.

Overall, there seem to be two major categories of connections, long-range (millimeters-long) horizontal connections, which are most prominent within the lamina of origin (Fisken et al. 1975; Rockland and Lund 1983; Angelucci et al. 2002b), and short local connections, which often cross layer boundaries.

Horizontal Connectivity

Most inputs to cortical neurons arise from their local neighborhood. On average 79% of incoming axons to any cortical point originate within the same functional area (Markov et al. 2011). In addition, the intra-areal intrinsic connectivity is highly local (Barone et al. 2000; Markov et al. 2011), that is, following injection of a retrograde tracer in cortex, the number of resulting retrogradely labeled neurons drops as a function of distance (d) from the injected site:

$$\text{Number of neurons} \sim \frac{1}{e^{\lambda d}}.$$

For example, in V1 lambda is 1/0.23 mm, resulting in 95% of labeled presynaptic neurons being located within 2.2 mm of the injection site; in V2 the corresponding value is 1.8 mm. On average, across the studied cortical areas, 95% of labeled intrinsic neurons are within 1.9 mm of the injected site (Markov et al. 2011). Moreover, on average 63% of these intrinsic retrogradely labeled V1 neurons are supragranular, and the drop in number as a function of distance appears similar in the supra- and infragranular layers (Barone et al. 2000).

The extent of local horizontal connections varies in different layers of V1. Using bidirectional tracers (which label both axon terminals anterogradely and cell bodies retrogradely), Angelucci et al. 2002b showed average horizontal extents of 3 mm (radius from the injection site) in L2/3, 3.4 mm in L4B/upper 4Cα, and 4 mm in L5/6. The largest axonal extents in these layers were 4.5, 5.0, and 4.8 mm, respectively. In contrast, connections in the remainder of L4C seem to be highly local, extending laterally mainly within one functional column (up to 0.2-mm radius, Fisken et al. 1975; Katz et al. 1989).

The number of synapses between any two horizontally connected cells appears to be very low: only 2 out of 33 postsynaptic dendritic branches (sample of two neurons) received two inputs from the same presynaptic neuron (McGuire et al. 1991). This study, however, looked only at single branches and, thus, could not exclude targets on different dendritic branches of the same postsynaptic cell.

Functional Organization of Horizontal Connections

Figure 4 depicts the relative extent of horizontal connections in V1, V2, and V5, and Table 4 summarizes key measurements. Horizontal connections extend over progressively larger distances in higher order areas (Amir et al. 1993).

In layers 2/3 of V1, horizontal connections labeled by retrograde tracer injections into V1 form patches of axon terminals and somata around the injection site (Rockland and Lund 1983; Angelucci et al. 2002b; Tanigawa et al. 2005). Single tracer injections label on average 11 (range 3–21) patches (Yoshioka et al. 1996; Tanigawa et al. 2005), each about 0.1–0.2 mm wide, which repeat at 0.5–0.6 mm intervals (Rockland and Lund 1983). The 0.2-mm patch diameter matches the width of the dendritic fields of PCs in the supragranular layers and, together with the characteristic interpatch distance, reflects the preference of these connections to link V1 domains with similar functional

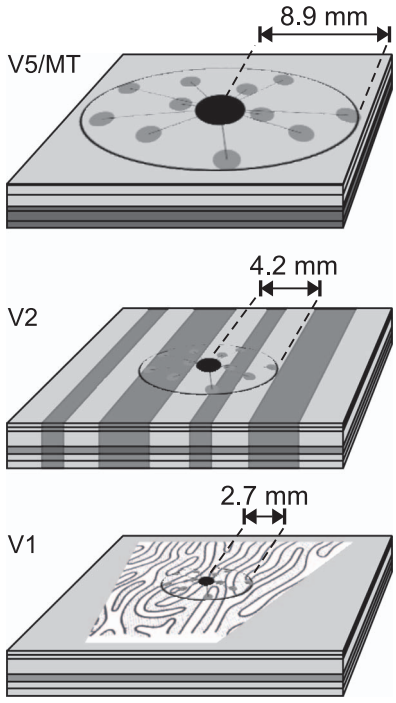

Figure 4. Extent of intra-areal horizontal connections in the tangential domain of areas V1, V2, and V5. Horizontal connections in V1 are most prominent in L2/3 and 5 but exist also in L4B/upper 4Cα and 6 (Amir et al. 1993; Angelucci et al. 2002b). In V2, horizontally spreading connections emerge from L2 and L3 and some from L5 and L6 (Levitt et al. 1994b). In V5, locally projecting neurons are predominantly found in L2 and L3 and, following deep layer injections, also in L6 (Ahmed et al. 2012). In the center of each cortical slab is a halo (black dot) of dense, unspecific local connectivity, surrounded by more specific patches of terminal clusters (gray dots). In V1, the OD pattern (modified from LeVay et al. 1975) and, in V2, the schematics of the CO bands are approximately at scale. In V5, the darker shading in layers 4–6 depicts heavier myelination. The horizontal connection extents are average maxima across studies from *M. fascicularis* and *M. mulatta*: V1, (Amir et al. 1993; Angelucci et al. 2002b); V2 (Amir et al. 1993); and V5 (Ahmed et al. 2012).

Table 4 Summary of horizontal connectivity

	V1	V2	V5
Most distant terminal cluster	2.7 (2.1–2.9)	4.1 (4.0–4.2)	8.9
Anisotropy ratio	1.7 (1.6–1.8)	1.6	1.2
Cluster size	0.21 (0.18–0.23)	0.25 (0.25–0.25)	0.52
Intercluster separation	0.61	0.88 (0.60–1.15)	2.3
References	1–2, 4–5	1, 3	6

Mean (range) across studies. Distances are in mm. Data from: 1, Amir et al. (1993); 2, Malach et al. (1993); 3, Levitt et al. (1994b); 4, Yoshioka et al. (1996); 5, Angelucci et al. (2002b); and 6, Ahmed et al. (2012).

tuning (Malach et al. 1993; Yoshioka et al. 1996). Patchy horizontal connections are also prominent in L5 (Lund et al. 1993).

Tracer injections targeted to specific orientation preference domain in the V1 orientation map send horizontal connections preferentially (70%) to other V1 domains with similar orientation preference (±45°) as that of the injected site. In the local neighborhood of the injected site, the connection targets show wider orientation diversity (Malach et al. 1993).

Horizontal connections in V1 layer 2/3 also prefer domains of similar ocular dominance (OD) and CO compartment (blob/interblob, Livingstone and Hubel 1984b; Yoshioka et al. 1996). Tracer injections targeted to a specific OD column resulted in labeled patches of horizontal connections, of which on average 54% resided in the surrounding OD columns representing the same eye territory, 18% at the border between the left and right eye representation, and 28% in the opposite eye territory. For tracer injections targeted to blob/interblob domains, 71% of connection targets remained in the same domain, the rest were located at blob/interblob borders or into the opposite CO compartment (Yoshioka et al. 1996).

Taken together, in layers 2 and 3 of V1, the horizontal connectivity is locally (within dendritic and axonal field) not specific to functional domains, but long-range connections form terminal patches with a preference for similar domain cells.

In thalamorecipient L4Cβ, the dendritic fields of both spiny and nonspiny stellate cells seem to avoid crossing OD boundaries, whereas axons of both cell classes cross to the opposite domain. Since these axons are only about 100-µm long, they nevertheless mainly remain in their home eye column (Katz et al. 1989). Functionally, this results in strictly monocular cells in this layer (Hubel and Wiesel 1968).

Horizontal connections in layers 4B/upper4Cα also show some domain-specific clustering. When columnar tracer injections encompass L2 to upper L4Cα, the clusters of horizontal connections in L2/3 and those in L4B/upper4Cα are vertically aligned, but clusters in L4B/upper4Cα are band-like rather than patch-like as in L2/3 (Angelucci et al. 2002a; Lund et al. 2003).

In L6, a specialized class of large pyramidal Meynert cells shows little clustering of their horizontal connections and appears to form diffuse terminations (Li et al. 2003). In other layers, the horizontal connectivity in relation to functional domains has not been systemically studied.

The distribution of horizontal connections is anisotropic. The ratio between the long and short axes of the antero- and retrogradely labeled connection fields ranges from 1.5 in L4B/upper 4Cα to 1.8 in L5/6 (Angelucci et al. 2002b). Interestingly, the visual field representation of these horizontal connection fields appears isotropic, that is, their spatial anisotropy in cortex translates to an isotropic distribution in visual field. This results from the anisotropic columnar organization in V1, primarily due to the OD columns, interrupting an otherwise smooth retinotopic representation (Blasdel and Campbell 2001).

In V2, horizontal connections are also patchy (Rockland 1985; Amir et al. 1993; Levitt et al. 1994b). From each injection site, efferent axons travel in layers 1–3 to form 10–15 terminal patches, each 0.25–0.3 mm wide. The patches are found up to 4 mm away from the injection site, with a gamma-like, positively skewed, distribution, peaking at 1-mm distance. The patches form an oval field, with median longer/shorter axis ratio of 1.6 (range 1–3.8) and the longer axis of the field being oriented orthogonal to the CO stripes. Given the anisotropy of visual field representation in V2, due to the presence of CO stripes, the connections seem to connect roughly a circular area of visual field. After tracer injections confined to the upper layers, some labeled horizontal connection are also observed in L5.

The stripe specificity of horizontal connections in V2 remains unclear. It appears that over short distances, they cross CO stripe boundaries (Levitt et al. 1994b), but over longer projection distances, they preferentially target the same stripe type as that of the injected site (Baldwin et al. 2012). Interestingly, GABAergic connections seem to create an oval-shaped connectivity along, rather than across, the CO stripes, in contrast to excitatory connections (Kritzer et al. 1992); their maximum lateral spread is also shorter, 1.4 mm in superficial layers and 1.1 mm in the infragranular layers. Functionally, this difference in excitatory versus inhibitory topography would seem to indicate that V2 excitatory horizontal connections combine signals from different visual processing streams, while the more local inhibitory connections suppress nearby activation within one stream.

In V5, horizontal connections form the longest-range connections, with clusters up to 10 mm from the injection site (Ahmed et al. 2012). A tracer injection in the upper layers labels horizontal connections that are restricted to supragranular layers, whereas a tracer injection in the deep layers labels horizontal axons in both supragranular and L6 neurons with a similar distribution of clusters (mean space between clusters 2 mm).

Overview of Interlaminar Connections

Interlaminar connections in V1 and V2 (Figs. 2 [middle, bottom], Supplementary Table 1B–D) have been previously reviewed (Gilbert 1983; Lund 1988; Lund et al. 1994; Levitt et al. 1996a; Callaway 1998a; Douglas and Martin 2004). We found no intrinsic interlaminar connectivity studies of macaque V5.

From a modeling perspective, it is interesting that lamination might reflect a developmental hierarchy. The major laminar borders and layer-specific connections develop first, guided by ontogenetic molecular markers, whereas sublamina-specific connectivity (e.g., axons targeting 3 vs. 4B, 4Cα vs. 4Cβ) might emerge postnatally, guided by either molecular markers or visual input (Callaway 1998b). Eventually, interlaminar connectivity becomes highly complex with multiple unique combinations of layer inputs (Sawatari and Callaway 2000; Nassi and Callaway 2009).

The excitatory and inhibitory local circuit neurons have been clearly distinguished in the literature, as light and electron microscopic observations allow straightforward identification of excitatory cells, as having spinous dendrites and forming asymmetric synapses, in contrast to inhibitory cells, which instead have smooth dendrites and form symmetric synapses. However, there are sparser data describing the extent of axonal spread in a target layer. Moreover, in these studies, cell samples were typically small, precluding statistical analyses, and the distance covered by the projecting axons is often reported only as largest extent within the small sample. An even greater challenge is the classification of inhibitory and excitatory cells into different morphological subtypes and describing the subtype-specific connectivity. While attempts to classify neurons into distinct subtypes have been made, the relative proportions of the different subtypes and the statistics of their inputs and outputs are sporadic and largely missing in macaques. However, a general rule that has emerged from these studies is that both excitatory and inhibitory neuron types typically project strongly within their home layer.

Excitatory Interlaminar Connections

In Figure 2 (middle) and in Supplementary Table 1B, we report, separately for V1 and V2, the layer location of the somata giving rise to interlaminar projections and a semiquantitative description of their axonal target layers.

V1 excitatory neuron connectivity. Excitatory neurons in L4Cα and L4Cβ project strongly to their home layer, but they also target 4Cm, a sublayer of cells, which occupies the middle of L4C between the α and β sublayers and which receives only sparse direct LGN connections. L4Cα sends robust projections to layers 3B and 4B, which align with CO blobs, but sparser projections also to other layers, except L1 and 5B. L4Cβ sends a robust projection to L3B, which instead aligns with both interblobs and blobs. L4Cβ also sends more moderate projections to other layers, except 1 and 5B. The L3B blob and interblob compartments seem to distribute efferent connections primarily to corresponding blob or interblob compartments, respectively, in other layers (2/3A, 4B (sparse) and 5), and L3B interblob neurons in addition project to 5A. L2/3A interlaminar connections are partially selective for blob/interblob divisions, emphasizing connections within their home compartment, but not totally avoiding crossing CO boundaries. L4A, which receives direct LGN Parvo input, projects to L3B interblobs, but also to layers 2/3A, 4B, and 5A. Cells in L4B blobs seem to be targeting mainly interblobs within 4B itself and in L5; in contrast, cells in L4B interblobs target primarily interblobs in these layers. L4B projections to layers 2/3A and 3B, instead, terminate in CO blobs, regardless of whether their soma sits in a blob or interblob column. However, Yarch et al. (2017) have recently shown that the L4B output cells that project to the thick CO stripes of V2 do not obey this local L4B to L3-blob connectivity rule; instead, these cells have somata that typically lay at a blob border or an interblob, and in L3 they avoid blobs but project to the same CO compartment where their soma resides, that is, blob border or interblob.

L5A and 5B neurons seem to be widely projecting to supragranular and granular layers, avoiding, however, L4Cm. L5A and 5B both send some axons to L6, too. L6 cells are connected to almost all other layers, with some emphasis on L4C.

In V1, the mutual connectivity between the L5 and 6 sublayers has not been studied. Sublayers 5A and 5B are most likely highly interconnected (Kisvarday et al. 1989; Briggs and Callaway 2005), but this has not been explicitly studied. The illustrations in Wiser and Callaway (1996), together with the quantification of PC types in L6A, L6 m, and L6B, seem to suggest that there is dense mutual sublayer connectivity between these L6 subdivisions.

L6 PCs have been classified into subgroups based on their specific laminar targets (Wiser and Callaway 1996). L6 neurons either target the L4C sublayers and L4A in different combinations avoiding all other layers (type I) or avoid L4C and show strong mutual connectivity within L6 (type II). The L6 projections to CO blobs versus interblobs seem to be nonspecific (Wiser and Callaway 1996), and only a subset of type I pyramids project selectively to particular OD columns in L4C (Wiser and Callaway 1997).

V2 excitatory neuron connectivity. For V2 interlaminar connections, we found only three studies (Valverde 1978; Lund et al. 1981; Levitt et al. 1994b), limiting the robustness of the connectivity graph and especially the classification of connection strength (Fig. 2 [middle], Supplementary Table 1B). First, local excitatory connections show the typical intralaminar self-connectivity. Input layer 4 sends projections to supragranular layers, whereas no direct infragranular projection has been reported from this layer. L3B connects to layers 3A, 5A, and 2. L3A projects to L3B, 2, and 5B. L2 sends axonal projections to every layer except 5A. L5A connects back to L4 and sends projections to both 3A and 3B. L5B projects to layers 3A and 3B. Finally, L6 sends efferent axons to all other layers, except L1.

Inhibitory Interlaminar Connections

Jennifer Lund and colleagues studied the inhibitory neurons and their interlaminar connections of V1 in a series of four papers (Lund 1987; Lund et al. 1988; Lund and Yoshioka 1991; Lund and Wu 1997), based on Golgi impregnation of thick tissue sections and reconstructions of single neurons within single sections. The limitations of these studies are the incomplete impregnation and the fact that neurons cannot be reconstructed beyond individual impregnated sections, therefore leading to incomplete neuron reconstructions. The inhibitory local circuit neurons of V2, instead, have been studied mainly together with excitatory neurons (Valverde 1978; Lund et al. 1981; Levitt et al. 1994b). Kritzer et al. (1992) used 3H-nipecotic acid to retrogradely label GABAergic cells. Their data suggest that inhibitory connections are made nearly across all layers in both V1 and V2, with the probability of connections decreasing with laminar distance. This is consistent with data in rodents (Markram et al. 2015). Due to poor confinement of tracer injections to single layers in Kritzer et al. (1992), in Figure 2 and Supplementary Table 1, we have omitted most data from this study.

V1 inhibitory neuron connectivity. The dendritic fields of inhibitory interneurons often spread vertically outside the layer where the parent soma is located (Lund 1987). Albeit spreading to other layers, the dendritic fields spread uniformly, sampling apparently unselectively across their depth. Horizontally, the dendritic fields of smooth inhibitory neurons in supragranular layers 1–4B are local, measuring 250–350 µm in diameter (Lund and Yoshioka 1991; Lund and Wu 1997).

It is safe to claim that more than half of the inhibitory synapses are formed within the layer of the parent soma. The exceptions in Figure 2 (bottom) and Supplementary Table 1 are L1, for which sparse data do not allow quantitative estimates, and L4A, which is too narrow to include most of the local axonal tree. In contrast to dendrites, the axons may also cross layers, but without sprouting, targeting specific upper or lower layers. A subset of inhibitory neurons with somata either in L4Cα or L4Cβ sends axons to the opposite geniculocortical stream (i.e., L4C$\alpha \geq$ L4Cβ, L4A or L4C$\beta \geq$ L4Cα), potentially causing cross-inhibition between the Magno and Parvo streams (Lund 1987). Horizontally, the axons of inhibitory neurons may spread considerable distances, albeit much less than the horizontal spread of excitatory cells; the largest distances are reached by the L2/3 wide-arbor Basket cells, whose axon terminals may reach up to 1.5 mm from the soma (Lund and Wu 1997).

The layer-specific connectivity in relation to CO compartments has not been extensively studied for inhibitory interneurons; thus, this is omitted in Figure 2 (bottom). Overall, however, the few available studies suggest that inhibitory connections preserve CO specificity (Kritzer et al. 1992), similar to excitatory neurons.

L4Cα interneurons connect to all 4C sublayers, as well as to layers 4B, 4A, 3B, 5A, and the bottom of L6. Sparse axonal projections from L4Cα target, in addition, layers 5B and 6A. L4Cβ interneurons show similar connectivity as those of 4Cα, but with emphasis on L6A instead of 6B, and a missing projection to L4B.

L4B interneurons target layers 3B, 4A, both 5A and 5B, and all L6 sublayers. Sparse projections reach L1 and L2/3A. L4A inhibitory neurons have similar targets as those of L4B. In contrast to L4B, L4A inhibitory neurons send weaker projections to L6, while targeting L4C (4Cm, as well as, weakly, 4Cα and 4Cβ). L3B inhibitory neurons target predominantly L4A, and moderately layers 2/3A, 4B, 4Cm, 5A, and 5B, and all three sublayers of L6. L2/3A interneurons send dominant projections to layers 1, 3B, 4A, 4B and 5B, and sparse connections to L6. L1 interneurons send axons to layers 2/3A, 3B, and 4B, but not to L4C or infragranular layers. L5A sends inhibitory axons to layers 1, 3B, as well as to all L4C and L6 sublayers. L5B is very different from 5A, as it sends inhibitory axon projections to layers 2/3A, 5A, and 6A and sparse projections to 3B, 4A, 4B, and the bottom two L6 sublayers. L6 interneurons project to layers 4A, all 4C sublayers, 5, and heavily to all L6 sublayers.

The two most apparent distinctions between inhibitory and excitatory intrinsic connectivity within V1 are in L1, which has more extensive inhibitory than excitatory connectivity, and in L6, which inhibits only the thin L4A, but excites most supragranular layers. Horizontally, the inhibitory connections do not seem to form terminal axon clusters, as excitatory neurons do, but their axon density decreases continuously as a function of distance (Kritzer et al. 1992).

Lund et al. (1988) suggested that some L5B inhibitory neurons send axons to the white matter, which would be an important exception to the rule that all white matter tracts are excitatory. Later, long-range inhibitory projections have been found in many species and systems (Caputi et al. 2013), but they are sparse, originating from about 0.5% of neocortical GABA neurons in mice (Tamamaki and Tomioka 2010). In macaques, long-distance projecting inhibitory neurons are predominantly inside the white matter (81%), and in the gray matter, they reside predominantly in L3 (12%; L1 0.5%, L2 3%, L5 2%, L6 1.5%, L4 none, Tomioka and Rockland 2007). The functional role of these neurons has remained unknown.

V2 inhibitory neuron connectivity. In V2, the inhibitory connectivity graph is sparse due to availability of only sparse data and will likely need to be modified when new data will become available. The extensive connectivity of L4 is mainly reported in Kritzer et al. (1992), but the ^{3}H-nipecotic acid retrograde tracing data seem to show an overall more diffusely connected system across layers than, for example, the Golgi-stained single-cell data of Lund et al. (1981).

Interlaminar FB

Despite the paucity of data on V2 excitatory interlaminar connectivity compared with V1, some similarities between the two areas are apparent.

The input layers 4C and 4 in V1 and V2, respectively, preferentially target the supragranular layers, particularly 3B, but also 3A and 2. In contrast, L2 avoids projecting back to these input layers. Given the lack of direct L2 FB to L4, it may be interesting to investigate whether L2 provides FB-like inputs to other layers.

L6 projects to all layers containing excitatory neurons. Given the large RFs and their broader tuning in L6 (Gur et al. 2005), L6 interlaminar projections could provide fast intracolumnar FB inputs relaying local contextual information to more sharply tuned cells in other layers. Moreover, as V1 L6 (together with L1) is a major recipient of interareal FB projections arising from higher visual areas (as discussed above), L6 is also in a position to relay global contextual information (arising from the "far surround" of V1 neurons) to all V1 layers to which it projects. This idea is consistent with the observation that V1 L6 (but also L1) shows the shortest onset latency of local field potential (LFP) responses (i.e., is activated earlier than other layers) following presentation of a visual stimulus in the far RF surround of neurons in a recorded V1 column (Bijanzadeh et al. 2018). These early far surround responses in V1 L6 (and L1) are thought to be generated by interareal FB connections from extrastriate cortex (Angelucci et al. 2002b; Angelucci and Bressloff 2006; Angelucci et al. 2017).

Anatomical reconstruction of microcircuits remains a challenge. Here, we have reviewed studies, most of which are based on injections of neuroanatomical tracers, followed by microscopy analysis of labeled tracts or reconstructions of single labeled neurons across serial tissue sections. These approaches have well-recognized limitations, for example, difficulty and errors in serial section reconstruction of single neurons, variability in tracer transport across injections and animals, etc. Serial block surface imaging with electron microscopy (EM) allows for accurate and high-resolution 3D reconstruction of circuits, at the level of synapses (Denk and Horstmann 2004), and recently automated transmission EM has allowed synapse-level analysis of excitatory network in rodents (Lee et al. 2016). These methods are, however, difficult to apply to large tissue blocks, for example, encompassing macaque V1, let alone the whole macaque visual cortex. Recently developed methods based on viral vector-mediated high-resolution fluorescent labeling of neuronal circuits (Luo et al. 2008), followed by tissue clearing, to render intact tissue blocks optically transparent (Chung et al. 2013), and deep-tissue imaging (Denk et al. 1990; Stelzer 2015), to image labeled neurons through intact tissue blocks, are making it possible to characterize primate and even human (Mortazavi et al. 2019) brain circuits at cellular resolution. However, the lack of algorithmic and computational solutions to visualize, analyze, and reconstruct the massive amount of neuronal data that are being collected remains a major challenge that requires development of cyberinfrastructure and computational approaches (Venkat et al. 2016; Petruzza et al. 2017, 2018).

Functional Anatomy

Cell Structure and Synaptic Coverage

The heterogeneity of cellular structures and their development across brain areas has been previously reviewed (Elston 2003; Elston and Fujita 2014). In V1, dendritic morphology does not seem to change as a function of RF eccentricity. V1 L3 pyramidal neurons show similar number of dendritic branches, total dendritic length, and basal dendritic fields across eccentricities (Oga et al. 2016).

In contrast, along the hierarchy of visual areas, dendritic field size and complexity increase. For L3 PCs, the area of basal dendrites, which form the largest extent of horizontal dendritic field coverage, increases from V1 ($36 \pm 5.5 \times 10^3$ μm^2; range 27–49×10^3 μm^2) to V2 ($45 \pm 10 \times 10^3$ μm^2; range 18–66×10^3 μm^2), to V5 ($84 \pm 11 \times 10^3$ μm^2; range 56–104×10^3 μm^2; Elston and Rosa 1997). Moreover, there are more dendritic branches per unit area in V5 than in V1 or V2.

The L3 pyramidal neuron basal dendritic field area is somewhat larger in the CO blobs ($27 \pm 11 \times 10^3$ μm^2; range 5–49×10^3 μm^2) of V1 compared with the interblobs ($20 \pm 10 \times 10^3$ μm^2; range 6–51×10^3 μm^2; Elston and Rosa 1998). There was a similar trend for larger dendritic fields in the V2 thin stripes compared with pale stripes, but without statistical significance.

The V1 L5 PC basal dendritic area ($40 \pm 19 \times 10^3$ μm^2;(Oga et al. 2017) is comparable to that of L3 mentioned above.

The total length of the apical dendrite of V1 L3 pyramidal neurons averages (mean ± SD) 1530 ± 114 μm (trunk 9% of total length, oblique branches 50%, and tuft 41%) with 15.3 ± 1.2 branch points, and the total length of the basal dendrites averages 1659 ± 138 μm with 16.8 ± 1.8 branch points (Gilman et al. 2017). The apical dendrites have on average 855 ± 92 spines and the basal dendrites 1030 ± 157 spines.

The apical dendrite spine necks, retrieved from two PCs in V1 L3, range from 0.2 to 1.2 μm in width, most being 0.4–0.8 μm (McGuire et al. 1991).

The proportion of LGN afferent synapses relative to the total number of synapses (summarized in Peters et al. 1994) in Magno-recipient L4Cα was originally reported to be between 1.3% and 1.9% (18–40/neuron) and in Parvo-recipient L4Cβ 3.7–8.7% (37–191/neuron; O'Kusky and Colonnier 1982b; Beaulieu et al. 1992). The corresponding number of synapses per number of neurons was (mean ± SD) $1.9 \pm 0.2 \times 10^3$ in L4Cα and $1.4 \pm 0.2 \times 10^3$ in L4Cβ (O'Kusky and Colonnier 1982b). A recent quantitative 3D microscopy study (Garcia-Marin et al. 2017) reported higher average thalamocortical synaptic densities: 0.46 (range 0.39–0.53) $\times 10^8$/mm^3 in L4Cα and 0.82 (range 0.70–0.93) $\times 10^8$/mm^3 in L4Cβ. These densities correspond to 15% of all excitatory synapses in L4Cα (197/neuron) and 20% in L4Cβ (200/neuron) being thalamocortical synapses, suggesting a much stronger thalamocortical drive than previously assumed. In L4A the thalamocortical synapses had an anisotropic honeycomb arrangement, with thalamocortical synaptic density of 0.35 (0.23–0.49) $\times 10^8$/mm^3. In L6 the corresponding density was 0.13 (0.08–0.16) $\times 10^8$/mm^3.

There might be a trend for higher inhibitory synaptic coverage of the spiny stellate cell somas compared with PC somas. Otherwise different layers and animals showed variable (between 20% and 60% of circumference) inhibitory synapse coverage of their somata (Lund et al. 2001).

Although V1 L2–3 CO blobs and interblobs differ in several physiological properties, their pyramidal neurons show no significant difference in soma area, spine density, number of basal dendrites, dendritic radius, or dendritic branching pattern (Hubener and Bolz 1992). Moreover, the dendritic fields of the PCs cross blob boundaries suggesting continuous dendritic sampling.

Proportions and Synaptic Densities of Excitatory and Inhibitory Connections in V1

About 85–90% of V1 connections are excitatory, forming asymmetric synapses with postsynaptic cells, the rest being inhibitory, that is, forming symmetric synapses (Fisken et al. 1975; Medalla and Luebke 2015). The horizontal and interlaminar connections seem to target dendritic spines and shafts in similar proportions. Labeling single V1 L3 PCs by intracellular injections of HRP (N = 2), McGuire et al. (1991) studied both local and long-range excitatory connections of layer 2/3 PCs and found that 75% of synapses are made onto dendritic spines and 25% onto shafts. This is consistent with the overall population of V1 layer 2/3 excitatory neurons, which make 75% of their synaptic contacts onto dendritic spines, with a mean density of $365 \pm 54 \times 10^6$ synapses/mm^3 (mean ± SEM), and 25% with shafts, with a mean density of $119 \pm 10 \times 10^6$/mm^3 (Medalla and Luebke 2015). Inhibitory neurons, instead, target spines more seldom (34%; mean density of $33 \pm 7 \times 10^6$/mm^3) than dendritic shafts (66%; $62 \pm 24 \times 10^6$/mm^3, Medalla and Luebke 2015). Although lower in volumetric density, the density of synapses along inhibitory cells' dendritic shafts (average of 1.9 synapses/μm, range 0.8–3.9 synapses/μm) is much higher than the density of synapses along excitatory cells' dendrites (average of 0.3 synapses/μm, range 0.1–0.5 synapses/μm, McGuire et al. 1991). A similar synaptic density was found on the cell bodies of the smooth inhibitory cells, with about 200–300 synapses over the whole soma surface.

Diversity of Response Properties in V1 and V2 Layers

Layers 4Cα and 4Cβ show response properties similar to those of their respective afferent Magno and Parvo LGN neurons (Blasdel and Fitzpatrick 1984). The minimum response field size of neurons (defined as the RF size measured using small bar or square stimuli) is about two times larger in L4Cα than in L4Cβ. Correspondingly, the contrast threshold increases up to 3.5-fold from the top of L4Cα to the bottom of L4Cβ. In supragranular layers, in both blob and interblob regions, cells receive input from both Magno and Parvo streams (Nealey and Maunsell 1994).

Gur and colleagues (Gur et al. 2005; Gur and Snodderly 2007, 2008) measured RF properties of neurons in different V1 layers in alert monkeys and found significant variability. Orientation and direction tuning in V1 show high laminar variability, with the input layers, 4Cα and 4Cβ, 4A and 6 housing less selective units (Gur et al. 2005). In addition, the input layers show higher spontaneous firing rates [layer: mean (range across cells) in light/mean (range) in darkness, Hz: L4A: 27 (1–74)/24 (3–113); L4Cα: 13 (<1–52)/10 (<1–28); L4Cβ: 30 (11–59)/17 (5–28); L6: 13 (<1—27 Hz)/10 (<1–25) Hz] compared with the output layers whose mean firing rates are generally < 1 Hz [L3: 3 (<1–14)/<1 (one cell); L4B: 1 (<1–3)/1 (<1–3); L5: < 1 (<1–<1)/<1 (<1–<1),(from Fig. 5 (top) in Snodderly and Gur 1995)]. The high spontaneous firing rate in the input layers may be inherited from the LGN, where the mean spontaneous firing rate is about 13 Hz (Spear et al. 1994). Mapping RF size with bars of light increments or decrements, Gur et al. (2005) found that V1 layers receiving direct input from LGN (L4A, L4Cα, L4Cβ, L6) have larger RFs than other layers (L2/3, L4B, L4Cm, L5). These findings challenged earlier studies of layer 4C, which reported much smaller RF sizes (Schiller et al. 1976; Hubel and Wiesel 1977; Blasdel and Fitzpatrick 1984). This discrepancy can perhaps be attributed to the effects of anesthesia in the earlier studies, which is known to alter LGN activity and multiple RF properties downstream of LGN (Gur et al. 2005). As an alternative explanation, the discrepancy may emerge from less accurate laminar differentiation and RF mapping in awake animals. Moreover, the method and visual stimuli used to map RF size affect the measurements (Angelucci and Bressloff 2006). For example, estimates of RF sizes based on the cortical spread of deoxyglucose uptake (Tootell et al. 1988b) allow accurate laminar definition and indicate that layers 2 and 6 have the widest RFs (spread could not be quantified), followed by L5 (half the spread from the edge of the stimulus, about 0.5 mm). L4Cα and L4B show intermediate spread (0.35 and 0.33 mm, respectively), followed by L3 (0.24 mm), and last L4Cβ (0.14 mm). Importantly, RF sizes vary by a factor of over 10 within layers (Dow et al. 1981; Van Essen and Newsome 1984). Given the inverse relationship between SF and the RF size (Teichert et al. 2007), SF data suggests that large RFs are horizontally clustered into CO blobs (Tootell et al. 1988a).

Most V1 laminae have a median CV, a measure of orientation selectivity (CV = 1−OSI), close to 0.5, but in L3B CV reaches up to 0.75, that is, L3B is less orientation selective (Ringach et al. 2002).

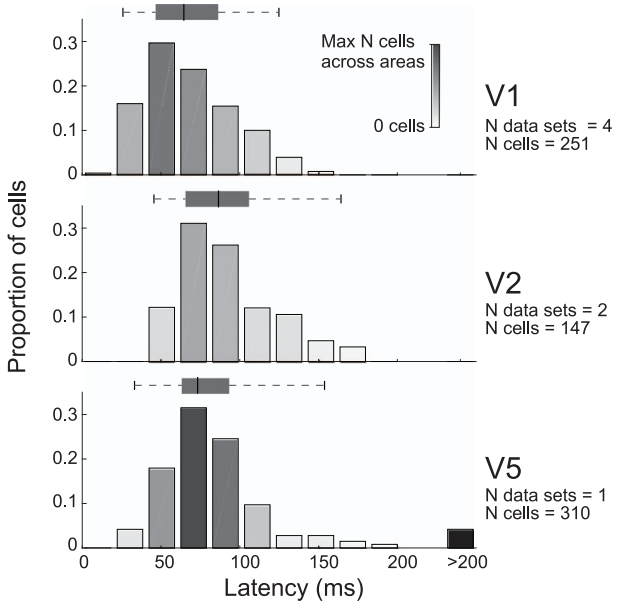

Figure 5. Onset latencies of spiking responses to visual stimulation. The proportions of cells are displayed as a function of latency. The number of distinct figures providing the source data, some in the same papers, are indicated on the right (*N* data sets), together with the total number of cells across the data sets. Bar darkness reflects the number of cells in each bin, normalized to largest number of cells in any of the bins across the three cortical areas. The black bar on the right contains outlier values above the reported cutoff at the tick mark value. The whisker plots indicate the 2.5, 25, 50, 75, and 97.5 percentiles of the data, calculated from the histograms in the original data. Data for V1 are from Maunsell and Gibson (1992) and Nowak et al. (1995), for V2 from Nowak et al. (1995), and for V5 from Raiguel et al. (1989).

L4 has an intricate parcellation, with layers 4A, 4Cα, and 4Cβ having higher CV values and 4Cm much smaller values (Gur et al. 2005). Overall, L4Cm, the sublayer located between 4Cα and 4Cβ, behaves like a noninput layer: it has small RFs, sharp orientation and direction tuning, and low spontaneous activity.

Direction selectivity emerges first in layer 4Cα, and thereafter highly direction selective cells are found in L4Cm, L3, L4B, and L6 (Gur and Snodderly 2007). Downstream from L4Cα, the L4Cm projects to L3, and it has been proposed to represent a third motion pathway from V1 to V2, in addition to the monosynaptic motion pathways arising from direction selective cells in layers 4B and 6 (Gur and Snodderly 2007). In addition to high direction selectivity, cells in L3 show high orientation selectivity and small RFs.

Although typically studied together, L2 is functionally distinct from L3. L2 has higher levels of ongoing activity, less spatially selective RFs, lower orientation selectivity, and no direction selectivity (Gur and Snodderly 2008), thus resembling more the input than output layers of V1.

In V2, the tuning properties of neuronal RFs in different layers show greater similarity than in V1 (Tootell and Hamilton 1989), but L3 has the largest proportion of neurons tuned for visual stimulus parameters (Shipp and Zeki 2002a). The layers receiving FB (L1, L2, L5, and L6) show more often (27% vs. 18%) combined tuning to chromatic and spatial features, suggesting higher order feature binding in these layers than in the layers receiving the FF input (L4 and L3; Shipp et al. 2009).

Diversity of Response Properties in Parallel Pathways

As reviewed in Schiller et al. (1976), the input from the LGN is transformed into five main ways within V1. First, the concentric center-antagonistic surround RFs become a minority in V1, while orientation selectivity emerges. Second, many units become selective for motion direction. Third, many cells acquire "complex" RFs, that is, they respond to both light increments and decrements in their RFs. Fourth, most cells become driven by both eyes and, fifth, become more selective for SF. In addition, some cells show double color opponency (Livingstone and Hubel 1984a), and most cells sum contrast nonlinearly as a function of visual stimulus size (Sceniak et al. 1999; Angelucci et al. 2002b; Cavanaugh et al. 2002).

Table 5 Functional selectivity of V2 stripes

	Thick	Thin	Pale	References
Orientation	85 (51–88)	41 (20–73)	80 (17–96)	1–7
Direction	29 (11–60)	6 (0–21)	13 (0–34)	1–4, 6–7
Color	16 (7–39)	63 (53–86)	27 (12–64)	1, 3–7
Disparity∗	68 (38–77)	21 (10–33)	15 (1–22)	1–2, 5

Median % (range) of cells tuned to the specific visual stimulus parameter (single or multiunit recordings) across seven electrophysiological studies published up to 2002. Modified from the summary of Shipp and Zeki (2002a) with permission from Cambridge University Press. The definitions of tuning and stripe type varied between studies. ∗Disparity or binocular interaction. Data originally from: 1, DeYoe and Van Essen (1985); 2, Peterhans and von der Heydt (1993); 3, Levitt et al. (1994a); 4, Munk et al. (1995); 5, Roe and Ts'o (1995); 6, Gegenfurtner et al. (1996); and 7, Shipp and Zeki (2002a).

The functional architecture of the macaque visual cortex and parallel processing strategies have been more extensively reviewed previously (Casagrande and Royal 2004; Roe 2004; Sincich and Horton 2005; Nassi and Callaway 2009). In brief, Figure 3 (top) depicts the parallel FF pathways from LGN to V1. Afferent geniculate connections from the two eyes remain segregated into OD columns in the input layers of V1 (Hubel and Wiesel 1968). CO blobs are prominent in layers 2/3, but to some extent visible also in layers 1, 4B, 5, and 6 in register with the L2/3 blobs (Horton 1984).

In V2, the CO stripes run orthogonally to the V1/V2 border (Tootell et al. 1983) and are visible, albeit weakly, in most layers and moderately in L4 (Balaram et al. 2014). Across V2, there are about 28 complete sets of CO stripes, a full stripe cycle encompassing on average 4 mm (Olavarria and Van Essen 1997). Table 5 presents a quantitative overview of early electrophysiological single-unit recording studies showing the prevalence of various visual stimulus tuning properties in the different V2 stripes (modified from Shipp and Zeki 2002a). Electrophysiological recordings have demonstrated that many visual response properties are present, albeit with differing prevalence, in all stripe types, and there has been much debate and controversy over the functional specificity, or lack thereof, of distinct stripes (Shipp and Zeki 2002a).

Intrinsic signal optical imaging (OI) is better suited than single-unit recordings to reveal the predominant response within a neuronal population, and, in addition, it allows investigations of the spatial layout of particular visual responses (Blasdel and Salama 1986; Grinvald et al. 1986; Ts'o et al. 1990). This technique has revealed that while neuronal responses to the various visual stimulus parameters are present in most CO compartments, only some of these parameters are systematically mapped within a given compartment.

Figure 3 (right) lists the functional feature selectivity and maps found in the various CO compartments of V1 and V2. Unfortunately, macaque V5 is buried within the superior temporal sulcus and thus is not accessible to OI. In V1, OI has revealed

multiple, and at least partially independent, spatial representations or maps of visual stimulus features, including OD (Blasdel and Salama 1986; Bartfeld and Grinvald 1992; Blasdel 1992), orientation (Bartfeld and Grinvald 1992; Blasdel 1992; Ramsden et al. 2014; Felleman et al. 2015), motion direction (Lu et al. 2010; Hu et al. 2018), binocular disparity (Ts'O et al. 2001; Chen et al. 2008), color (Ts'O et al. 2001; Landisman and Ts'o 2002; Xiao et al. 2003, 2007; Lu and Roe 2008), and brightness/luminance (Roe et al. 2005; Wang et al. 2007) maps.

Based on microelectrode recordings by Hubel and Wiesel (1974a), Braitenberg and Braitenberg (1979) suggested that iso-orientation domains are arranged around orientation singularities. This local "pinwheel-like" organization of orientations was later confirmed by OI of intrinsic signal (Blasdel and Salama 1986; Ts'o et al. 1990; Malach et al. 1993; Landisman and Ts'o 2002; Nauhaus et al. 2008) and two-photon imaging (Nauhaus et al. 2012); for a critical and quantitative analysis of data and models, see (Obermayer and Blasdel 1993; Erwin et al. 1995).

Many studies have examined the relative spatial relationships between these various feature maps in V1. CO blobs (Horton and Hubel 1981) and orientation pinwheel centers (Bartfeld and Grinvald 1992) lie close to the center of OD bands [the latter 300–670 μm wide (LeVay et al. 1975; Horton and Hocking 1996)], but it has remained controversial whether CO blobs and pinwheel centers align with each other (Bartfeld and Grinvald 1992; Blasdel 1992; Obermayer and Blasdel 1993; Lu and Roe 2008). This controversy may have been aggravated by spatial low-pass filtering of neural responses by OI method, which may cause systematic shift of pinwheel centers (Polimeni et al. 2005). In our unpublished data (Merlin et al. 2012), we find a strong association between CO blobs and pinwheel centers, with 85–90% of blobs containing a pinwheel center. However, as pinwheel centers are more numerous than CO blobs in V1, only about 50% of pinwheel centers reside in blobs, therefore suggesting at least partially independent representations of orientation and CO blob maps. The CO blobs seem to coincide with color patches revealed by OI (Lu and Roe 2008), and each color patch contains an orderly and overlapping mapping of responses to distinct hues (Xiao et al. 2007). Despite this partially independent spatial arrangement between orientation pinwheels and color patches, many neurons in V1 are tuned both to color and orientation (Garg et al. 2019).

OI studies have shown that in V2, each CO stripe contains distinct feature maps. Each thick stripe contains one or more (200-μm wide × 1-mm long) topological representation of horizontal retinal disparities (Chen et al. 2008) and a pinwheel-like (about 1-mm wide) or linear representation of different motion directions (Lu et al. 2010). In addition, thick stripes contain ordered orientation maps, which have a diameter of 0.7–1.5 mm (Ts'O et al. 2001). Orientation domains are also found in the pale stripes, in response to both real and illusory contours (Ramsden et al. 2014). Thin stripes represent hue in a systematic fashion [0.07–0.32 wide × 1.3-mm-long bands of varying shape (Xiao et al. 2003)], as well as brightness increments/decrements, the latter forming distinct domains about 0.7 mm apart (Wang et al. 2007).

Physiology

Conduction Velocities and Latencies

The hierarchy of anatomical connections suggests that areas higher in the hierarchy have increasingly longer response latencies to visual stimulation. Experimental evidence supports this claim to some extent for the areas in the occipitotemporal ventral stream, but not for the areas in the parietal and frontal dorsal stream (Schmolesky et al. 1998). In the LGN, the Magno pathway has about a 20-ms lead in response onset relative to the Parvo pathway. In V1, Magno-recipient L4Cα has a corresponding 20-ms lead relative to Parvo-recipient L4Cβ (Nowak et al. 1995). This segregation of latencies continues in the distinct functional compartments of V2 (Bullier and Nowak 1995). Interestingly, the inhibitory responses are as early as the excitatory responses, and the shortest latencies in V2 are in the infragranular layers (Nowak et al. 1995). Thereafter, cortical latencies show a wide distribution (Nowak and Bullier 1997; Schmolesky et al. 1998).

Intracortical conduction velocity has been measured for connections between V1 and V2 (Girard et al. 2001). The following values are a lower bound for the true velocities, because they were estimated assuming direct connections in Cartesian 3D space. The median FF conduction velocity was 3.7 m/s (range 3–6 m/s) and the FB conduction velocity 3.4 m/s (range 1.5–9.5 m/s). This is very fast compared with the conduction velocity of upper layer local V1 axons (0.33 m/s) enabling a rapid FF–FB loop between V1 and V2, particularly faster for the Magno signals, which are conveyed to V2 and back to V1 even before the Parvo signals (80% of optic nerve fibers) arrive to V1. Functionally, Magno signals may prime V1 with contextual/top-down information before Parvo signals arrive to V1, and the loop via extrastriate cortices would be necessary in particular for long-distance interactions (reviewed in Bullier 2001; Bullier et al. 2001; Angelucci and Bressloff 2006). It is noteworthy that Girard et al. (2001) briefly reported that intrinsic horizontal connections within the infragranular layers of V1 may conduct signals faster than upper layer axons (up to 1 m/s), albeit still slower than interareal V1–V2 connections; however, layer differences were not thoroughly characterized in that study and will need further investigation.

Figure 5 shows response onset latencies in areas V1, V2, and V5, and Supplementary Figure 1 shows the cumulative density functions and pairwise uncorrected Mann–Whitney U tests between the areas' median latency values. Response onset latencies overlap in the different areas, but median latency increases from V1 to V5 to V2 (65, 73, and 86 ms, respectively). Onset latencies are strongly dependent on various visual stimulus parameters, especially luminance, which affects integration time in the retina (Mansfield 1973). Moreover, there is significant variability between individual animals in onset latencies (Maunsell and Gibson 1992), which complicates comparison across studies. The study of Schmolesky et al. (1998) compared latencies in different cortical areas. Mean latencies were shortest in V1, 66 ms (SD 10.7, range 34–97), longest in V2, 82 ms (SD 21.1, range 56–118), and intermediate in V5, 72 ms (SD 10.3, range 49–98). These latencies resemble our summary data from multiple studies.

The earliest responses at the top of L4C of V1 cause oscillations at 50–100 Hz (Maunsell and Gibson 1992). Within V2, the thick (median multiunit onset latency 63 ms) and pale (70 ms) stripes show earlier response onset compared with the color-sensitive thin stripes (81 ms;(Munk et al. 1995).

Firing Rate Statistics

The ability of a neural system to provide the same response with high temporal precision is highly dependent on the variance of the input, suggesting neural systems have low intracellular noise (Mainen and Sejnowski 1995). High temporal precision

enables a system to transmit information using less resources. Because neuronal response statistics differs in alert versus anesthetized monkeys, in the discussion below, we specify the state of anesthesia.

In alert monkeys, individual V1 neurons show high temporal precision of spike latency in response to an optimal stimulus, with the median Fano factor (variance/mean) across layers ranging between 0.2 and 0.35 and the mean across V1 being 0.33 ± 0.17 (SD, range across cells < 0.1–1). However, when stimulus contrast is reduced to near threshold, variability increases, and Fano Factors grow closer to 1 (Gur and Snodderly 2006).

The spontaneous spike rate in V1 has an exponential distribution across cells with very low average rates (simple cells 1.2 Hz, $N = 137$, complex cells 4.9 Hz, $N = 245$, anesthetized; Schiller et al. 1976).

Rasch et al. (2011) studied the statistics of V1 spiking during movie viewing in anesthetized monkeys. They found a mean firing rate of 5.1 ± 0.8 (SD) Hz, and an exponential distribution of firing rates, with the exponent being on average -0.8 ± 0.6 s (range -2.4 to -0.2 s). For individual neurons, the Fano factor across multiple presentations of the same stimulus was close to 1 for very short $\leq$10-ms epochs and increased for longer epochs. The population response was, as expected, more reliable for short epochs (smaller Fano factor than for individual neurons), but increased again with longer epochs, suggesting that the firing rates of individual neurons go up and down together. There are probably important differences in firing rate statistics due to anesthesia. First, the Fano factors are significantly lower in awake than anesthetized animals (Gur and Snodderly 2006); moreover, when fixational eye movements are carefully controlled in awake animals (Gur and Snodderly 2006; McFarland et al. 2016), Fano factors cease to increase at longer epochs. In summary, response variability might be significantly smaller in awake visual cortex than previously assumed and stay constant over time.

There are few studies on the firing rate statistics of extrastriate areas. Because Fano factor is affected by anesthesia, epoch length and, in awake animals, fixational eye movements, areas V1, V2, and V5 need to be compared under identical conditions. Yang et al. (2009) compared anesthetized young and old adult monkeys and found that Fano factors in V1 and V5 during drifting grating stimulation are very similar, but increase with age in both areas. Mean Fano factors were (young/old) 1.4/2.4 in V1 and 1.5/2.5 in V5.

Visual Field Representation in Cortex

The representation of the visual field in cortex can be characterized by three parameters, namely, RF size, magnification factor (or it is 2D generalization log conformal mapping), and cortical point image. These representations are however not smooth, because local discontinuities arise from RF scatter and additional dimensions, such as OD (V1; LeVay et al. 1975) and CO (V2) bands (Roe and Ts'o 1995; Shipp and Zeki 2002b).

RF Size

In macaque V1, a typical single-cell response to an enlarging stimulus first shows an increase, then a decrease, until an asymptote is reached (Fig. 6A). The RF size is defined as the stimulus radius at peak response, and the region beyond peak response, where the cells response is suppressed, is termed the surround. This patch-size tuning curve, also called the area summation function (ASF), has been modeled as antagonistic excitatory and inhibitory Gaussian mechanisms, interacting either divisively (ratio of Gaussians, RoG, model; Cavanaugh et al. 2002) or subtractively (difference of Gaussians, DoG, model; Sceniak et al. 1999). In the DoG model, the ASF is:

$$R\,(\mathrm{dia}) = R_0 + K_c \int_{\mathrm{dia}/2}^{\mathrm{dia}/2} e^{-(2x/w_c)^2}\,dx - K_s \int_{\mathrm{dia}/2}^{\mathrm{dia}/2} {}^{-(2x/w_s)^2}\,dx.$$

Here, dia is the diameter of the stimulus, R_0 is the spontaneous firing rate, and K_c, K_s are the gain and w_c, w_s are the extent of the RF center and surround, respectively. The center and surround mechanisms are thought to be generated by distinct connections: the excitatory center primarily by geniculocortical FF and intra-V1 horizontal connections, while the inhibitory surround primarily by both local intra-V1 and interareal FB connections (Angelucci et al. 2002b; Schwabe et al. 2006). A recent review (Angelucci et al. 2017) discusses how the cortical microcircuit might give rise to the ASF.

Neurons show significant variability in their ASFs, and the center and surround extents vary with visual field eccentricity (Fig. 6B,C). In parafoveal V1 (at 3–7° eccentricity)

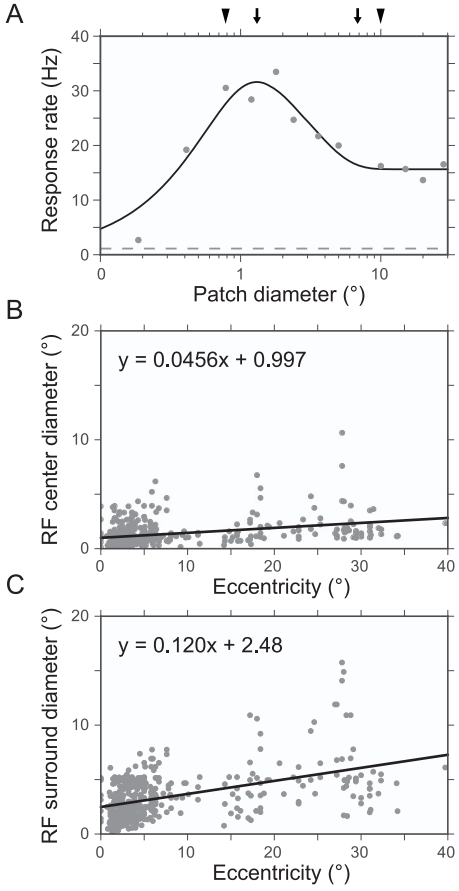

Figure 6. ASF in V1. (*A*) ASF for an example V1 neuron. Solid line represents fit to the data (dots) using the DoG model. Dashed line indicates the mean spontaneous firing rate. Arrows indicate the center and surround diameters obtained using the DoG fit. Arrowheads indicate the center and surround diameters extracted from the empirically measured responses (without any fit). Data from Shushruth et al. (2009). (*B*) RF center diameter with respect to eccentricity. Solid line represents linear fit to the data (dots, $N = 425$). (*C*) RF surround diameter with respect to eccentricity. Solid line represents linear fit to the data (dots, $N = 425$). (*B* and *C*) data from Cavanaugh et al. (2002).

using a high-contrast grating patch increasing in size, the RF radius is measured on average 0.36° ± 0.13° ($N = 79$; range 0.11°–0.82°, Shushruth et al. 2009) and in a different study 0.39° ($N = 148$; eccentricity < 5°, Cavanaugh et al. 2002). These same studies estimated the surround radius to be 1.62° ± 0.62° ($N = 79$; range 0.55°–2.66°) and 2.5° ($N = 148$), respectively. The extents were determined using the DoG fits to the spatial summation data (Shushruth et al. 2009), or directly from the data (Cavanaugh et al. 2002), and defining RF extent as the smallest stimulus radius at the peak of the fitted function, or (for cells that did not show surround suppression) that elicited 95% of the maximum response, and the surround extent as the smallest stimulus for which the response was reduced to 5% of its asymptotic value.

Similarly, in parafoveal V2 (up to 10° eccentricity), the RF radius has been reported to average 0.74° ± 0.50° ($N = 91$; range 0.16°–2.43°) and the surround radius 3.56° ± 1.94° ($N = 83$; range 1.06°–10.55°). Thus in V2, the RF sizes are on average double the sizes of V1 RFs (Shushruth et al. 2009).

For V5, similar nonlinear ASFs as in V1 and V2 have been reported (Pack et al. 2005; Hunter and Born 2011). The peak response appears to be larger than in V1 or V2, in many cases larger than the largest stimulus diameter used for the measurements (30°). The "classical RF" for V5 cells, which is measured using small stimuli rather than gratings of increasing size, was defined by the following equation: size (deg) = 0.72E + 1.35 (Ungerleider and Desimone 1986b). The optimal RF size, corresponding summation field, is about 10 times larger in V5 than in V1 (Albright and Desimone 1987; Maunsell and Van Essen 1987).

Mapping of Visual Field in Cortex

The representation of foveal and parafoveal visual field in V1 can be characterized as (Schwartz 1980, 1994):

$$w = k * \log(z + a), \tag{1}$$

where w is the position in cortex, and z is the position in visual field. The real part of z represents the eccentricity and the imaginary part the polar angle (azimuth) in visual field. The parameters k and a scale the transformation, and a defines the foveal part of the visual field, respectively. For the existing macaque data (Daniel and Whitteridge 1961), Schwartz (1980) used a value of $a = 1$ (in his Figure 1), and k would scale for the individual V1 size.

Schwartz's log mapping has been generalized to cover full field V1, V2, and V3 and to account for shear that conformal (i.e., angle-preserving) mappings cannot model (Polimeni et al. 2006). For numerical simulations, the log mapping provides a straightforward way to map the visual field into cortical coordinates, and it has recently been applied to visual cortical prosthetics as well (Li 2015).

Several previous studies have provided quantitative data on the 1D derivative of the log conformal map, that is, the magnification factor. This is the distance in cortex that represents a given distance in visual field (Daniel and Whitteridge 1961). The parameters k and a of the log conformal mapping are related to the magnification factor (M), because the inverse of the magnification factor can be defined as a linear function of eccentricity (Schwartz 1994):

$$\frac{1}{M} = \frac{a}{k} + \frac{1}{k} * \text{eccentricity}. \tag{2}$$

Although none of the cortical areas show smooth mappings of the visual field, as they all have some substructure, V1 has in early studies been characterized with a single magnification value. Nevertheless, the relation of eccentricity to M^{-1} is not fully linear (Dow et al. 1981) and additionally shows significant horizontal–vertical anisotropy (Tootell et al. 1988b). This anisotropy calls for the aforementioned more comprehensive 2D mapping of the visual cortex than what the M factor allows (Polimeni et al. 2006). However, since these parameters are nonexistent for V5, here, we only report magnification factor.

The area V1 magnification factor, M, as a function of eccentricity is $1/(0.077 + 0.082 \times E)$ mm/deg, as determined using the 2 deoxyglucose method within the central 10° (Tootell et al. 1982), and $1/(0.0404 + 0.116 \times E)$ mm/deg, as determined using electrophysiological recordings within the central 2.5° (Dow et al. 1981) or $1/(0.109 + 0.0637 \times E)$ mm/deg outside the foveal representation (Hubel and Wiesel 1974b; Hubel and Freeman 1977). The slope of M^{-1} at the fovea is about half the slope outside the fovea. The OD columns cause anisotropy by reducing the M factor to about half the value in the direction orthogonal to the OD bands (LeVay et al. 1975).

Early V2 studies reported that the three CO stripes have separate maps of the visual field. The representations are, however, continuous within the same type of stripe (Roe and Ts'o 1995; Shipp and Zeki 2002b). Each of the V2 CO compartments had similar values of magnification factor (interstripes 1.44 mm/deg, thin stripes 1.4 mm/deg, and thick stripes 1.25 mm/deg; Roe and Ts'o 1995).

The magnification factor for area V5 is $1.14 \times E^{-0.76}$ (Gattass and Gross 1981; Albright and Desimone 1987). Because the sizes of cortical areas vary across individuals (as also shown for humans in Amunts et al. 2000), the magnification factors show also individual variability.

Cortical Point Image

The literature on cortical point image, that is, the cortical representation of one point in visual field, is a function of the average cortical RF size and scatter. In V1, the cortical point image shows discrepant values, depending on whether it was measured by electrophysiological recordings or by OI with voltage-sensitive dyes (VSDI). Electrophysiological recordings demonstrate an exponential reduction of the cortical point image with increasing eccentricity. At the fovea the point image approaches 10 mm, whereas in the periphery it is about 1 mm (Dow et al. 1981). In contrast, VSDI shows a constant point image, at least in the parafoveal representation (2°–5°, Palmer et al. 2012). The former method measures action potentials, that is, the output of neurons, whereas the latter measures the subthreshold voltage variations. The discrepancy may, thus, be related to differences in neuronal tuning of synaptic versus action potentials (Jia et al. 2010) and may partially reflect nonlinear mapping from subthreshold to suprathreshold responses (Anderson et al. 2000; Miller and Troyer 2002).

Including LGN in a computational model requires mapping the visual field onto LGN cells and then LGN cells onto visual cortex. The visual field forms retinotopic representation in each Parvo and Magno layer. The LGN represents the visual field with a smaller number of cells than V1, and the ratio of LGN/V1 cell numbers changes as a function of eccentricity (Connolly and Van Essen 1984). The number of cells per square degree of visual field (M_c, cells/deg^2) as a function of eccentricity (E) is given by:

$$M_c = k(a + E)^{-x},$$

where $k = 83\,700$, $a = 1.28$, and $x = 1.96$, for Parvo layers, and $k = 3520$, $a = 3.12$, and $x = 1.56$, for Magno layers. These results suggest that the Magno/Parvo cell ratio in LGN increases by a factor of up to 20 from the fovea to the periphery.

Livingstone and Hubel (1988b), instead, found an approximately equal M/P ratio across eccentricities and suggested that the Connolly and Van Essen (1984) analysis was flawed. The anatomical data of Livingstone and Hubel (1988b) were later challenged by Malpeli et al. (1996), who attributed the discrepancy to a number of potential factors, such as technical issues related to the retrograde transport of the tracers, the omission of the Koniocellular channel (which was discovered in 1994, after the Livingstone and Hubel's study), or a plateau in the magnitude of the magnification factor of the Magno channel at the eccentricities where the tracer injections were placed. Malpeli et al. (1996) showed that the M/P cell ratio in LGN grows by a factor of at least 14 from the fovea to the periphery, thus confirming the original study by Connolly and Van Essen (1984).

Based on the results by Connolly and Van Essen (1984), Schein and de Monasterio (1987) estimated the point images from LGN cells onto V1. Point images are very different for the LGN Parvo and Magno cells' mapping onto the cortex, which results from the different types of scaling of N neurons/unit area as a function of eccentricity. Outside the fovea, the ratio of LGN Parvo cells to unit area of cortex is close to constant, being 550/mm^2 at 1° eccentricity and increasing to 872/mm^2 at 80°. In contrast, the density of Magno cells increases steeply, from 13/mm^2 at 1° to 206/mm^2 at 80° eccentricity. The point image in V1 behaves exactly the opposite, namely, for Parvo cells it decreases steeply with eccentricity, whereas it is almost constant for the Magno cells.

The cortical point image size grows along the ventral stream hierarchy, but stays constant along the dorsal stream, including V5 (Gattass et al. 2005).

Orientation Selectivity

In V1 about 70% of cells are tuned to the orientation of edge stimuli, the rest having non-orientation-sensitive RFs (Bullier and Henry 1980). The distribution of orientation selectivity across V1 layers is discussed in the section "Diversity of response properties in V1 layers" under "Functional anatomy." Quantitatively, orientation selectivity can be defined by two parameters, CV and bandwidth (BW). The CV is a global measure, based on firing rate responses (r) to all orientations (Θ).

$$\mathrm{CV} = 1 - \left| \frac{\sum r e^{i2\theta}}{\sum r} \right|. \quad (3)$$

A CV of zero indicates high orientation selectivity and CV of 1 no selectivity.

Figure 7 and Supplementary Figure 1 show that the CV in V1 is somewhat higher than in V2. All datasets in V1 and V2 were from Goris et al. (2015) and were originally reported as OSI, which we have converted into CV (1−OSI) for the data shown in Figure 7. For V5, Albright (1984) reported that 83% (74/89) of units were tuned for orientation, but, because he quantified orientation tuning as the difference between the max and min responses, this data could not be converted to CV.

Orientation BW is a local measure, defined as the response distribution close to the orientation causing the peak response (Fig. 8, Supplementary Fig. 1).

$$\mathrm{BW}_\theta = \theta_{r_{1/2\max}} - \theta_{r_{1/2}\min}, \quad (4)$$

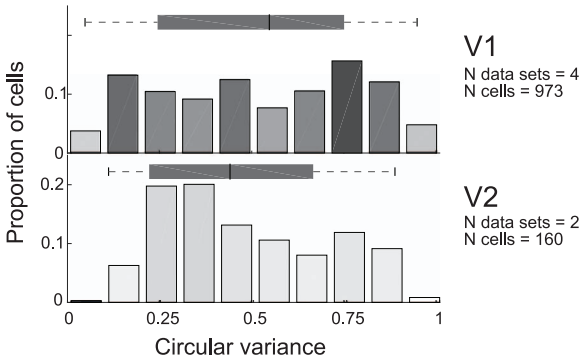

Figure 7. CV. Conventions are as in Figure 5. Data for V1 are from Ringach et al. (2002), Gur et al. (2005), and Goris et al. (2015) and for V2 from Goris et al. (2015).

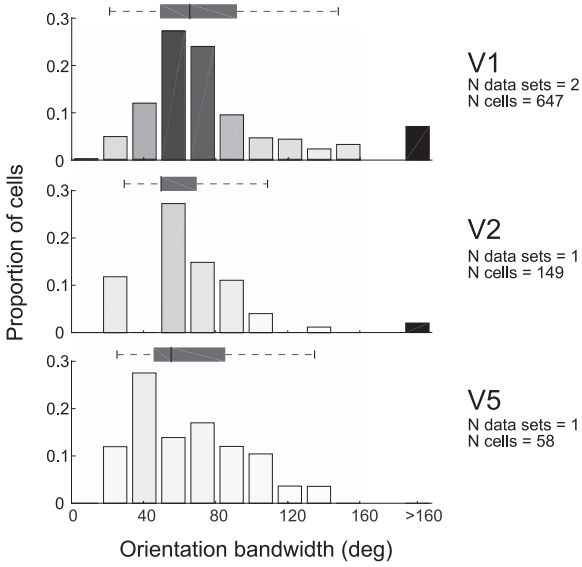

Figure 8. Orientation BW. Conventions are as in Figure 5. Data for V1 are from Ringach et al. (2002) and Gur et al. (2005), for V2 from Levitt et al. (1994a), and for V5 from Albright (1984).

where $\theta_{r_{1/2\max}}$ is the max (min) orientation producing half of the response strength. Studies reporting BW at $1/2^{1/2}$, or 70.7%, of the peak response (Ringach et al. 2002; Gur et al. 2005) instead of the half-height, were transformed to half-height values by assuming a Gaussian distribution of the tuning and multiplying the BW values by the square root of two. The full BW was reported only by Albright (1984), whereas we doubled the values from other studies, which reported the half-BW. The outlier cutoff was set at 160 . Figure 8 and Supplementary Figure 1 demonstrate that orientation BW is slightly wider in V1 than V2, but BW in V5 is not significantly different from V1 and V2.

Direction Selectivity

The direction selectivity index (DSI) reported in Figure 9 is based on nine previous studies. The DSI is defined as follows:

$$\mathrm{DSI} = 1 - \frac{r_{\text{null direction}}}{r_{\text{preferred direction}}}. \quad (5)$$

A DSI = 0 indicates a nondirection selective cell and a DSI = 1 a highly directionally selective cell. Values >1 appear when

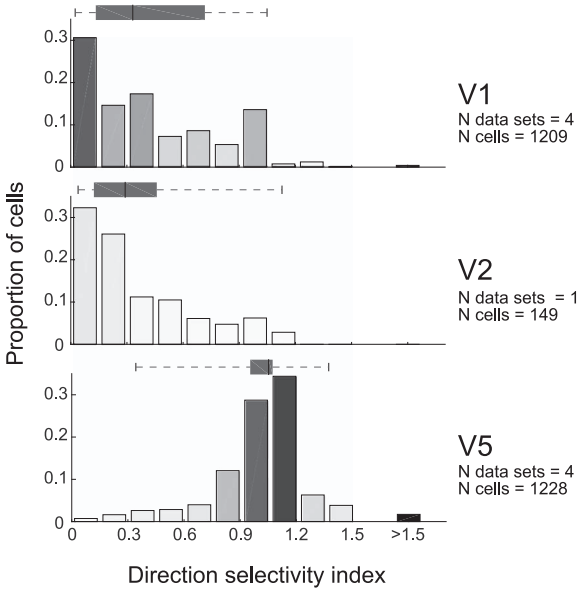

Figure 9. DSI. Conventions are as in Figure 5. Data for V1 are from De Valois et al. (1982b), Albright (1984), Movshon and Newsome (1996), and Wang and Movshon (2016), for V2 from Levitt et al. (1994a), and for V5 from Maunsell and Van Essen (1983c), Albright (1984), Movshon and Newsome (1996), and Wang and Movshon (2016).

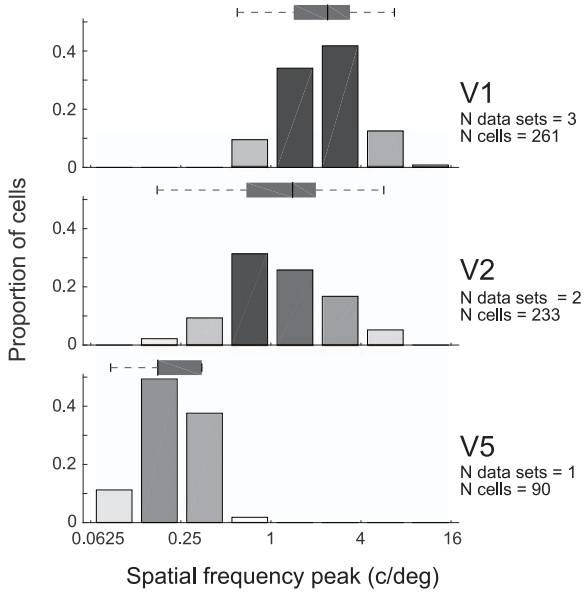

Figure 10. SF peak. Conventions are as in Figure 5. Data for V1 are from De Valois et al. 1982a and Foster et al. (1985), for V2 from Levitt et al. (1994a), and for V5 from Yuan et al. (2014).

the minimal response to stimuli moving in the nonpreferred direction is below the spontaneous firing rate. One study (De Valois et al. 1982b) reported V1 DSI as null/preferred response; in this case the DSI values were recalculated according to equation 5. De Valois et al. did not report values when the null response was below baseline, leading to a max DSI value of 1. However, a similar secondary peak at 1 in V1 was observed in two other data sets. The distribution in Figure 9 did not change much with the De Valois et al. dataset removed (222 cells).

Direction selectivity clearly differs in different areas. Most cells in V1 and V2 are poorly or moderately directionally selective, and the two areas show overlapping distribution, whereas most cells in V5 are strongly directionally selective.

SF Selectivity

In contrast to retina and LGN, where most cells show low-pass characteristics, in visual cortex the majority of cells are band-pass tuned (De Valois et al. 1982a). SF has typically been described by two parameters, the optimal response (peak) and the BW.

Figure 10 shows the distribution of peak SFs in the three cortical areas. The eccentricities of the recorded neurons varied a little between studies, but the range was similar: 2°–5° in V1, 0°–5° in V2, and 0°–8° in V5. The large variability in peak SF precluded setting the outlier threshold at the same cutoff value for all areas, because the low outlier cutoff in V1 (<0.5, De Valois et al. 1982a) encompassed most data in V5. The number of outliers in the original data was low, 4 cells (1.5%) in V1, 22 (9.4%) in V2, and none in V5, thus then could only minimally skew the data in Figure 10.

The peak SF differed significantly between areas, with the highest values in V1, and progressively lower values in V2 and V5 (Supplementary Fig. 1). Functionally, this suggests that the three areas cooperate to detect a wide range of SFs. Because the low SFs would be lost after band-pass filtering in V1, these data in addition suggest either that V2 and V5 has direct access to visual information from LGN (as, indeed, reported in the anatomy section above) or that the few units in V1 tuned to low SFs have high response gain.

Datasets on the SF BW are limited, due to different metrics used to report it in different studies (Fig. 11). The BW in Figure 11 is reported as full width at half-height, on a logarithmic scale (octaves, i.e., $\log_2$):

$$\mathrm{BW_{SF}} = \mathrm{SF}_{r_{1/2\,\max}} - \mathrm{SF}_{r_{1/2\,\min}}. \quad (6)$$

V5 has significantly wider SF BW compared with V1 and V2 (Supplementary Fig. 1). In addition, higher areas showed increasingly higher numbers of cells whose SF BW could not be defined (black bars), as their response did not drop to half of the maximum response on either side of the peak. Cells with such wide-band tuning could be sensitive to sharp edges.

TF Selectivity

Peak TF was characterized in five studies (Fig. 12). The original data have sparse bins, and small numbers of cells, hampering comparison between areas. V5 significantly prefers higher optimal TFs compared with V1 and V2, whereas V2 shows a distribution with somewhat lower TF values than V1 (Supplementary Fig. 1).

The TF BW (Fig. 13) was characterized in the literature only for a minority of cells, most not reaching the threshold of 50% response strength and most of them having low-pass temporal response function. The TF BW was significantly wider in V1 than in V2 (Supplementary Fig. 1). We found no published data for V5.

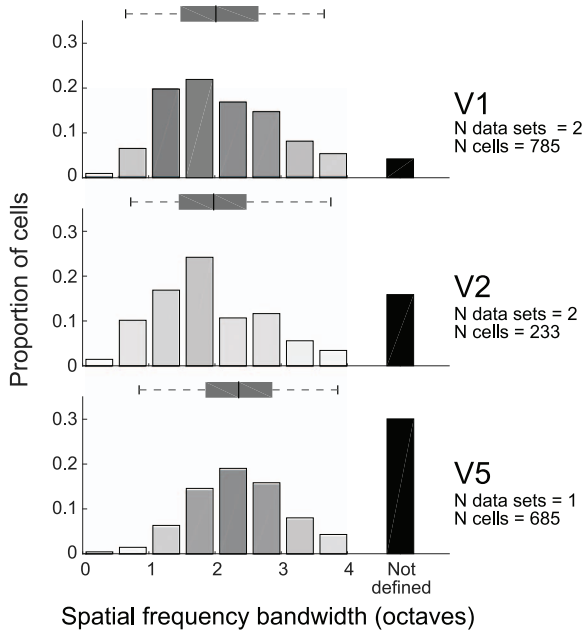

Figure 11. SF BW. Conventions are as in Figure 5. Data for V1 are from Foster et al. (1985) and Wang and Movshon (2016), for V2 from Foster et al. (1985) and Levitt et al. (1994a), and for V5 from Wang and Movshon (2016).

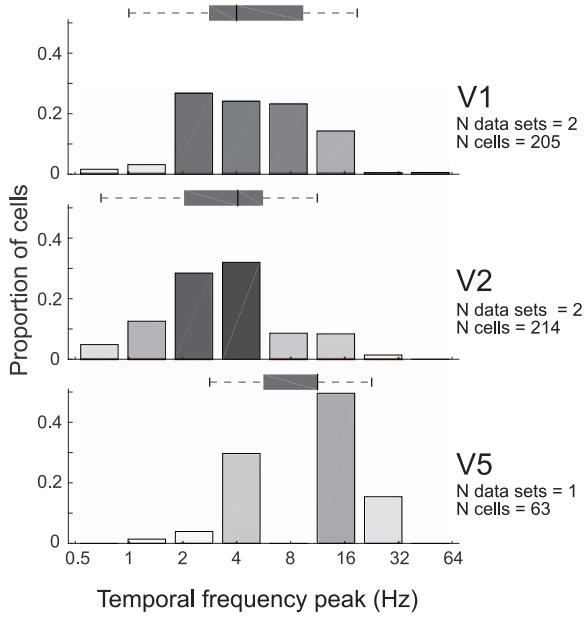

Figure 12. TF peak. Conventions are as in Figure 5. Data for V1 are from Foster et al. (1985) and Hawken et al. (1996), for V2 from Foster et al. (1985) and Levitt et al. (1994a), and for V5 from Yuan et al. (2014).

Contrast Response Function

The contrast response function is quantified using the following equation:

$$R = b + \frac{C^{\gamma}}{C^{\gamma} + C_{50}^{\gamma}}, \tag{7}$$

where R is response, b is baseline firing rate, and C is contrast (independent variable). The fitted variables are γ, the exponent,

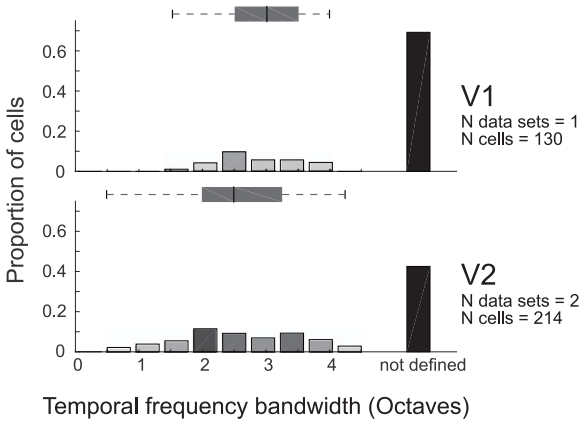

Figure 13. TF BW. Conventions are as in Figure 5. Data for V1 are from Foster et al. (1985) and for V2 from Foster et al. (1985) and Levitt et al. (1994a).

and C_{50}, the semisaturation contrast, that is, the contrast value at which the response curve reaches 50% of its maximum value.

Figure 14 shows the distributions of semisaturation contrast and contrast exponent for areas V1, V2, and V5. For each study we reviewed both parameters. The only logarithmic semisaturation contrast plot (V2) in Levitt et al. (1994a) was turned into a linear scale, for comparison.

Figure 15 visualizes the normalized contrast response functions attainable with the median exponent and semisaturation contrast for each area. Figures 14 and 15 as well as Supplementary Figure 1 demonstrate that V5 has significantly higher contrast sensitivity than the two other areas, followed by V2 and V1. This is due to the varying semisaturation contrast, whereas the median exponents are similar in the three areas.

Figure 16 shows that there is a similar distribution of maximum firing rates across the cell population in V1 and V5. The original data were binned at 10 spike/s and peaked between 10 and 20 Hz in both V1 and V5, with about 50% drop in the 0–10 Hz bin (Sclar et al. 1990).

Higher Order Feature Selectivity in V2 and V5

In addition to the low-level feature selectivity, neurons in V2 and V5 become selective to more complex RF features. These higher order features are related presumably to pattern, object, speed, and depth computations in V2 and V5.

About one-third of V2 cells are selective for complex gratings or forms (Hegdé and Van Essen 2000). These responses are dependent on anisotropic orientation sensitivity in the classical RF and its surroundings (Ito 2004; Anzai et al. 2007). Most V2 cells (63%) are sensitive to natural texture statistics, that is, in the higher order correlation of image features across spatial frequencies, orientations, and positions. This is in sharp contrast to V1, where only 15% show such selectivity (Freeman et al. 2013). Interestingly, this increased sensitivity in V2 derives from stronger surround suppression from nonnatural (gratings, noise) than from natural texture stimuli (Ziemba et al. 2018).

Stereoscopic depth perception is dependent on relative disparity between the retinal images of the two eyes. While V1, V2, and V5 all have cells which are tuned for retinal disparity, only the cells in V2 and V5 contribute to depth perception (Van Essen 1983a; DeAngelis et al. 1998; Nienborg 2006). Another depth cue, motion parallax, arises from self-motion in stationary surround-

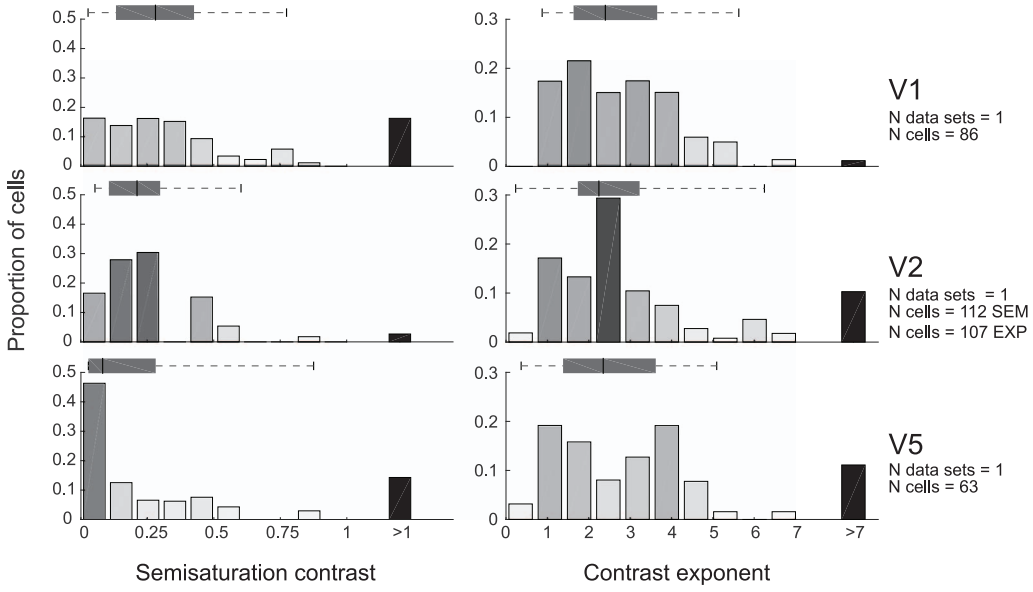

Figure 14. Semisaturation contrast and contrast exponent of the contrast response function. Conventions are as in Figure 5. Data for V1 are from Sclar et al. (1990), for V2 from Levitt et al. (1994a), and for V5 from Sclar et al. (1990).

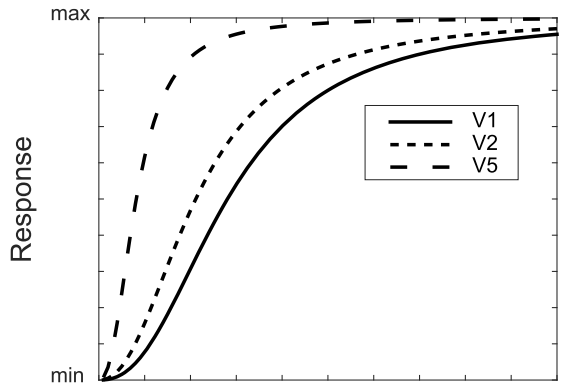

Figure 15. Contrast response function. Based on the median parameters of the data reported in Figure 14.

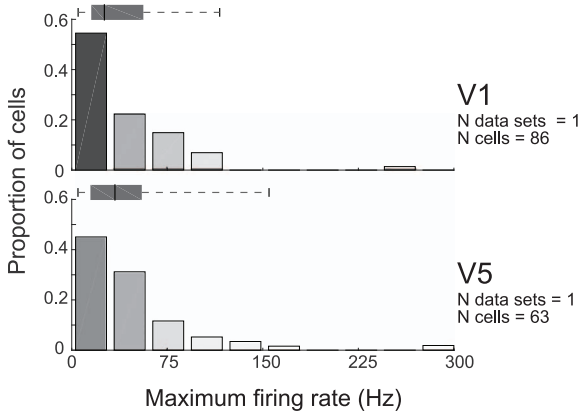

Figure 16. Maximum firing rate. Stimuli were sinusoidal gratings at 120 cd/m^2 luminance and saturating contrast; the grating orientation, SF, motion direction, and speed were optimized for each cell. Conventions are as in Figure 5. Data for V1 and V5 are from Sclar et al. (1990).

ings. Eighteen percent of V5 cells contribute significantly to behavioral judgments based on motion parallax (Kim et al. 2015).

The V2 cells assign contrast edges to particular object, or code "border ownership," more often than V1 cells (59% in V2 vs. 18% in V1; Zhou et al. 2000). This may be related to emergent segregation of objects from background in V2.

Many V5 cells become more sensitive to motion of a whole pattern than motion of the components of the pattern. Estimates for the proportion of cells which prefer pattern motion in macaque V5 range from 23 to 25%, whereas such cells are rare in V1 (Movshon et al. 1985; Wang and Movshon 2016).

Neuronal Membrane Physiology

The neuronal membrane physiology has not been systemically studied in macaque visual cortex. Some parameters have been extracted from prefrontal cortex, but given the structural differences of neurons in different areas (Elston 2003; Luebke 2017), it is unclear whether such values are relevant for the visual areas considered in this review; therefore, those data were excluded. In visual cortices, some biophysical parameters are available for V1 L3 pyramidal neurons (Table 6, Amatrudo et al. 2012; Luebke et al. 2015; Gilman et al. 2017). While all neurons have tonic regular spiking patterns, many also show phasic activity. Amatrudo et al. (2012) tuned a model neuron to the structure of a single PC providing an example table of biophysical model parameters (their Table 1).

In V1 L3 PCs, a depolarizing current step of 80 pA evokes on average (SD) a 14.9 (1.8) Hz response, and a 180 pA current step evokes a 19.6 (2.4) Hz response, clearly higher than in prefrontal cortex (Gilman et al. 2017). This is likely due to the smaller cell size, and thus membrane capacitance, in visual than prefrontal cortex, resulting in more responsive neurons to the same input current.

Table 6 Biophysical parameters for area V1 L3 pyramidal neurons

Membrane time constant (ms)	23 (19–28)
Input resistance (Mohm)	238 (205–285)
Resting membrane potential (mV)	−66 (−66.4 to −65.8)
Action potential threshold (mV)	−42 (−42.8 to −41.8)
Rheobase (pA)	82 (79–87)
sEPSC freq (Hz)	1.4 (1.2–1.5)
Rise (ms)	1.1 (1.0–1.2)
Decay (ms)	4.7 (4.2–5.4)
Amplitude (pA)	6.7 (6.4–7.3)
sIPSC freq (Hz)	0.33
Rise (ms)	2.8
Decay (ms)	7.6
Amplitude (pA)	20

Data from(Amatrudo et al. (2012), Luebke et al. (2015), and Gilman et al., (2017). sEPSC, sIPSC = spontaneous EPSP, IPSP. Mean (range) across studies.

The Need for Future Quantitative Studies

We have reviewed the literature and summarized quantitative data about the structure and function of, and interactions between, macaque visual areas V1, V2, and V5. Although available data are insufficient to support a complete quantitative microcircuit diagram, it, however, allows to construct a binary diagram, including partial data on relative connection strength, which allows to identify dominant and sparse connections in a microcircuit, helping to constrain the parameter search spaces for numerical simulations.

This review omits several areas in the occipital lobe, such as V3, V3A, V6/PO, and V4. These areas either lack a unique definition (Angelucci and Rosa 2015; Angelucci et al. 2015; Gamberini et al. 2015; Zhu and Vanduffel 2019) and clear homologues between humans and macaques (Kaas 1992; Tootell et al. 1997; Hadjikhani et al. 1998), thus precluding prospective generalization of the model system to humans, or have not been sufficiently studied to justify their inclusion into a quantitative review. The exclusion of these visual areas naturally limits the type of visual analysis that can be expected from a model and may also lead to inaccuracies in the model RFs, if the latter are shaped by FB in the real biological system.

In the early 1990s, Felleman and Van Essen (1991) provided a binary diagram of connections between macaque visual cortical areas and studied their mutual hierarchy. The CoCoMac database (Stephan et al. 2001; Kötter 2004; Bakker et al. 2012) later provided online access to interareal anatomical tract tracing data. Later these connections were studied quantitatively, revealing the dense connectome between areas (Barone et al. 2000; Markov et al. 2011; Markov et al. 2014a). The macroscopic scale is however insufficient for model simulations aiming to replicate single neuron function. Instead, we need a model at the microcircuit level.

Missing Parts for a Synthetic Blueprint

Much information is still missing in order to build a comprehensive model of the macaque visual cortex. First, we need information on which cell types contact which other cell types, making how many synapses, and the probability distribution of synapses along the dendritic tree. Unfortunately, the construction of such a detailed connectome directly from anatomical data is not technically possible, because no current method allows reading and visualizing massive anatomical volumes at synaptic resolution.

Table 7 Missing data for macaque V1, V2, and V5 needed for microcircuit reconstruction

Parameter	Missing data
Total *N* neurons by layer	V2, V5
Excitatory cell type counts by layer	PC subtypes sparse for V1, missing for V2 and V5
Inhibitory cell type counts by layer	V1, V2, V5
Interlaminar cell type-specific connectivity	Partial data for V1, sparse for V2, missing for V5
Horizontal distribution of local axons	Partial data for V1, V2, and V5
Axonal structure, incl. *N* boutons	Sparse data for V1, missing for V2 and V5
Dendritic structure	Partial data for V1, V2, missing for V5
Neural membrane electrophysiology	Sparse data for V1, missing for V2 and V5
Cell type-specific neural structural model	V1, V2, V5

PC: pyramidal cell

Fortunately, partial data samples may allow us to extract statistical rules, which could lead to the establishment of a representative connectome and synaptome of a neural system (DeFelipe 2010, 2015). Two studies, both in rat somatosensory cortex, have presented approaches to build a comprehensive model from sparse connectivity data. In the first study, Egger et al. (2014) combined experimental anatomical volumetric data, soma distributions, examples of neuron type-specific morphologies (axonal and dendritic fields), relative frequency of neuron types, and subcellular structural connectivity data between cell types. This subcellular connectivity included neuron type-specific density of postsynaptic targets, separately for the soma and apical and basal dendrites. Using these data, the software calculated dense instantiations of a microcircuit, which were available for numerical simulations (such as Landau et al. 2016). In the second study, Reimann et al. (2015) build microcircuit models based on five types of data. The first defines morphological neuron types and their local density distributions. Then, they estimate the total length of axons and the density of boutons on the axons for each type of neuron. For each connection between two neuron types, the approach requires connection probability and the mean and standard deviation of number of synapses per connection. This algorithm was later used to build a comprehensive microcircuit model of rat somatosensory cortex (Markram et al. 2015).

Table 7 lists some of the key data that are still missing for macaque. In the literature there are many anatomical tracing studies of interareal connections. Unfortunately, there are only partial data on the densities of distinct morphological neuron types in different layers for V1 and none for V2 or V5. Moreover, inhibitory cell types have not been quantified by layer, and quantitative data of dendritic length and bouton or synapse numbers on different cell types, and in different layers, are missing.

A recent cluster analysis of V1 L6 neurons provides a sense of the correlations between functional parameters (Hawken et al. 2019). The study reports six major clusters of RF properties, on the basis of simple/complex RFs (f0/f1 modulation; Skottun

et al. 1991), direction selectivity, and TF tuning. Such cluster analyses for other layers could reveal the interparameter correlations, which may significantly limit a model's parameter search space.

In addition, we are missing subcellular data on synaptic connection strengths, although it is likely that the latter are also dynamically adjusted by homeostasis (Turrigiano et al. 1998; van Rossum et al. 2000; Turrigiano 2008). For state-of-the-art Hodgkin–Huxley membrane voltage dynamics, we would, additionally, need information on the relative density of distinct ion channels. For a comprehensive multicompartmental model, the detailed dendritic morphology of distinct cell types would be required in digital format. Some data are available at http://neuromorpho.org/index.jsp mainly for V1 L6 pyramidal and spiny stellate neurons (Briggs et al. 2016) and L3 PCs (Luebke et al. 2015).

Fortunately, a complete microcircuit connectome is not necessary for simplified model simulations. Simplified models allow avoiding unnecessary complexity for some research questions and increase computational efficiency (Hokkanen et al. 2019). Figure 17 presents two levels of connection detail that can be implemented in a model. If the neural model is point-like, with fixed synaptic dynamics and firing patterns, the required level of description of the system is the identification of pre- and postsynaptic neuron types, the fraction of pre- and postsynaptic neurons contacting each other, the number of synapses per connection, and the amount of divergence and convergence in interareal connectivity (Fig. 17 [top]). However, more detailed and biologically realistic models require additional details on the morphology and firing rate statistics of the presynaptic neuron, as well as synapse location and dynamics of the postsynaptic neurons (Fig. 17 [bottom]).

Studies on anatomical tracer injections targeted to specific CO compartments of V1 or V2 have typically reported the percentages of resulting labeled neurons in each compartment. To calibrate such measures, we need data on the density of projecting fibers/mm^2 of cortical surface area for each V2 compartment. For V1, where distinct layers have unique projection patterns, such data should also indicate the amount of projecting fibers/mm^3 of cortex. Given the known layer thickness, one would thus be able to estimate the amount of projecting fibers.

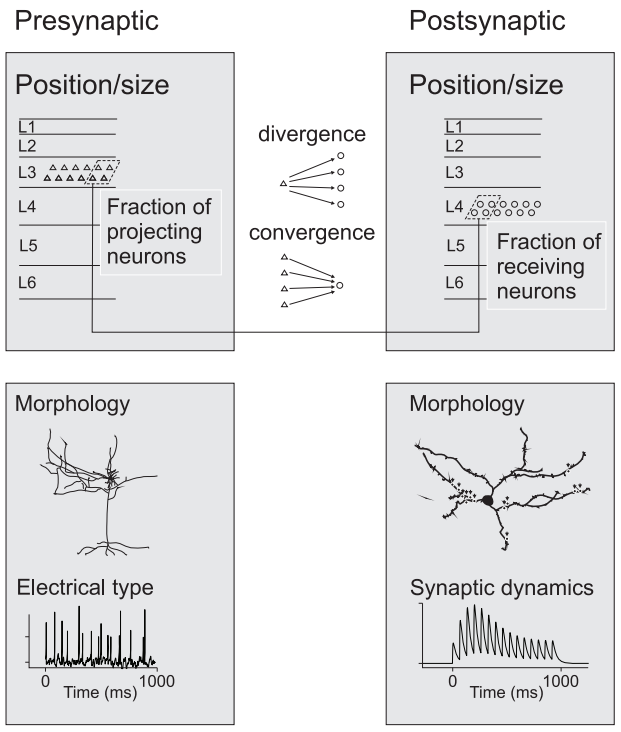

Figure 17. Describing connections between two neuron groups in silico. (A) A simple point-like phenomenological neural model with fixed synaptic dynamics only needs to incorporate data on position and population size as well as data on the divergence and convergence of connections. (B) A more comprehensive, biophysically meaningful, multicompartmental model requires, in addition, data on the cellular morphology, distribution of synapses, and electrical types of neurons and synaptic dynamics.

Filling in Missing Macaque Data for Numerical Simulations

For missing local connectivity data for macaque visual cortex, a theoretician is forced to use available data from other mammalian species, such as cat, rat, and mouse, whose local connections have been studied more extensively (Thomson and Lamy 2007; Markram et al. 2015). In addition, neural cell membrane electrophysiology has been studied more extensively in rodents (Markram et al. 1998; Thomson and Destexhe 1999; Gupta et al. 2000), and there is a clear underrepresentation of monkey data in the neuroinformatics databases, such as NeuroElectro at http://neuroelectro.org/.

Binzegger et al. (2004) collected local structural data for cat primary visual cortex and suggested a canonical microcircuit diagram based on those data and remaining assumptions. For this diagram one needs essentially three quantities: the number of each neuron type in each layer, each neuron type's average dendritic length in each layer, and the number of synapses formed by each cell type in each layer. Moreover, one needs to assume that synapses form between cell types with equal probability (Peters' rule, Braitenberg and Schuz 1998). However, many parameters remain uncertain in such a diagram, for example, how synapses are distributed onto the postsynaptic cells' dendritic trees, the short-term synaptic dynamics and potential for long-term plasticity in distinct neuron types. Moreover, potential local anatomical anisotropies, such as those of patchy local horizontal connections, remain undetermined.

Thomson (2002) provided local structural network data for rat and cat cortex, together with connection strength measured by dual or triple intracellular electrophysiological recordings in cortical slices. Most differences between species were just scale differences. Thomson (2002) reported apparent deviations from Peter's rule, particularly an asymmetry between interlaminar FF (e.g., L4 to 3 and L3 to 5) and FB projections (e.g., from L3 to L4 and from L5 to L3). The excitatory targets of FF connections were primarily the larger pyramidal neurons; the FB targets were horizontally more diffuse than the FF targets, and the FB-induced EPSPs were very small, below threshold. Moreover, FB connections were stronger onto inhibitory than onto excitatory neurons, the latter being generally very sparse. The authors suggested that this asymmetry prevents reverberating excitation within the local circuit.

Interspecies differences may unfortunately hamper the ability to supplement a monkey model with rodent data (Luebke 2017). For example, the basket cells show lower input resistance and higher firing thresholds in rat compared with monkey, causing them to have lower excitability in rats than monkeys (Povysheva et al. 2008).

Schmidt et al. (2018) estimated the quantitative anatomical connectivity of macaque visual areas by combining CoCoMac databases (Stephan et al. 2001; Bakker et al. 2012) with the fraction of supragranular presynaptic neurons in a source area (Barone et al. 2000; Markov et al. 2011; Markov et al. 2014b) and an exponential distance rule (Ercsey-Ravasz et al. 2013). As local connectivity data from macaque were largely missing, the model of Schmidt et al. (2018) used Potjans and Diesmann's (2014) local microcircuit model, which was based on data from rats and cats. While Schmidt et al. (2018) provided a full graph of connections of macaque visual cortex, as well as explicit tables of the heuristics and assumptions included in their model, our reported anatomical data are different. We provide the details of published experimental data, including the rich substructure and layer-specific connectivity. Although we provide relative rather than absolute connection strengths, and there are uncertainties about the completeness of layer-specific connectivity graphs between two areas, our work goes one step forward compared with existing interareal connectivity graphs (Felleman and Van Essen 1991; Markov et al. 2014a).

In conclusion, here, we have collated data from the literature with the goal of facilitating construction of biophysically meaningful models of macaque visual cortex and validation of such models by numerical simulation of neuronal RF properties. In the short run, it will be challenging to establish how the model structure gives rise to RF properties that resemble those measured in the real cortex, because multiple unknown factors affect RF responses. In the long run, however, a comprehensive model could nevertheless help elucidate the relation between macroscopic activation, local spiking, and signal processing in a neural population.

Supplementary Material

Supplementary material is available at *Cerebral Cortex* online.

Funding

This work was supported by Helsingin ja Uudenmaan Sairaanhoitopiiri University Hospital research funds (TYH2016257, Y1249NEUR1) to S.V.; grants from the National Institutes of Health (NIH) (R01 EY026812, R01 EY019743, BRAIN U01 NS099702), National Science Foundation (NSF) (IOS 1355075 and 1755431, EAGER 1649923), and University of Utah Neuroscience Initiative, to A.A.; grants from Research to Prevent Blindness, Inc.; and a core grant from the NIH (EY014800) to the Department of Ophthalmology, University of Utah.

Notes

We thank Vafa Andalibi for technical support and Prof. Patrizia Fattori and Dr Michela Gamberini for help with physiological data analysis.

References

Adams MM, Hof PR, Gattass R, Webster MJ, Ungerleider LG. 2000. Visual cortical projections and chemoarchitecture of macaque monkey pulvinar. *J Comp Neurol*. 419:377–393.

Ahmad A, Spear PD. 1993. Effects of aging on the size, density, and number of rhesus monkey lateral geniculate neurons. *J Comp Neurol*. 334:631–643.

Ahmed B, Cordery PM, McLelland D, Bair W, Krug K. 2012. Long-range clustered connections within extrastriate visual area V5/MT of the rhesus macaque. *Cereb Cortex*. 22: 60–73.

Albright TD. 1984. Direction and orientation selectivity of neurons in visual area MT of the macaque. *J Neurophysiol*. 52:1106–1130.

Albright TD, Desimone R. 1987. Local precision of visuotopic organization in the middle temporal area (MT) of the macaque. *Exp Brain Res*. 65:582–592.

Amatrudo JM, Weaver CM, Crimins JL, Hof PR, Rosene DL, Luebke JI. 2012. Influence of highly distinctive structural properties on the excitability of pyramidal neurons in monkey visual and prefrontal cortices. *J Neurosci*. 32:13644–13660.

Amir Y, Harel M, Malach R. 1993. Cortical hierarchy reflected in the organization of intrinsic connections in macaque monkey visual cortex. *J Comp Neurol*. 334:19–46.

Amunts K, Malikovic A, Mohlberg H, Schormann T, Zilles K. 2000. Brodmann's areas 17 and 18 brought into stereotaxic space–where and how variable. *NeuroImage*. 11:66–84.

Anderson JC, Binzegger T, Martin KAC, Rockland KS. 1998. The connection from cortical area V1 to V5: a light and electron microscopic study. *J Neurosci*. 18:10525–10540.

Anderson JC, Martin KAC. 2002. Connection from cortical area V2 to MT in macaque monkey. *J Comp Neurol*. 443:56–70.

Anderson JC, Martin KAC. 2009. The synaptic connections between cortical areas V1 and V2 in macaque monkey. *J Neurosci*. 29:11283–11293.

Anderson JS, Lampl I, Gillespie DC, Ferster D. 2000. The contribution of noise to contrast invariance of orientation tuning in cat visual cortex. *Science*. 290:1968–1972.

Angelucci A, Bijanzadeh M, Nurminen L, Federer F, Merlin S, Bressloff PC. 2017. Circuits and mechanisms for surround modulation in visual cortex. *Annu Rev Neurosci*. 40:425–451.

Angelucci A, Bressloff PC. 2006. Contribution of feedforward, lateral and feedback connections to the classical receptive field center and extra-classical receptive field surround of primate V1 neurons. *Prog Brain Res*. 154:93–120.

Angelucci A, Levitt JB, Lund JS. 2002a. Anatomical origins of the classical receptive field and modulatory surround field of single neurons in macaque visual cortical area V1. *Prog Brain Res*. 136:373–388.

Angelucci A, Levitt JB, Walton EJ, Hupe JM, Bullier J, Lund JS. 2002b. Circuits for local and global signal integration in primary visual cortex. *J Neurosci*. 22:8633–8646.

Angelucci A, Roe AW, Sereno MI. 2015. Controversial issues in visual cortex mapping: Extrastriate cortex between areas V2 and MT in human and nonhuman primates. *Vis Neurosci*. 32:e025.

Angelucci A, Rosa MGP. 2015. Resolving the organization of the third tier visual cortex in primates: a hypothesis-based approach. *Vis Neurosci*. 32:e010.

Anzai A, Peng X, Van Essen DC. 2007. Neurons in monkey visual area V2 encode combinations of orientations. *Nat Neurosci*. 10:1313–1321.

Ascoli GA, Alonso-Nanclares L, Anderson SA, Barrionuevo G, Benavides-Piccione R, Burkhalter A, Buzsáki G, Cauli B, DeFelipe J, Fairén A *et al*. 2008. Petilla terminology: nomenclature of features of GABAergic interneurons of the cerebral cortex. *Nat Rev Neurosci*. 9:557–568.

Bakker R, Wachtler T, Diesmann M. 2012. CoCoMac 2.0 and the future of tract-tracing databases. *Front Neuroinform*. 6: Article 30.

Balaram P, Kaas JH. 2014. Towards a unified scheme of cortical lamination for primary visual cortex across primates: insights from NeuN and VGLUT2 immunoreactivity. *Front Neuroanat*. 8:Article 81.

Balaram P, Young NA, Kaas JH. 2014. Histological features of layers and sublayers in cortical visual areas V1 and V2 of chimpanzees, macaque monkeys, and humans. *Eye Brain*. 6:5–18.

Baldwin MKL, Kaskan PM, Zhang B, Chino YM, Kaas JH. 2012. Cortical and subcortical connections of V1 and V2 in early postnatal macaque monkeys. *J Comp Neurol*. 520: 544–569.

Barone P, Batardiere A, Knoblauch K, Kennedy H. 2000. Laminar distribution of neurons in extrastriate areas projecting to visual areas V1 and V4 correlates with the hierarchical rank and indicates the operation of a distance rule. *J Neurosci*. 20:3263–3281.

Bartfeld E, Grinvald A. 1992. Relationships between orientation-preference pinwheels, cytochrome oxidase blobs, and ocular-dominance columns in primate striate cortex. *Proc Natl Acad Sci*. 89:11905–11909.

Beaulieu C, Kisvarday Z, Somogyi P, Cynader M, Cowey A. 1992. Quantitative distribution of gaba-immunopositive and -immunonegative neurons and synapses in the monkey striate cortex (area 17). *Cereb Cortex*. 2:295–309.

Benevento LA, Rezak M. 1976. The cortical projections of the inferior pulvinar and adjacent lateral pulvinar in the rhesus monkey (macaca mulatta): an autoradiographic study. *Brain Res*. 108:1–24.

Betizeau M, Dehay C, Kennedy H. 2013. Conformity and specificity of primate corticogenesis. In: Werner JS, Chalupa LM, editors. *The new visual neurosciences*. Cambridge, (MA): The MIT Press, pp. 1407–1422.

Bijanzadeh M, Nurminen L, Merlin S, Angelucci A. 2018. Distinct laminar processing of local and global context in primate primary visual cortex. *Neuron*. 100:259–274.

Binzegger T, Douglas RJ, Martin KA. 2004. A quantitative map of the circuit of cat primary visual cortex. *J Neurosci*. 24:8441–8453.

Blasdel GG. 1992. Differential imaging of ocular dominance and orientation selectivity in monkey striate cortex. *J Neurosci*. 12:3115–3138.

Blasdel GG, Campbell D. 2001. Functional retinotopy of monkey visual cortex. *J Neurosci*. 21:8286–8301.

Blasdel GG, Fitzpatrick D. 1984. Physiological organization of layer 4 in macaque striate cortex. *J Neurosci*. 4:880–895.

Blasdel GG, Lund JS. 1983. Termination of afferent axons in macaque striate cortex. *J Neurosci*. 3:1389–1413.

Blasdel GG, Salama G. 1986. Voltage-sensitive dyes reveal a modular organization in monkey striate cortex. *Nature*. 321:579–585.

Born RT, Bradley DC. 2005. Structure and function of visual area MT. *Annu Rev Neurosci*. 28:157–189.

Braitenberg V, Braitenberg C. 1979. Geometry of orientation columns in the visual cortex. *Biol Cybern*. 33:179–186.

Braitenberg V, Schuz A. 1998. *Cortex: statistics and geometry of neuronal connectivity*. 2nd ed. Berlin: Springer.

Briggs F, Callaway EM. 2001. Layer-specific input to distinct cell types in layer 6 of monkey primary visual cortex. *J Neurosci*. 21:3600–3608.

Briggs F, Callaway EM. 2005. Laminar patterns of local excitatory input to layer 5 neurons in macaque primary visual cortex. *Cereb Cortex*. 15:479–488.

Briggs F, Kiley CW, Callaway EM, Usrey WM. 2016. Morphological substrates for parallel streams of Corticogeniculate feedback originating in both V1 and V2 of the macaque monkey. *Neuron*. 90:388–399.

Briggs F, Usrey WM. 2009. Parallel processing in the Corticogeniculate pathway of the macaque monkey. *Neuron*. 62:135–146.

Brodmann K, Garey LJ. 2006. *Brodmann's localisation in the cerebral cortex*. Boston, MA: Springer.

Bullier J. 2001. Integrated model of visual processing. *Brain Res Brain Res Rev*. 36:96–107.

Bullier J, Girard P, Salin P-A. 1994. The role of area 17 in the transfer of visual information to extrastriate visual cortex. In: Peters A, Rockland KS, editors. *Cerebral cortex*. New York: Plenum Press, pp. 301–330.

Bullier J, Henry GH. 1980. Ordinal position and afferent input of neurons in monkey striate cortex. *J Comp Neurol*. 193: 913–935.

Bullier J, Hupe JM, James AC, Girard P. 2001. The role of feedback connections in shaping the responses of visual cortical neurons. *Prog Brain Res*. 134:193–204.

Bullier J, Kennedy H. 1983. Projection of the lateral geniculate nucleus onto cortical area V2 in the macaque monkey. *Exp Brain Res*. 53:168–172.

Bullier J, Nowak G. 1995. Parallel versus serial processing: new vistas on the distributed organization of the visual system. *Curr Biol*. 5:497–503.

Callaway EM. 1998a. Local circuits in primary visual cortex of the macaque monkey. *Annu Rev Neurosci*. 21:47–74.

Callaway EM. 1998b. Prenatal development of layer-specific local circuits in primary visual cortex of the macaque monkey. *J Neurosci*. 18:1505–1527.

Callaway EM, Wiser AK. 1996. Contributions of individual layer 2-5 spiny neurons to local circuits in macaque primary visual cortex. *Vis Neurosci*. 13:907–922.

Caputi A, Melzer S, Michael M, Monyer H. 2013. The long and short of GABAergic neurons. *Curr Opin Neurobiol*. 23:179–186.

Carlos L, Silveira L. 2003. Comparative study of primate retina. In: Kaas JH, Collins CE, editors. *The primate visual system*. London: CRC Press, pp. 29–51.

Casagrande VA, Kaas JH. 1994. The afferent, intrinsic and efferent connections of primary visual cortex in primates. In: Peters A, Rockland KS, editors. Cerebral cortex, volume 10, primary visual cortex in primates New York: Plenum Press. p. 201–259.

Casagrande VA, Royal DW. 2004. Parallel visual pathways in a dynamic system. In: Kaas JH, Collins CE, editors. *The primate visual system*. London: CRC Press, pp. 1–27.

Casagrande VA, Yazar F, Jones KD, Ding Y. 2007. The morphology of the koniocellular axon pathway in the macaque monkey. *Cereb Cortex*. 17:2334–2345.

Cavanaugh JR, Bair W, Movshon JA. 2002. Nature and interaction of signals from the receptive field center and surround in macaque V1 neurons. *J Neurophysiol*. 88:2530–2546.

Chariker XL, Shapley R, Young L. 2016. Orientation selectivity from very sparse LGN inputs in a comprehensive model of macaque V1 cortex. *J Neurosci*. 36:12368–12384.

Chen G, Lu HD, Roe AW. 2008. A map for horizontal disparity in monkey V2. *Neuron*. 58:442–450.

Chow K-L, Blum JS, Blum RA. 1950. Cell ratios in the thalamocortical visual system of Macaca mulatta. *J Comp Neurol*. 92:227–239.

Chung K, Wallace J, Kim SY, Kalyanasundaram S, Andalman AS, Davidson TJ, Mirzabekov JJ, Zalocusky KA, Mattis J, Denisin

AK *et al*. 2013. Structural and molecular interrogation of intact biological systems. *Nature*. 497:332–337.
Collins CE. 2011. Variability in neuron densities across the cortical sheet in primates. *Brain Behav Evol*. 78:37–50.
Connolly M, Van Essen D. 1984. The representation of the visual field in parvicellular and magnocellular layers of the lateral geniculate nucleus in the macaque monkey. *J Comp Neurol*. 226:544–564.
Daniel PM, Whitteridge D. 1961. The representation of the visual field on the cerebral cortex in monkeys. *J Physiol*. 159:203–221.
De Valois RL, Albrecht DG, Thorell LG. 1982a. Spatial frequency selectivity of cells in macaque visual cortex. *Vis Res*. 22:545–559.
De Valois RL, Yund EW, Hepler N. 1982b. The orientation and direction selectivity of cells in macaque visual cortex. *Vis Res*. 22:531–544.
DeAngelis GC, Cumming BG, Newsome WT. 1998. Cortical area MT and the perception of stereoscopic depth. *Nature*. 394:677–680.
DeAngelis GC, Newsome WT. 1999. Organization of disparity-selective neurons in macaque area MT. *J Neurosci*. 19: 1398–1415.
DeFelipe J. 2010. From the connectome to the synaptome: an epic love story. *Science*. 330:1198–1201.
DeFelipe J. 2011. The evolution of the brain, the human nature of cortical circuits, and intellectual creativity. *Front Neuroanat*. 5:Article 29.
DeFelipe J. 2015. The anatomical problem posed by brain complexity and size: a potential solution. *Front Neuroanat*. 9: Article 104.
DeFelipe J, González-Albo MC, Del Río MR, Elston GN. 1999. Distribution and patterns of connectivity of interneurons containing calbindin, calretinin, and parvalbumin in visual areas of the occipital and temporal lobes of the macaque monkey. *J Comp Neurol*. 412:515–526.
DeFelipe J, López-Cruz PL, Benavides-Piccione R, Bielza C, Larrañaga P, Anderson S, Burkhalter A, Cauli B, Fairén A, Feldmeyer D *et al*. 2013. New insights into the classification and nomenclature of cortical GABAergic interneurons. *Nat Rev Neurosci*. 14:202–216.
Denk W, Horstmann H. 2004. Serial block-face scanning electron microscopy to reconstruct three-dimensional tissue nanostructure. *PLoS Biol*. 2:e329.
Denk W, Strickler JH, Webb WW. 1990. Two-photon laser scanning fluorescence microscopy. *Science*. 248:73–76.
Derrington AM, Krauskopf J, Lennie P. 1984. Chromatic mechanisms in lateral geniculate nucleus of macaque. *J Physiol*. 357:241–265.
Desimone R, Ungerleider LG. 1986. Multiple visual areas in the caudal superior temporal sulcus of the macaque. *J Comp Neurol*. 248:164–189.
Douglas RJ, Martin KAC. 2004. Neuronal circuits of the Neocortex. *Annu Rev Neurosci*. 27:419–451.
Dow BM, Snyder AZ, Vautin RG, Bauer R. 1981. Magnification factor and receptive field size in Foveal striate cortex of the monkey. *Exp Brain Res*. 44:213–228.
DeYoe EA, Van Essen DC. 1985. Segregation of efferent connections and receptive field properties in visual area V2 of the macaque. *Nature*. 317:58–61.
Dubner R, Zeki SM. 1971. Response properties and receptive fields of cells in an anatomically defined region of the superior temporal sulcus in the monkey. *Brain Res*. 35:528–532.
Edwards DP, Purpura KP, Kaplan E. 1995. Contrast sensitivity and spatial frequency response of primate cortical neurons in and around the cytochrome oxidase blobs. *Vision Res*. 35: 1501–1523.
Egger R, Dercksen VJ, Udvary D, Hege H-C, Oberlaender M. 2014. Generation of dense statistical connectomes from sparse morphological data. *Front Neuroanat*. 8:Article 129.
Elston GN. 2003. Cortex, cognition and the cell: new insights into the pyramidal neuron and prefrontal function. *Cereb Cortex*. 13:1124–1138.
Elston GN, Fujita I. 2014. Pyramidal cell development: postnatal spinogenesis, dendritic growth, axon growth, and electrophysiology. *Front Neuroanat*. 8: Article 78.
Elston GN, Rosa MGP. 1997. The occipitoparietal pathway of the macaque monkey: comparison of pyramidal cell morphology in layer III of functionally related cortical visual areas. *Cereb Cortex*. 7:432–452.
Elston GN, Rosa MGP. 1998. Morphological variation of layer III pyramidal neurones in the occipitotemporal pathway of the macaque monkey visual cortex. *Cereb Cortex*. 8:278–294.
Ercsey-Ravasz M, Markov NT, Lamy C, Van Essen DC, Knoblauch K, Toroczkai Z, Kennedy H. 2013. A predictive network model of cerebral cortical connectivity based on a distance rule. *Neuron*. 80:184–197.
Erwin E, Obermayer K, Schulten K. 1995. Models of orientation and ocular dominance columns in the visual cortex: a critical comparison. *Neural Comput*. 7:425–468.
Falchier A, Clavagnier S, Barone P, Kennedy H. 2002. Anatomical evidence of multimodal integration in primate striate cortex. *J Neurosci*. 22:5749–5759.
Federer F, Merlin S, Angelucci A. 2015. *Anatomical and functional specificity of V2-to-V1 feedback circuits in the primate visual cortex*. Soc. Neurosci., Online 699.602 [abstract].
Federer F, Williams D, Ichida JM, Merlin S, Angelucci A. 2013. Two projection streams from macaque V1 to the pale cytochrome oxidase stripes of V2. *J Neurosci*. 33:11530–11539.
Felleman DJ, Lim H, Xiao Y, Wang Y, Eriksson A, Parajuli A. 2015. The representation of orientation in macaque V2: four stripes not three. *Cereb Cortex*. 25:2354–2369.
Felleman DJ, Van Essen DC. 1991. Distributed hierarchical processing in the primate cerebral cortex. *Cereb Cortex*. 1:1–47.
Fisken RA, Garey LJ, Powell TP. 1975. The intrinsic, association and commissural connections of area 17 on the visual cortex. *Philos Trans R Soc L B Biol Sci*. 272:487–536.
Fitzpatrick D, Lund JS, Schmechel DE, Towles AC. 1987. Distribution of GABAergic neurons and axon terminals in the macaque striate cortex. *J Comp Neurol*. 264:73–91.
Foster KH, Gaska JP, Nagler M, Pollen DA. 1985. Spatial and temporal frequency selectivity of neurones in visual cortical areas V1 and V2 of the macaque monkey. *J Physiol*. 365: 331–363.
Franklin MS, Kraemer GW, Shelton SE, Baker E, Kalin NH, Uno H. 2000. Gender differences in brain volume and size of corpus callosum and amygdala of rhesus monkey measured from MRI images. *Brain Res*. 852:263–267.
Freeman J, Ziemba CM, Heeger DJ, Simoncelli EP, Movshon JA. 2013. A functional and perceptual signature of the second visual area in primates. *Nat Neurosci*. 16:974–981.
Freund TF, Martin KAC, Soltesz I, Somogyi P, Whitteridge D. 1989. Arborisation pattern and postsynaptic targets of physiologically identified thalamocortical afferents in striate cortex of the macaque monkey. *J Comp Neurol*. 289:315–336.

Gamberini M, Fattori P, Galletti C. 2015. The medial parietal occipital areas in the macaque monkey. *Vis Neurosci*. 32:e013.

Garcia-Marin V, Kelly J, Hawken M. 2017. Major feedforward thalamic input into layer 4C of primary visual cortex in primate. *Cereb Cortex*. 29:134–149.

Garg AK, Li P, Rashid MS, Callaway EM. 2019. Color and orientation are jointly coded and spatially organized in primate primary visual cortex. *Science*. 364:1275–1279.

Gattas R, Sousa APB, Mishkin M, Ungerleider LG. 1997. Cortical projections of area V2 in the macaque. *Cereb Cortex*. 7: 110–129.

Gattass R, Gross CG. 1981. Visual topography of striate projection zone (MT) in posterior superior temporal sulcus of the macaque. *J Neurophysiol*. 46:621–638.

Gattass R, Gross CG, Sandell JH. 1981. Visual topography of V2 in the macaque. *J Comp Neurol*. 201:519–539.

Gattass R, Nascimento-Silva S, Soares JGM, Lima B, Jansen AK, Diogo ACM, Farias MF, Botelho MM, Mariani OS, Azzi J *et al*. 2005. Cortical visual areas in monkeys: location, topography, connections, columns, plasticity and cortical dynamics. *Philos Trans R Soc B Biol Sci*. 360:709–731.

Gattass R, Soares JGM, Desimone R, Ungerleider LG. 2014. Connectional subdivision of the claustrum: two visuotopic subdivisions in the macaque. *Front Syst Neurosci*. 8:Article 63.

Gegenfurtner KR. 2003. Cortical mechanisms of colour vision. *Nat Rev Neurosci*. 4:563–572.

Gegenfurtner KR, Kiper DC, Fenstemaker SB. 1996. Processing of color, form, and motion in macaque area V2. *Vis Neurosci*. 13:161–172.

Giannaris EL, Rosene DL. 2012. A stereological study of the numbers of neurons and glia in the primary visual cortex across the lifespan of male and female rhesus monkeys. *J Comp Neurol*. 520:3492–3508.

Gilbert CD. 1983. Microcircuitry of the visual cortex. *Annu Rev Neurosci*. 6:217–247.

Gilman JP, Medalla M, Luebke JI. 2017. Area-specific features of pyramidal neurons-a comparative study in mouse and rhesus monkey. *Cereb Cortex*. 27:2078–2094.

Girard P, Hupe JM, Bullier J. 2001. Feedforward and feedback connections between areas V1 and V2 of the monkey have similar rapid conduction velocities. *J Neurophysiol*. 85: 1328–1331.

Goris RLT, Simoncelli EP, Movshon JA. 2015. Origin and function of tuning diversity in macaque visual cortex. *Neuron*. 88:819–831.

Grinvald A, Lieke E, Frostig RD, Gilbert CD, Wiesel TN. 1986. Functional architecture of cortex revealed by optical imaging of intrinsic signals. *Nature*. 324:361–364.

Gupta A, Wang Y, Markram H. 2000. Organizing principles for a diversity of GABAergic interneurons and synapses in the Neocortex. *Science*. 287:273–278.

Gur M, Kagan I, Snodderly DM. 2005. Orientation and direction selectivity of neurons in V1 of alert monkeys: functional relationships and laminar distributions. *Cereb Cortex*. 15:1207–1221.

Gur M, Snodderly DM. 2006. High response reliability of neurons in primary visual cortex (V1) of alert, trained monkeys. *Cereb Cortex*. 16:888–895.

Gur M, Snodderly DM. 2007. Direction selectivity in V1 of alert monkeys: evidence for parallel pathways for motion processing. *J Physiol*. 585:383–400.

Gur M, Snodderly DM. 2008. Physiological differences between neurons in layer 2 and layer 3 of primary visual cortex (V1) of alert macaque monkeys. *J Physiol*. 586:2293–2306.

Hadjikhani N, Liu a K, Dale AM, Cavanagh P, Tootell RB. 1998. Retinotopy and color sensitivity in human visual cortical area V8. *Nat Neurosci*. 1:235–241.

Harris KD, Shepherd GMG. 2015. The neocortical circuit: themes and variations. *Nat Neurosci*. 18:170–181.

Hassler R. 1966. Comparative anatomy of the central visual system in dayand night-active primates. In: Hassler R, Stephan H, editors. *Evolution of the forebrain*. Stuttgart: Thieme, pp. 419–434.

Hawken MJ, Shapley RM, Disney AA, Garcia-Marin V, Henrie JA, Henry CA, Johnson EM, Joshi S, Kelly JG, Ringach DL *et al*. 2019. Functional clusters of neurons in layer 6 of macaque V1. *bioRxiv*. doi: 10.1101/685990.

Hawken MJ, Shapley RM, Grosof DH. 1996. Temporal-frequency selectivity in monkey visual cortex. *Vis Neurosci*. 13:477–492.

Hegdé J, Van Essen DC. 2000. Selectivity for complex shapes in primate visual area V2. *J Neurosci*. 20:RC61.

Hegdé J, Van Essen DC. 2003. Strategies of shape representation in macaque visual area V2. *Vis Neurosci*. 20:313–328.

Heider B, Meskenaite V, Peterhans E. 2000. Anatomy and physiology of a neural mechanism defining depth order and contrast polarity at illusory contours. *Eur J Neurosci*. 12:4117–4130.

Hendrickson AE, Wilson JR, Ogren MP. 1978. The neuroanatomical organization of pathways between the dorsal lateral geniculate nucleus and visual cortex in old world and new world primates. *J Comp Neurol*. 182:123–136.

Hendry SH, Reid RC. 2000. The koniocellular pathway in primate vision. *Annu Rev Neurosci*. 23:127–153.

Hendry SH, Schwark HD, Jones EG, Yan J. 1987. Numbers and proportions of GABA-immunoreactive neurons in different areas of monkey cerebral cortex. *J Neurosci*. 7:1503–1519.

Hendry SHC, Yoshioka T. 1994. A neurochemically distinct third channel in the macaque dorsal lateral geniculate nucleus. *Science*. 264:575–577.

Hofman MA. 1989. On the evolution and geometry of the brain in mammals. *Prog Neurobiol*. 32:137–158.

Hokkanen H, Andalibi V, Vanni S. 2019. Controlling complexity of cerebral cortex simulations-II: streamlined microcircuits. *Neural Comput*. 31:1066–1084.

Horton JC. 1984. Cytochrome oxidase patches: a new cytoarchitectonic feature of monkey visual cortex. *Philos Trans R Soc Lond Ser B Biol Sci*. 304:199–253.

Horton JC, Hocking DR. 1996. Intrinsic variability of ocular dominance column periodicity in normal macaque monkeys. *J Neurosci*. 16:7228–7339.

Horton JC, Hubel DH. 1981. Regular patchy distribution of cytochrome oxidase staining in primary visual cortex of macaque monkey. *Nature*. 292:762–764.

Hu J, Ma H, Zhu S, Li P, Xu H, Fang Y, Chen M, Han C, Fang C, Cai X *et al*. 2018. Visual motion processing in macaque V2. *Cell Rep*. 25:157–167.e5.

Hubel D, Wiesel T. 1968. Receptive fields and functional architecture of monkey striate cortex. *J Physiol*. 195:215–243.

Hubel DH, Freeman DC. 1977. Projection into the visual field of ocular dominance columns in macaque monkey. *Brain Res*. 122:336–343.

Hubel DH, Wiesel TN. 1972. Laminar and columnar distribution of geniculo-cortical fibers in the macaque monkey. *J Comp Neurol*. 146:421–450.

Hubel DH, Wiesel TN. 1974a. Sequence regularity and geometry of orientation columns in the monkey striate cortex. *J Comp Neurol*. 158:267–294.

Hubel DH, Wiesel TN. 1974b. Uniformity of monkey striate cortex: a parallel relationship between field size, scatter, and magnification factor. *J Comp Neurol*. 158:295–305.

Hubel DH, Wiesel TN. 1977. Ferrier lecture. Functional architecture of macaque monkey visual cortex. *Proc R Soc Lond Ser B Biol Sci*. 198:1–59.

Hubener M, Bolz J. 1992. Relationships between dendritic morphology and cytochrome-oxidase compartments in monkey striate cortex. *J Comp Neurol*. 324:67–80.

Hunter JN, Born RT. 2011. Stimulus-dependent modulation of suppressive influences in MT. *J Neurosci*. 31: 678–686.

Hupé J-MM, James AC, Girard P, Bullier J. 2001. Response modulations by static texture surround in area V1 of the macaque monkey do not depend on feedback connections from V2. *J Neurophysiol*. 85:146–163.

Hupé JM, James AC, Payne BR, Lomber SG, Girard P, Bullier J. 1998. Cortical feedback improves discrimination between figure and background by V1, V2 and V3 neurons. *Nature*. 394:784–787.

Ito M. 2004. Representation of angles embedded within contour stimuli in area V2 of macaque monkeys. *J Neurosci*. 24:3313–3324.

Jerison HJ. 1955. Brain to body ratios and the evolution of intelligence. *Science*. 121:447–449.

Jia H, Rochefort NL, Chen X, Konnerth A. 2010. Dendritic organization of sensory input to cortical neurons in vivo. *Nature*. 464:1307–1312.

Jones EG. 1993. Gabaergic neurons and their role in cortical plasticity in primates. *Cereb Cortex*. 3:361–372.

Jones EG, Dell'Anna ME, Molinari M, Rausell E, Hashikawa T. 1995. Subdivisions of macaque monkey auditory cortex revealed by calcium-binding protein immunoreactivity. *J Comp Neurol*. 362:153–170.

Kaas JH. 1992. Do humans see what monkeys see? *Trends Neurosci*. 15:1–3.

Kaas JH. 1995. The evolution of isocortex. *Brain Behav Evol*. 46:187–196.

Kaas JH. 2003. Early visual areas: V1, V2, V3, DM, DL, and MT. In: Kaas JH, Collins CE, editors. *The primate visual system*. London: CRC Press, pp. 139–159.

Kaas JH. 2005. The evolution of visual cortex in primates. In: Kremers J, editor. *The primate visual system*. John Wiley & Sons Ltd, pp. 267–284.

Kaplan E. 2003. The M, P, and K Pathways of the Primate Visual System. In: Chalupa L, Werner J, editors. *The Visual Neurosciences*. Cambridge, MA: The MIT Press, pp. 481–493.

Katz LC, Gilbert CD, Wiesel TN. 1989. Local circuits and ocular dominance columns in monkey striate cortex. *J Neurosci*. 9:1389–1399.

Kelly JG, Hawken MJ. 2017. Quantification of neuronal density across cortical depth using automated 3D analysis of confocal image stacks. *Brain Struct Funct*. 222: 3333–3353.

Kennedy H, Bullier J. 1985. A double-labeling investigation of the afferent connectivity to cortical areas V1 and V2 of the macaque monkey. *J Neurosci*. 5:2815–2830.

Kim HR, Angelaki DE, DeAngelis GC. 2015. A functional link between MT neurons and depth perception based on motion parallax. *J Neurosci*. 35:2766–2777.

Kisvarday ZF, Cowey A, Smith a D, Somogyi P. 1989. Interlaminar and lateral excitatory amino acid connections in the striate cortex of monkey. *J Neurosci*. 9:667–682.

Kötter R. 2004. Online retrieval, processing, and visualization of primate connectivity data from the CoCoMac database. *Neuroinformatics*. 2:127–144.

Kravitz DJ, Saleem KS, Baker CI, Mishkin M. 2011. A new neural framework for visuospatial processing. *Nat Rev Neurosci*. 12:217–230.

Kravitz DJ, Saleem KS, Baker CI, Ungerleider LG, Mishkin M. 2013. The ventral visual pathway: an expanded neural framework for the processing of object quality. *Trends Cogn Sci*. 17:26–49.

Kritzer MF, Cowey A, Somogyi P. 1992. Patterns of inter- and intralaminar GABAergic connections distinguish striate (V1) and extrastriate (V2, V4) visual cortices and their functionally specialized subdivisions in the rhesus monkey. *J Neurosci*. 12:4545–4564.

Krzywinski M, Schein J, Birol I, Connors J, Gascoyne R, Horsman D, Jones SJ, Marra MA. 2009. Circos: an information aesthetic for comparative genomics. *Genome Res*. 19: 1639–1645.

Lagae L, Raiguel S, Orban GA. 1993. Speed and direction selectivity of macaque middle temporal neurons. *J Neurophysiol*. 69:19–39.

Landau ID, Egger R, Dercksen VJ, Oberlaender M, Sompolinsky H. 2016. The impact of structural heterogeneity on excitation-inhibition balance in cortical networks. *Neuron*. 92:1106–1121.

Landisman CEC, Ts'o DY. 2002. Color processing in macaque striate cortex: relationships to ocular dominance, cytochrome oxidase, and orientation. *J Neurophysiol*. 87:3126–3137.

Large I, Bridge H, Ahmed B, Clare S, Kolasinski J, Lam WW, Miller KL, Dyrby TB, Parker AJ, Smith JET *et al*. 2016. Individual differences in the alignment of structural and functional markers of the V5/MT complex in primates. *Cereb Cortex*. 26:3928–3944.

Larkman AU. 1991. Dendritic morphology of pyramidal neurones of the visual cortex of the rat: I. branching patterns. *J Comp Neurol*. 306:307–319.

Larkum M. 2013. A cellular mechanism for cortical associations: an organizing principle for the cerebral cortex. *Trends Neurosci*. 36:141–151.

Larkum ME, Senn W, Lüscher HR. 2004. Top-down dendritic input increases the gain of layer 5 pyramidal neurons. *Cereb Cortex*. 14:1059–1070.

le Gros Clark WE. 1941. The laminar organization and cell content of the lateral geniculate body in the monkey. *J Anat*. 75:419–433.

Lee SH, Hjerling-Leffler J, Zagha E, Fishell G, Rudy B. 2010. The largest group of superficial neocortical GABAergic interneurons expresses ionotropic serotonin receptors. *J Neurosci*. 30:16796–16808.

Lee WCA, Bonin V, Reed M, Graham BJ, Hood G, Glattfelder K, Reid RC. 2016. Anatomy and function of an excitatory network in the visual cortex. *Nature*. 532:370–374.

Lennie P, Movshon JA. 2005. Coding of color and form in the geniculostriate visual pathway (invited review). *J Opt Soc Am A Opt Image Sci Vis*. 22:2013–2033.

LeVay S, Hubel D, Wiesel T. 1975. The pattern of ocular dominance columns in macaque visual cortex revealed by a reduced silver stain. *J Comp Neurol*. 159:559–576.

Levitt JB, Kiper DC, Movshon JA. 1994a. Receptive fields and functional architecture of macaque V2. *J Neurophysiol*. 71:2517–2542.

Levitt JB, Lund JS, Yoshioka T. 1996. Anatomical substrates for early stages in cortical processing of visual information in the macaque monkey. *Behav Brain Res*. 76:5–19.

Levitt JB, Yoshioka T, Lund JS. 1994b. Intrinsic cortical connections in macaque visual area V2: evidence for interaction between different functional streams. *J Comp Neurol*. 342:551–570.

Li H, Fukuda M, Tanifuji M, Rockland KS. 2003. Intrinsic collaterals of layer 6 Meynert cells and functional columns in primate V1. *Neuroscience*. 120:1061–1069.

Li WH. 2015. A fast and flexible computer vision system for implanted visual prostheses. *Lect Notes Comput Sci*. 8927: 686–701.

Livingstone M, Hubel D. 1988a. Segregation of form, color, movement and depth: anatomy, physiology and perception. *Science*. 240:740–749.

Livingstone MS, Hubel DH. 1984a. Anatomy and physiology of a color system in the primate visual cortex. *J Neurosci*. 4:309–356.

Livingstone MS, Hubel DH. 1984b. Specificity of intrinsic connections in primate primary visual cortex. *J Neurosci*. 4: 2830–2835.

Livingstone MS, Hubel DH. 1988b. Do the relative mapping densities of the magno- and parvocellular systems vary with eccentricity? *J Neurosci*. 8:4334–4339.

Lu HD, Chen G, Tanigawa H, Roe AW. 2010. A motion direction map in macaque V2. *Neuron*. 68:1002–1013.

Lu HD, Roe AW. 2007. Optical imaging of contrast response in macaque monkey V1 and V2. *Cereb Cortex*. 17:2675–2695.

Lu HD, Roe AW. 2008. Functional organization of color domains in V1 and V2 of macaque monkey revealed by optical imaging. *Cereb Cortex*. 18:516–533.

Luebke JI. 2017. Pyramidal neurons are not generalizable building blocks of cortical networks. *Front Neuroanat*. 11:Article 11.

Luebke JI, Medalla M, Amatrudo JM, Weaver CM, Crimins JL, Hunt B, Hof PR, Peters A. 2015. Age-related changes to layer 3 pyramidal cells in the rhesus monkey visual cortex. *Cereb Cortex*. 25:1454–1468.

Lund JS. 1973. Organization of neurons in the visual cortex, area 17, of the monkey (Macaca mulatta). *J Comp Neurol*. 147:455–495.

Lund JS. 1987. Local circuit neurons of macaque monkey striate cortex: I. neurons of laminae 4C and 5A. *J Comp Neurol*. 257:60–92.

Lund JS. 1988. Anatomical Organization of Macaque Monkey Striate Visual Cortex. *Annu Rev Neurosci*. 11:253–288.

Lund JS, Angelucci A, Bressloff PC. 2003. Anatomical substrates for functional columns in macaque monkey primary visual cortex. *Cereb Cortex*. 13:15–24.

Lund JS, Boothe RG. 1975. Lnterlaminar connections and pyramidal neuron organisation in the visual cortex, area 17, of the macaque monkey. *J Comp Neurol*. 159:305–334.

Lund JS, Griffiths S, Rumberger A, Levitt JB. 2001. Inhibitory synapse cover on the Somata of excitatory neurons in macaque monkey visual cortex. *Cereb Cortex*. 11:783–795.

Lund JS, Hawken MJ, Parker AJ. 1988. Local circuit neurons of macaque monkey striate cortex: II. Neurons of laminae 5B and 6. *J Comp Neurol*. 276:1–29.

Lund JS, Hendrickson AE, Ogren MP, Tobin EA. 1981. Anatomical organization of primate visual cortex area VII. *J Comp Neurol*. 202:19–45.

Lund JS, Lund RD, Hendrickson AE, Bunt AH, Fuchs AF. 1975. The origin of efferent pathways from the primary visual cortex, area 17, of the macaque monkey as shown by retrograde transport of horseradish peroxidase. *J Comp Neurol*. 164:287–303.

Lund JS, Wu CQ. 1997. Local circuit neurons of macaque monkey striate cortex: IV. Neurons of laminae 1-3a. *J Comp Neurol*. 384:109–126.

Lund JS, Yoshioka T. 1991. Local circuit neurons of macaque monkey striate cortex: III. Neurons of laminae 4B, 4A, and 3B. *J Comp Neurol*. 311:234–258.

Lund JS, Yoshioka T, Levitt JB. 1993. Comparison of intrinsic connectivity in different areas of macaque monkey cerebral cortex. *Cereb Cortex*. 3:148–162.

Lund JS, Yoshioka T, Levitt JB. 1994. Substrates for interlaminar connections in area V1 of macaque monkey cerebral cortex. In: Peters A, Rockland KS, editors. *Cerebral cortex, volume 10, primary visual cortex in primates*. New York: Plenum Press, pp. 37–60.

Luo L, Callaway EM, Svoboda K. 2008. Genetic dissection of neural circuits. *Neuron*. 57:634–660.

Mainen Z, Sejnowski T. 1995. Reliability of spike timing in neocortical neurons. *Science*. 268:1503–1506.

Malach R, Amir Y, Harel M, Grinvald A. 1993. Relationship between intrinsic connections and functional architecture revealed by optical imaging and in vivo targeted biocytin injections in primate striate cortex. *Proc Natl Acad Sci*. 90:10469–10473.

Malpeli JG, Lee D, Baker FH. 1996. Laminar and retinotopic organization of the macaque lateral geniculate nucleus: magnocellular and parvocellular magnification functions. *J Comp Neurol*. 375:363–377.

Mansfield RJW. 1973. Latency functions in human vision. *Vis Res*. 13:2219–2234.

Marino L. 1998. A comparison of encephalization between odontocete cetaceans and anthropoid primates. *Brain Behav Evol*. 51:230–238.

Markov NT, Ercsey-Ravasz M, Ribeiro Gomes AR, Lamy C, Magrou L, Vezoli J, Misery P, Falchier A, Quilodran R, Gariel MA *et al*. 2014a. A weighted and directed interareal connectivity matrix for macaque cerebral cortex. *Cereb Cortex*. 24:17–36.

Markov NT, Ercsey-Ravasz M, Van Essen DC, Knoblauch K, Toroczkai Z, Kennedy H. 2013. Cortical high-density counterstream architectures. *Science*. 342:1238406.

Markov NT, Misery P, Falchier A, Lamy C, Vezoli J, Quilodran R, Gariel MA, Giroud P, Ercsey-Ravasz M, Pilaz LJ *et al*. 2011. Weight consistency specifies regularities of macaque cortical networks. *Cereb Cortex*. 21:1254–1272.

Markov NT, Vezoli J, Chameau P, Falchier A, Quilodran R, Huissoud C, Lamy C, Misery P, Giroud P, Ullman S *et al*. 2014b. Anatomy of hierarchy: feedforward and feedback pathways in macaque visual cortex. *J Comp Neurol*. 522:225–259.

Markram H, Muller E, Ramaswamy S, Reimann MW, Abdellah M, Sanchez CA, Ailamaki A, Alonso-Nanclares L, Antille N, Arsever S *et al*. 2015. Reconstruction and simulation of neocortical microcircuitry. *Cell*. 163:456–492.

Markram H, Toledo-Rodriguez M, Wang Y, Gupta A, Silberberg G, Wu C. 2004. Interneurons of the neocortical inhibitory system. *Nat Rev Neurosci*. 5:793–807.

Markram H, Wang Y, Tsodyks M. 1998. Differential signaling via the same axon of neocortical pyramidal neurons. *Proc Natl Acad Sci U S A*. 95:5323–5328.

Mates SL, Lund JS. 1983. Neuronal composition and development in lamina 4C of monkey striate cortex. *J Comp Neurol*. 221:60–90.

Maunsell JH, Gibson JR. 1992. Visual response latencies in striate cortex of the macaque monkey. *J Neurophysiol*. 68: 1332–1344.

Maunsell JH, Van Essen DC. 1983a. Functional properties of neurons in middle temporal visual area of the macaque monkey. II. Binocular interactions and sensitivity to binocular disparity. *J Neurophysiol*. 49:1148–1167.

Maunsell JHR, van Essen DC. 1987. Topographic organization of the middle temporal visual area in the macaque monkey: representational biases and the relationship to callosal connections and myeloarchitectonic boundaries. *J Comp Neurol*. 266:535–555.

Maunsell JHR, Van Essen DC. 1983b. The connections of the middle temporal visual area (MT) and their relationship to a cortical hierarchy in the macaque monkey. *J Neurosci*. 3:2563–2586.

Maunsell JHR, Van Essen DC. 1983c. Functional properties of neurons in middle temporal visual area of the macaque monkey. I. Selectivity for stimulus direction, speed, and orientation. *J Neurophysiol*. 49:1127–1147.

McFarland JM, Cumming BG, Butts DA. 2016. Variability and correlations in primary visual cortical neurons driven by fixational eye movements. *J Neurosci*. 36:6225–6241.

McGuire BA, Gilbert CD, Rivlin PK, Wiesel TN. 1991. Targets of horizontal connections in macaque primary visual cortex. *J Comp Neurol*. 305:370–392.

Medalla M, Luebke JI. 2015. Diversity of Glutamatergic synaptic strength in lateral prefrontal versus primary visual cortices in the rhesus monkey. *J Neurosci*. 35:112–127.

Mejias JF, Murray JD, Kennedy H, Wang X-J. 2016. Feedforward and feedback frequency-dependent interactions in a large-scale laminar network of the primate cortex. *Sci Adv*. 2:e1601335.

Merigan WH, Maunsell JHR. 1993. How parallel are the primate visual pathways? *Annu Rev Neurosci*. 16:369–402.

Merlin S, Ichida J, Federer F, Schiessl I, Angelucci A. 2012. Systematic relationship between cytochrome oxidase (CO) blobs, orientation singularities and dendritic spines in macaque V1. *Soc Neurosci*. Online 568.02 [abstarct].

Miller KD, Troyer TW. 2002. Neural noise can explain expansive, power-law nonlinearities in neural response functions. *J Neurophysiol*. 87:653–659.

Montero VM, Zempel J. 1986. The proportion and size of GABA-immunoreactive neurons in the magnocellular and parvocellular layers of the lateral geniculate nucleus of the rhesus monkey. *Exp Brain Res*. 62:215–223.

Mortazavi F, Stankiewicz A, Zhdanova I. 2019. Looking through brains with fast passive CLARITY: Zebrafish, rodents, nonhuman primates and humans. *Bio-protocol*. 9:e3321.

Movshon JA, Adelson EH, Gizzi MS, Newsome WT. 1985. The analysis of moving visual patterns. In: Chagas C, Gattas R, Gross CG, editors. *Pattern recognition mechanisms*. Rome: Vatican Press, pp. 119–151.

Movshon JA, Newsome WT. 1996. Visual response properties of striate cortical neurons projecting to area MT in macaque monkeys. *J Neurosci*. 16:7733–7741.

Munk MH, Nowak LG, Girard P, Chounlamountri N, Bullier J. 1995. Visual latencies in cytochrome oxidase bands of macaque area V2. *Proc Natl Acad Sci*. 92:988–992.

Nassi JJ, Callaway EM. 2006. Multiple circuits relaying primate parallel visual pathways to the middle temporal area. *J Neurosci*. 26:12789–12798.

Nassi JJ, Callaway EM. 2007. Specialized circuits from primary visual cortex to V2 and area MT. *Neuron*. 55:799–808.

Nassi JJ, Callaway EM. 2009. Parallel processing strategies of the primate visual system. *Nat Rev Neurosci*. 10:360–372.

Nassi JJ, Lomber SG, Born RT. 2013. Corticocortical feedback contributes to surround suppression in V1 of the alert primate. *J Neurosci*. 33:8504–8517.

Nauhaus I, Benucci A, Carandini M, Ringach DL. 2008. Neuronal selectivity and local map structure in visual cortex. *Neuron*. 57:673–679.

Nauhaus I, Nielsen KJ, Disney AA, Callaway EM. 2012. Orthogonal micro-organization of orientation and spatial frequency in primate primary visual cortex. *Nat Neurosci*. 15:1683–1690.

Nealey TA, Maunsell JH. 1994. Magnocellular and parvocellular contributions to the responses of neurons in macaque striate cortex. *J Neurosci*. 14:2069–2079.

Nhan HL, Callaway EM. 2012. Morphology of superior colliculus- and middle temporal area-projecting neurons in primate primary visual cortex. *J Comp Neurol*. 520:52–80.

Nienborg H. 2006. Macaque V2 neurons, but not V1 neurons, show choice-related activity. *J Neurosci*. 26:9567–9578.

Nieuwenhuys R. 1994. The neocortex. An overview of its evolutionary development, structural organization and synaptology. *Anat Embryol*. 190:307–337.

Nowak LG, Bullier J. 1997. The timing of information transfer in the visual system. In: Rockland KS, Kaas JH, Peters A, editors. *Cerebral cortex*. London: Plenum Press, pp. 205–241.

Nowak LG, Munk MH, Girard P, Bullier J. 1995. Visual latencies in areas V1 and V2 of the macaque monkey. *Vis Neurosci*. 12:371–384.

Nurminen L, Merlin S, Bijanzadeh M, Federer F, Angelucci A. 2018. Top-down feedback controls spatial summation and response amplitude in primate visual cortex. *Nat Commun*. 9:2281.

O'Kusky J, Colonnier M. 1982a. Postnatal changes in the number of neurons and synapses in the visual cortex (area 17) of the macaque monkey: a stereological analysis in normal and monocularly deprived animals. *J Comp Neurol*. 210: 291–306.

O'Kusky J, Colonnier M. 1982b. A laminar analysis of the number of neurons, glia, and synapses in the visual cortex (area 17) of adult macaque monkeys. *J Comp Neurol*. 210:278–290.

Obermayer K, Blasdel GG. 1993. Geometry of orientation and ocular dominance columns in monkey striate cortex. *J Neurosci*. 13:4114–4129.

Oga T, Elston GN, Fujita I. 2017. Postnatal dendritic growth and spinogenesis of layer-V pyramidal cells differ between visual, inferotemporal, and prefrontal cortex of the macaque monkey. *Front Neurosci*. 11:Article 118.

Oga T, Okamoto T, Fujita I. 2016. Basal dendrites of layer-III pyramidal neurons do not scale with changes in cortical magnification factor in macaque primary visual cortex. *Front Neural Circuits*. 10:Article 74.

Olavarria JF, Van Essen DC. 1997. The global pattern of cytochrome oxidase stripes in visual area V2 of the macaque monkey. *Cereb Cortex*. 7:395–404.

Pack CC, Hunter NJ, Born RT. 2005. Contrast dependence of suppressive influences in cortical area MT of alert macaque. *J Neurophysiol*. 93:1809–1815.

Palmer CR, Chen Y, Seidemann E. 2012. Uniform spatial spread of population activity in primate parafoveal V1. *J Neurophysiol*. 107:1857–1867.

Perkel DJ, Bullier J, Kennedy H. 1986. Topography of the afferent connectivity of area 17 in the macaque monkey: a double-labelling study. *J Comp Neurol*. 253:374–402.

Perrone JA, Thiele A. 2001. Speed skills: measuring the visual speed analyzing properties of primate MT neurons. *Nat Neurosci*. 4:526–532.

Peterhans E, von der Heydt R. 1993. Functional organization of area V2 in the alert macaque. *Eur J Neurosci*. 5:509–524.

Peters A, Payne BR, Budd J. 1994. A numerical analysis of the geniculocortical input to striate cortex in the monkey. *Cereb Cortex*. 4:215–229.

Peters A, Sethares C. 1991a. Layer IVA of rhesus monkey primary visual cortex. *Cereb Cortex*. 1:445–462.

Peters A, Sethares C. 1991b. Organization of pyramidal neurons in area 17 of monkey visual cortex. *J Comp Neurol*. 306:1–23.

Petruzza S, Venkat A, Gyulassy A, Scorzelli G, Federer F, Angelucci A, Pascucci V, Bremer PT. 2017. ISAVS: interactive scalable analysis and visualization system. In: SIGGRAPH Asia.

Petruzza S, Venkat A, Gyulassy A, Scorzelli G, Federer F, Angelucci A, Pascucci V, Bremer PT. 2018. Scaling big data neuroscience: from interactive analytics to HPC platforms. *Adv Parallel Comput*. 33:53–68.

Polimeni JR, Balasubramanian M, Schwartz EL. 2006. Multi-area visuotopic map complexes in macaque striate and extra-striate cortex. *Vis Res*. 46:3336–3359.

Polimeni JR, Granquist-Fraser D, Wood RJ, Schwartz EL. 2005. Physical limits to spatial resolution of optical recording: clarifying the spatial structure of cortical hypercolumns. *Proc Natl Acad Sci U S A*. 102:4158–4163.

Potjans TC, Diesmann M. 2014. The cell-type specific cortical microcircuit: relating structure and activity in a full-scale spiking network model. *Cereb Cortex*. 24:785–806.

Povysheva NV, Zaitsev AV, Rotaru DC, Gonzalez-Burgos G, Lewis DA, Krimer LS. 2008. Parvalbumin-positive basket interneurons in monkey and rat prefrontal cortex. *J Neurophysiol*. 100:2348–2360.

Preuss TM. 2004. Specializations of the human visual system: the monkey model meets the human reality. In: Kaas JH, Collins CE, editors. *The primate visual system*. London: CRC Press, pp. 231–259.

Raiguel SE, Lagae L, Gulyas B, Orban GA. 1989. Response latencies of visual cells in macaque areas V1, V2 and V5. *Brain Res*. 493:155–159.

Rall W. 1962. Theory of physiological properties of dendrites. *Ann N Y Acad Sci*. 96:1071–1092.

Ramsden BM, Hung CP, Roe AW. 2014. Orientation domain diversity in macaque area V2. *Eye Brain*. 6:97–112.

Rasch MJ, Schuch K, Logothetis NK, Maass W. 2011. Statistical comparison of spike responses to natural stimuli in monkey area V1 with simulated responses of a detailed laminar network model for a patch of V1. *J Neurophysiol*. 105:757–778.

Reimann MW, King JG, Muller EB, Ramaswamy S, Markram H. 2015. An algorithm to predict the connectome of neural microcircuits. *Front Comput Neurosci*. 9:Article 120.

Ringach DL, Shapley RM, Hawken MJ. 2002. Orientation selectivity in macaque V1: diversity and laminar dependence. *J Neurosci*. 22:5639–5651.

Rockland KS. 1985. A reticular pattern of intrinsic connections in primate area V2 (area 18). *J Comp Neurol*. 235:467–478.

Rockland KS. 1989. Bistratified distribution of terminal Arbors of individual axons projecting from area V1 to middle temporal area (MT) in the macaque monkey. *Vis Neurosci*. 3:155–170.

Rockland KS. 1994. The organization of feedback connections from area V2 (18) to V1 (17). In: Peters A, Rockland KS, editors. *Cerebral cortex, volume 10, primary visual cortex in primates*. New York: Plenum Press, pp. 261–299.

Rockland KS. 1995. Morphology of individual axons projecting from area V2 to MT in the macaque. *J Comp Neurol*. 355:15–26.

Rockland KS. 1997. Elements of cortical architecture: hierarchy revisited. In: Rockland KS, Kaas JH, Peters A, editors. *Cerebral cortex volume 12: extrastriate cortex in primates*. London: Plenum Press, pp. 243–293.

Rockland KS, Lund JS. 1983. Intrinsic laminar lattice connections in primate visual cortex. *J Comp Neurol*. 216:303–318.

Rockland KS, Ojima H. 2003. Multisensory convergence in calcarine visual areas in macaque monkey. *Int J Psychophysiol*. 50:19–26.

Rockland KS, Pandya DN. 1979. Laminar origins and terminations of cortical connections of the occipital lobe in the rhesus monkey. *Brain Res*. 179:3–20.

Rockland KS, Virga A. 1989. Terminal arbors of individual "feedback" axons projecting from area V2 to V1 in the macaque monkey: a study using immunohistochemistry of anterogradely transported Phaseolus vulgaris-leucoagglutinin. *J Comp Neurol*. 285:54–72.

Rockland KS, Virga A. 1990. Organization of Individual Cortical Axons Projecting from Area VI (area 17) to V2 (area 18) in the macaque monkey. *Vis Neurosci*. 4:11–28.

Roe AW. 2004. Modular complexity of area V2 in the macaque monkey. In: Kaas JH, Collins CE, editors. *The primate visual system*. London: CRC Press, pp. 109–138.

Roe AW, Lu HD, Hung CP. 2005. Cortical processing of a brightness illusion. *Proc Natl Acad Sci*. 102:3869–3874.

Roe W, Ts'o DY. 1995. Visual topography in primate V2: multiple representation across functional stripes. *J Neurosci*. 15:3689–3715.

Rosa MGP, Tweedale R. 2005. Brain maps, great and small: lessons from comparative studies of primate visual cortical organization. *Philos Trans R Soc B Biol Sci*. 360:665–691.

Rudy B, Fishell G, Lee S, Hjerling-Leffler J. 2011. Three groups of interneurons account for nearly 100% of neocortical GABAergic neurons. *Dev Neurobiol*. 71:45–61.

Saleem KS, Price JL, Hashikawa T. 2007. Cytoarchitectonic and chemoarchitectonic subdivisions of the perirhinal and parahippocampal cortices in macaque monkeys. *J Comp Neurol*. 500:973–1006.

Sawatari A, Callaway EM. 2000. Diversity and cell type specificity of local excitatory connections to neurons in layer 3B of monkey primary visual cortex. *Neuron*. 25:459–471.

Sceniak MP, Ringach DL, Hawken MJ, Shapley R. 1999. Contrast's effect on spatial summation by macaque V1 neurons. *Nat Neurosci*. 2:733–739.

Schein SJ, de Monasterio FM. 1987. Mapping of retinal and geniculate neurons onto striate cortex of macaque. *J Neurosci*. 7:996–1009.

Schiller PH, Finlay BL, Volman SF. 1976. Quantitative studies of single-cell properties in monkey striate cortex. I. Spatiotemporal organization of receptive fields. *J Neurophysiol*. 39:1288–1319.

Schmidt M, Bakker R, Hilgetag CC, Diesmann M, van Albada SJ. 2018. Multi-scale account of the network structure of macaque visual cortex. *Brain Struct Funct*. 223:1409–1435.

Schmolesky MT, Wang Y, Hanes D, Thompson KG, Leutgeb S, Schall JD, Leventhal AG. 1998. Signal timing across macaque visual system. *J Neurophysiol*. 79:3272–3278.

Schwabe L, Obermayer K, Angelucci A, Bressloff PC. 2006. The role of feedback in shaping the extra-classical receptive field of cortical neurons: a recurrent network model. *J Neurosci*. 26:9117–9129.

Schwartz EL. 1980. Computational anatomy and functional architecture of striate cortex: a spatial mapping approach to perceptual coding. *Vis Res*. 20:645–669.

Schwartz EL. 1994. Computational studies of the spatial architecture of primate visual cortex. In: Peters A, Rockland KS, editors. *Cerebral cortex, volume 10, primary visual cortex in primates*. New York: Plenum Press, pp. 359–411.

Sclar G, Maunsell JHR, Lennie P. 1990. Coding of image contrast in central visual pathways of the macaque monkey. *Vis Res*. 30:1–10.

Self MW, van Kerkoerle T, Supèr H, Roelfsema PR. 2013. Distinct roles of the cortical layers of area V1 in figure-ground segregation. *Curr Biol*. 23:2121–2129.

Shepherd GMG. 2013. Corticostriatal connectivity and its role in disease. *Nat Rev Neurosci*. 14:278–291.

Shipp S. 2007. Structure and function of the cerebral cortex. *Curr Biol*. 17:R443–R449.

Shipp S, Adams DL, Moutoussis K, Zeki S. 2009. Feature binding in the feedback layers of area V2. *Cereb Cortex*. 19:2230–2239.

Shipp S, Zeki S. 2002a. The functional organization of area V2, I: specialization across stripes and layers. *Vis Neurosci*. 19:187–210.

Shipp S, Zeki S. 2002b. The functional organization of area V2, II: the impact of stripes on visual topography. *Vis Neurosci*. 19:211–231.

Shipp S, Zeki S, Shipp S. 1989. The organization of connections between areas V5 and V2 in macaque monkey visual cortex. *Eur J Neurosci*. 1:309–332.

Shushruth S, Ichida JM, Levitt JB, Angelucci A. 2009. Comparison of spatial summation properties of neurons in macaque V1 and V2. *J Neurophysiol*. 102:2069–2083.

Silverman MS, Grosof DH, De Valois RL, Elfar SD. 1989. Spatial-frequency organization in primate striate cortex. *Proc Natl Acad Sci U S A*. 86:711–715.

Sincich LC, Adams DL, Horton JC. 2003. Complete flatmounting of the macaque cerebral cortex. *Vis Neurosci*. 20:663–686.

Sincich LC, Horton JC. 2002. Divided by cytochrome oxidase: a map of the projections from V1 to V2 in macaques. *Science*. 295:1734–1737.

Sincich LC, Horton JC. 2003. Independent projection streams from macaque striate cortex to the second visual area and middle temporal area. *J Neurosci*. 23:5684–5692.

Sincich LC, Horton JC. 2005. The circuitry of V1 and V2: integration of color, form, and motion. *Annu Rev Neurosci*. 28: 303–326.

Sincich LC, Jocson CM, Horton JC. 2007. Neurons in V1 patch columns project to V2 thin stripes. *Cereb Cortex*. 17:935–941.

Sincich LC, Jocson CM, Horton JC. 2010. V1 Interpatch projections to V2 thick stripes and pale stripes. *J Neurosci*. 30:6963–6974.

Sincich LC, Park KF, Wohlgemuth MJ, Horton JC. 2004. Bypassing V1: a direct geniculate input to area MT. *Nat Neurosci*. 7:1123–1128.

Skottun BC, De Valois RL, Grosof DH, Movshon JA, Albrecht DG, Bonds AB. 1991. Classifying simple and complex cells on the basis of response modulation. *Vis Res*. 31:1079–1086.

Snodderly DM, Gur M. 1995. Organization of striate cortex of alert, trained monkeys (Macaca fascicularis): ongoing activity, stimulus selectivity, and widths of receptive field activating regions. *J Neurophysiol*. 74:2100–2125.

Spear PD, Moore RJ, Kim CB, Xue JT, Tumosa N. 1994. Effects of aging on the primate visual system: spatial and temporal processing by lateral geniculate neurons in young adult and old rhesus monkeys. *J Neurophysiol*. 72:402–420.

Stelzer EHK. 2015. Light-sheet fluorescence microscopy for quantitative biology. *Nat Methods*. 12:23–26.

Stephan KE, Kamper L, Bozkurt A, Burns GAPC, Young MP, Kotter R. 2001. Advanced database methodology for the collation of connectivity data on the macaque brain (CoCoMac). *Philos Trans R Soc B Biol Sci*. 356:1159–1186.

Ta'afua SF, Federer F, Merlin S, Angelucci A. 2018. Parallel feedback pathways between macaque visual areas V2 and V1. *Soc Neurosci*. Online 219.20 [abstract].

Tamamaki N, Tomioka R. 2010. Long-range GABAergic connections distributed throughout the neocortex and their possible function. *Front Neurosci*. 4:Article 202.

Tanigawa H, Wang Q, Fujita I. 2005. Organization of horizontal axons in the inferior temporal cortex and primary visual cortex of the macaque monkey. *Cereb Cortex*. 15: 1887–1899.

Tasic B, Yao Z, Graybuck LT, Smith KA, Nguyen TN, Bertagnolli D, Goldy J, Garren E, Economo MN, Viswanathan S *et al*. 2018. Shared and distinct transcriptomic cell types across neocortical areas. *Nature*. 563:72–78.

Teichert T, Wachtler T, Michler F, Gail A, Eckhorn R. 2007. Scale-invariance of receptive field properties in primary visual cortex. *BMC Neurosci*. 8:Article 38.

Thomson AM. 2002. Synaptic connections and small circuits involving excitatory and inhibitory neurons in layers 2-5 of adult rat and cat Neocortex: triple intracellular recordings and Biocytin labelling in vitro. *Cereb Cortex*. 12:936–953.

Thomson AM, Destexhe A. 1999. Dual intracellular recordings and computational models of slow inhibitory postsynaptic potentials in rat neocortical and hippocampal slices. *Neuroscience*. 92:1193–1215.

Thomson AM, Lamy C. 2007. Functional maps of neocortical local circuitry. *Front Neurosci*. 1:19–42.

Tomioka R, Rockland KS. 2007. Long-distance corticocortical GABAergic neurons in the adult monkey white and gray matter. *J Comp Neurol*. 505:526–538.

Tootell R, Silverman M, Switkes E, De Valois R. 1982. Deoxyglucose analysis of retinotopic organization in primate striate cortex. *Science*. 218:902–904.

Tootell RB, Hamilton SL. 1989. Functional anatomy of the second visual area (V2) in the macaque. *J Neurosci*. 9:2620–2644.

Tootell RB, Mendola JD, Hadjikhani NK, Ledden PJ, Liu AK, Reppas JB, Sereno MI, Dale AM. 1997. Functional analysis of V3A and related areas in human visual cortex. *J Neurosci*. 17:7060–7078.

Tootell RBH, Nelissen K, Vanduffel W, Orban GA. 2004. Search for color "Center(s)" in macaque visual cortex. *Cereb Cortex*. 14:353–363.

Tootell RBH, Silverman MS, De Valois RL, Jacobs GH. 1983. Functional organization of the second cortical visual area in primates. *Science*. 220:737–739.

Tootell RBH, Silverman MS, Hamilton SL, Switkes E, De Valois RL. 1988a. Functional anatomy of macaque striate cortex. V. Spatial frequency. *J Neurosci*. 8:1610–1624.

Tootell RBH, Switkes E, Silverman MS, Hamilton SL. 1988b. Functional anatomy of macaque striate cortex. II. Retinotopic organization. *J Neurosci*. 8:1531–1568.

Trojanowski JQ, Jacobson S. 1976. Areal and laminar distribution of some pulvinar cortical efferents in rhesus monkey. *J Comp Neurol*. 169:371–392.

Ts'o DY, Frostig RD, Lieke EE, Grinvald A. 1990. Functional organization of primate visual cortex revealed by high resolution optical imaging. *Science*. 249:417–420.

Ts'o DY, Roe AW, Gilbert CD. 2001. A hierarchy of the functional organization for color, form and disparity in primate visual area V2. *Vis Res*. 41:1333–1349.

Turrigiano GG. 2008. The self-tuning neuron: synaptic scaling of excitatory synapses. *Cell*. 135:422–435.

Turrigiano GG, Leslie KR, Desai NS, Rutherford LC, Nelson SB. 1998. Activity-dependent scaling of quantal amplitude in neocortical neurons. *Nature*. 391:892–896.

Ungerleider LG, Desimone R. 1986a. Projections to the superior temporal sulcus from the central and peripheral field representations of V1 and V2. *J Comp Neurol*. 248:147–163.

Ungerleider LG, Desimone R. 1986b. Cortical connections of visual area MT in the macaque. *J Comp Neurol*. 248:190–222.

Ungerleider LG, Mishkin M. 1979. The striate projection zone in the superior temporal sulcus of Macaca mulatta: location and topographic organization. *J Comp Neurol*. 188:347–366.

Vanduffel W, Tootell RBH, Schoups AA, Orban GA. 2002. The organization of orientation selectivity throughout macaque visual cortex. *Cereb Cortex*. 12:647–662.

Valverde F. 1978. The organization of area 18 in the monkey - a Golgi study. *Anat Embryol (Berl)*. 154, 305–334.

Van Essen DC. 2003. Organization of visual areas in macaque and human cerebral cortex. In: Chalupa L, Werner J, editors. *Visual neurosciences*. MIT Press, pp. 507–521.

Van Essen DC, Glasser MF, Dierker DL, Harwell J. 2012. Cortical parcellations of the macaque monkey analyzed on surface-based atlases. *Cereb Cortex*. 22:2227–2240.

Van Essen DC, Newsome WT. 1984. The visual field representation in the striate cortex of the macaque monkey: asymmetries, anisptropies, and indiviual variability. *Vis Res*. 24:429–448.

Van Essen DC, Maunsell JHR, Bixby JL. 1981. The middle temporal visual area in the macaque: Myeloarchitecture, connections, functional properties and topographic organization. *J Comp Neurol*. 199:293–326.

Van Essen DC, Newsome WT, Maunsell JH. 2002. The visual field representation in striate cortex of the macaque monkey: asymmetries, anisotropies, and individual variability. *Vis Res*. 24:429–448.

Van Essen DC, Newsome WT, Maunsell JHR, Bixby JL. 1986. The projections from striate cortex (V1) to areas V2 and V3 in the macaque monkey: asymmetries, areal boundaries, and patchy connections. *J Comp Neurol*. 244:451–480.

van Rossum MC, Bi GQ, Turrigiano GG. 2000. Stable Hebbian learning from spike timing-dependent plasticity. *J Neurosci*. 20:8812–8821.

Venkat A, Christensen C, Gyulassy A, Summa B, Federer F, Angelucci A, Pascucci V. 2016. A scalable cyberinfrastructure for interactive visualization of terascale microscopy data. *N Y Sci Data Summit NYSDS*. doi: 10.1109/NYSDS.2016.7747805.

Vidyasagar TR, Eysel UT. 2015. Origins of feature selectivities and maps in the mammalian primary visual cortex. *Trends Neurosci*. 38:475–485.

Wandell BA, Dumoulin SO, Brewer AA. 2007. Visual field maps in human cortex. *Neuron*. 56:366–383.

Wang HX, Movshon JA. 2016. Properties of pattern and component direction-selective cells in area MT of the macaque. *J Neurophysiol*. 115:2705–2720.

Wang Y, Xiao Y, Felleman DJ. 2007. V2 thin stripes contain spatially organized representations of achromatic luminance change. *Cereb Cortex*. 17:116–129.

Weller RE, Kaas JH. 1983. Retinotopic patterns of connections of area 17 with visual areas V-II and MT in macaque monkeys. *J Comp Neurol*. 220:253–279.

Williams SR, Stuart GJ. 2002. Dependence of EPSP efficacy on synapse location in neocortical pyramidal neurons. *Science*. 295, 1907–1910.

Wiser A, Callaway E. 1996. Contributions of individual layer 6 pyramidal neurons to local circuitry in macaque primary visual cortex. *J Neurosci*. 16:2724–2739.

Wiser AK, Callaway EM. 1997. Ocular dominance columns and local projections of layer 6 pyramidal neurons in macaque primary visual cortex. *Vis Neurosci*. 14:241–251.

Xiao Y, Casti A, Xiao J, Kaplan E. 2007. Hue maps in primate striate cortex. *NeuroImage*. 35:771–786.

Xiao Y, Wang Y, Felleman DJ. 2003. A spatially organized representation of colour in macaque cortical area V2. *Nature*. 421:535–539.

Yabuta NH, Sawatari A, Callaway EM. 2001. Two functional channels from primary visual cortex to dorsal visual cortical areas. *Science*. 292:297–300.

Yuan N, Liang Z, Yang Y, Li G, Zhou Y. 2014. Changes of spatial and temporal frequency tuning properties of neurons in the middle temporal area of aged rhesus monkeys. *Eur J Neurosci*. 40:2652–2661.

Yang Y, Liang Z, Li G, Wang Y, Zhou Y. 2009. Aging affects response variability of V1 and MT neurons in rhesus monkeys. *Brain Res*. 1274:21–27.

Yarch J, Federer F, Angelucci A. 2017. Local circuits of V1 layer 4B neurons projecting to V2 thick stripes define distinct cell classes and avoid cytochrome oxidase blobs. *J Neurosci*. 37:422–436.

Yarch J, Larsen H, Chen M, Angelucci A. forthcoming2019. Morphological cell types projecting from V1 layer 2B to V2 thick and thin stripes. *J Neurosci*.

Yoshioka T, Blasdel GG, Levitt JB, Lund JS. 1996. Relation between patterns of intrinsic lateral connectivity, ocular dominance, and cytochrome oxidase-reactive regions in macaque monkey striate cortex. *Cereb Cortex*. 6:297–310.

Zeki S. 2015. Area V5—a microcosm of the visual brain. *Front Integr Neurosci*. 9:Article 21.

Zeki S, Shipp S. 1988. The functional logic of cortical connections. *Nature*. 335:311–317.

Zhou H, Friedman HS, von der Heydt R. 2000. Coding of border ownership in monkey visual cortex. *J Neurosci*. 20: 6594–6611.

Zhu Q, Vanduffel W. 2019. Submillimeter fMRI reveals a layout of dorsal visual cortex in macaques, remarkably similar to new world monkeys. *Proc Natl Acad Sci U S A*. 116: 2306–2311.

Ziemba CM, Freeman J, Simoncelli EP, Movshon JA. 2018. Contextual modulation of sensitivity to naturalistic image structure in macaque V2. *J Neurophysiol*. 120:409–420.